ULTRA-HIGH DISPERSION OF MgO/CaO IN MESOPOROUS SBA-15 AND MACROPOROUS SBA-15 USING A ONE-POT METHOD: NOVEL MATERIAL PREPARATION AND APPLICATION AS A BASE CATALYST FOR TRANSESTERIFICATION

BY

LOIS AFUA DAMPTEY

(10387249)

DEPARTMENT OF MATERIALS SCIENCE AND ENGINEERING,

UNIVERSITY OF GHANA, LEGON

This Thesis is submitted to the University of Ghana, Legon in partial fulfillment of the requirement for the award of MPhil Materials Science & Engineering degree

JULY 2018

ULTRA-HIGH DISPERSION OF MgO/CaO IN MESOPOROUS SBA-15 AND MACROPOROUS SBA-15 USING A ONE-POT METHOD: NOVEL MATERIAL PREPARATION AND APPLICATION AS A BASE CATALYST FOR TRANSESTERIFICATION

BY

LOIS AFUA DAMPTEY

(10387249)

DEPARTMENT OF MATERIALS SCIENCE AND ENGINEERING,

UNIVERSITY OF GHANA, LEGON

This Thesis is submitted to the University of Ghana, Legon in partial fulfillment of the requirement for the award of MPhil Materials Science & Engineering degree

JULY 2018

DECLARATIONS

Candidate's Declaration

I hereby declare that this thesis which is the result of my own original research under strict supervision was prepared in accordance with the University of Ghana's academic regulations and that no part of it has been presented for another degree in this University or elsewhere.

Candidate's name: **Lois Afua Damptey**

Signature: ……. Date: ……...

Supervisors' declaration

I hereby declare that the preparation and presentation of the thesis were supervised in accordance with the guidelines on supervision of thesis laid down by the University of Ghana.

Supervisor's name: **Dr. Johnson Kwame Efavi**, (University of Ghana, Ghana)

Signature..... Date…… ……...

Co supervisor's name: **Dr. Collins Obuah,** (University of Ghana, Ghana)

Signature ……... Date…….

Head of Department's declaration

I hereby declare that this thesis has been prepared, supervised and accepted in accordance with the guidelines on the thesis laid down by the University of Ghana.

Head of Department's name: **Dr. Lucas Nana Wiredu Damoah**

Signature..... Date.....

ABSTRACT

Global uncertainty over fossil fuels security provides the impetus for the development of fuels from renewable feedstocks. A promising route to diesel is available through transesterification of vegetable oils. In this work, there is a novel development of the true liquid crystal templating approach to the synthesis of uniformly dispersed ordered porous mixed oxides. Via this route, a family of mesoporous and mesomacroporous MgO/SBA-15 and CaO/SBA-15 catalysts with metal loading in the range of 1.00-9.00 wt.% and 3.00-18.00 wt.% have been prepared respectively. Textural characterization of the materials shows surface areas > 500 and 600 $m^2. g^{-1}$ for magnesium functionalised mesoporous and macroporous series. Surface areas recorded for calcium functionalized mesoporous and macroporous areas > 200 and 400 $m^2. g^{-1}$. Pore diameters were determined by the N_2 porosimetry and are found to be in the order of 3.0 nm and 4.0 nm for both meso- and macrofamilies. Elemental (ICP-OES) and XPS analysis for magnesium and calcium functionalized species suggest that majority of MgO is preferentially located within the pore network of all catalyst. TGA chromatogram showed desorption of gases evolved for magnesium species but showed desorption of surfaces carbonates for calcium species around 500 ^oC to 800 ^oC. Meso – calcium series (CaO/(TLCT) SBA-15) were further recalcined at 800 ^oC to remove all the surface carbonates. TEM and SEM-EDX images show the uniform dispersion of metal oxide in long channel SBA-15 materials for meso- and interconnected macropores for macro- materials. Catalytic studies have been conducted in stirred batch reactors with pressure flasks at 60 ^oC and 90 ^oC. Optimization studies revealed that most favorable conditions are 10 mmol: excess tributyrin/tricaprylin, 50 mg catalyst and reaction time 24 h. Under these conditions, 3.59 wt.% CaO/(TLCT) SBA-15 was found to be most active providing > 99% of FAME in 24 h. Overall

trend in conversion showed that macropore materials are suitable as compared to mesopore material and this is much more evident in higher triglyceride molecule where 15.78 wt.% CaO/MM – (TLCT) SBA-15 proved to be the best catalyst.

ACKNOWLEDGEMENT

First and foremost, all thank goes to the God Almighty for his guidance and protection from the beginning of the academic year through to the research year. My sincere gratitude goes to the Leverhulme Royal Society African Award for funding my research work I thank Doctor Johnson Kwame Efavi and Doctor Collins Obuah for supervising this work. This thesis would not have been possible without their immense supervision. I would also like to thank Doctor Dorcas Osei Osafo, Professor Karen Wilson and Professor Adam Lee for their help and guidance throughout my research year. I am extremely grateful for this opportunity. I have had extensive help in characterizing my materials and as such, I would like to thank Doctor Mark A. Isaacs, Doctor Christopher M.A. Parlett for their time and patience in performing microscopy of materials. I would also like to thank Thomas Bryant, Constanza Cucuzella for their immense help in the laboratory. I will like to thank Blaine Murray, Edmund Ofei Aidoo, Nicolette Naa Shormeh Noi, Melody Frempong and Abigail Okyere for their support one way or the other throughout the research. Finally, I will like to thank the Synthesis Material and Catalysis Group (SMAC) of European Bioenergy Research Institute (EBRI) of Aston University for making my stay a wonderful and informative one.

DEDICATION

I dedicate this thesis to my parents, Mister. Luke Damptse and Miss. Winifred Brenya and my sister, Eunice Bibian Ama Saaku Damptey. I also dedicate this work to my supervisors, Doctor Johnson Kwame Efavi and Doctor Collins Obuah.

CONTENTS

LIST OF FIGURES

LIST OF TABLES

LIST OF SCHEMES

LIST OF ACRONYMS AND ABBREVIATIONS

wt. %	Weight percent
$m^2. g^{-1}$	Metres squared per gram
FAME	Fatty acid methyl esters
pH	Potential of hydrogen
mL	Millilitres
rpm	Revolutions per minutes
BET	Brunaeur-Emmet-Teller
ICP – OES	Inductively Coupled Plasma – Optical Emission Spectroscopy
FTIR	Fourier Transform Infrared Spectroscopy
TEM	Transmission Electron Microscope
SEM-EDX	Scanning Electron Microscope-Energy Dispersive X-Ray

CHAPTER ONE

1.0 Introduction

This gives the general overview of the project taking into account the project's background, research justification, problem statements, aims and objectives, research question and hypothesis, the scope and limitation of the project and the research approach.

1.1 Background

The transportation sector of the global economy is one of the top energy consumer and depends heavily on fossil fuel [1–5]. Due to urbanization, industrialization and population growth, several attempts have been made to meet goals of demand for energy using fossil fuels. However, using fossil fuel is not sustainable because of the depleting amount of the fuel reserve as well as its associated climate change issues [6–10]. There is, therefore, a concerted effort to explore the alternative source of energy from renewable resources in order to maximize the amount of renewables in the global energy production [11–17].

Biodiesel has been internationally recognized as an alternative renewable source of fuel necessary to increase the percentage of renewables in the total energy mix [11,18–22]. The self-sustaining, carbon neutral and renewable nature of biomass-derived fuels makes them an extremely innovative and exciting petroleum replacement technology [23]. The first generation of biofuels was obtained directly from food crops and involved extracting oil to be processed into biodiesel or fermented to produce bioethanol [24]. These first-generation biofuels convert edible crops as a feedstock, which is extremely unethical considering the large percentage of the world's population currently undernourished [25]. These fuels suffer from reduced yields, typically in the order of 3000-5000

L.hectare^{-1}.year^{-1}, which would not efficiently utilize the crop space [26]. From the arising food versus fuel debate, non-competitive crop feedstocks were sourced, resulting in second generation biofuels [27]. These feedstocks are derived from non-edible food crops helping to eliminate the competition with food crops for land [28].

A key stage in biofuel production is the chemical processing of bio-oil to form biodiesel, which requires a catalyst for these reactions to proceed at appreciable rates. This chemical process is the transesterification of triglyceride compounds (TAG) producing fatty acid methyl esters (FAME), commonly identified as biodiesel, and glycerol as a by-product [29]. This process is a very efficient reaction because the FAME produced can be used as a liquid fuel while the food and pharmaceutical industries use glycerol as a raw material. This chemical process can be acid or base catalysed with their respective advantages and disadvantages [30]. For industrial biodiesel production, some common catalysts used for transesterification process are homogeneous basic catalysts such as NaOH, KOH, or CH_3ONa. [31,32]. The sensitivity of these catalysts to water and available free fatty acid (FFA) reacts to form unwanted by-products such as soap via the process of 'saponification' [33]. Additionally, the product separation process becomes difficult as a result of the soap formation and decreases the strength of the catalyst. A tedious and environmentally friendly water washing process is adapted to eliminate the catalyst from the final product to purify the biodiesel. The end result is the production of large amounts of wastewater which may be very expensive to treat for reuse.

It is not surprising to see the number of researches into heterogeneous base catalysts for use in transesterification reactions. Some include alkaline earth oxides, supported alkali or alkaline earth metals, basic zeolites produced from sodium aluminosilicates and hydrotalcites [34–36].Alkaline

earth oxides alone and its binary metal were used for biodiesel production but were unstable and the catalyst faced reusability issues [37]. This has led to the recent development of mesoporous molecular sieves which acts as surfactant template catalyst to increase transesterification reaction by stabilizing the enzymes and increasing product yield [38–42]. SBA-15 silica, referred commonly as a hexagonally ordered mesoporous material, provides excellent support for heterogeneous catalysts because it has a large pore size, high surface area and very stable and chemically inert [43–45].

1.2 Justification

The global economy is sustained by the consumption of finite petrochemical materials, which is both unsustainable and damaging to the environment. A more pressing concern however, is the polluting nature of consuming petroleum resources which releases damaging greenhouse gasses into the atmosphere. Because of this, alternative sources of energy, synthetic feedstocks and fuel are required. A promising solution to the fuel crisis is liquid fuels produced from biomass, known as biofuels. Most recent research has looked into the developments of heterogenous catalysts in increasing the yield of biofuel production. The highly customizable tuneable nature of these heterogeneous catalysts provides improvements over homogenous catalysed production. This however promotes effective catalyst separation and fuel purification with high amount of biodiesel production. These materials catalyse the transesterification of triglyceride compounds because of increased absorption capacities of active species.

1.3 Problem Statement

The increasing emissions of carbon dioxide paired with the finite nature of petroleum resources means alternative fuel sources are imperative to reduce the impact of global warming. Biodiesel is

an excellent replacement for petrochemical fuels, as it can be produced by renewable, non-competitive and reabsorbs all CO_2 emitted. Current industrial practice uses homogeneous alkaline alkoxides and hydroxides catalysts to produce biodiesel, which require aqueous quenching and neutralisation steps to remove fatty acid impurities as well as difficult separation of products. Alternatively, a solid acid-base hierarchical material could esterify the fatty acid impurity, and transesterification of triglyceride compounds simultaneously in a tandem reaction, with easy separation through filtration. While many basic species can, and have been used successfully, alkaline earth oxide species are well suited to this reaction. Among heterogeneous bases, alkaline earth-based metal oxide specifically magnesium and calcium supported catalysts have become the go-to catalysts for the transesterification reaction because they are easy to acquire and cost significantly less [46]. A family of novel mesoporous and hierarchical (meso-macroporous) materials with the increased addition of magnesium and calcium nitrate precursor was synthesized using True "Liquid Crystal Templating (TLCT)" method. This was confirmed by Attard *et al* to be a very reliable method in the preparation of hexagonal large, crack-free monoliths with outstanding shape control and surface morphology [47]. The metal particles are only added during the silica preparation resulting in the production of surfactants with the metal precursor incorporated within the head group. This approach ensured that the catalysts were incorporated in the surfactants and upon calcining the material, the surfactants were removed after templating, leaving the metal nanoparticles within the pores of the silica. The SBA-15 was *in-situ* coated with magnesium and calcium by adding their nitrate salt to the initial mixture of raw materials for the one-step synthesis of novel material with a mesoporous structure and strong basicity. Mg^{2+} and Ca^{2+} ions interact strongly with "poly (ethylene oxide) (PEO) surfactant" head groups by creating helical crown-ether-like metal-PEO complexes, the existence of Mg^{2+} and Ca^{2+} species in the

sample prevents the non-ionic surfactant from decomposing. Introduction of macroporosity to form hierarchical materials was used in comparison to mesoporous materials to study if there is a reduced diffusion pathway as the mesopores are more accessible due to the macropore network.

1.4 Research Question and Hypothesis

This research work aims to provide answers to questions arising from literature and find basis for accepting or rejecting the hypothesis stated below;

Research Questions

i. Does the use of true liquid crystal templating method in a one pot synthesis provide a more stable, active catalyst?
ii. Does the use of alkaline earth metal oxides incorporated into a porous system in the form of MgO/TLCT SBA-15 and MgO/(TLCT) MM-SBA-15, CaO/TLCT SBA-15 and CaO/(TLCT) MM-SBA-15 provide a better catalytic performance for transesterification?

Hypothesis

Alkaline earth metal oxides have been shown to catalyse a wide variety of reactions due to their varying level of basicity resulting from the ease of OH- ions release when dissolved in water and transesterification of triglyceride is favored by strong basic sites at the catalyst surface. In a basic catalytic transesterification, the reaction mechanism proceeds via the deprotonation of the alcohol species by the basic catalyst. The strong basic active sites provide sufficient adsorptive sites for methanol where O-H readily break into methoxide anions and hydrogen cation. There is therefore a reaction between methoxide anions and triglyceride molecules to yield methyl esters. However, stand-alone alkaline earth oxides as heterogenous catalysts are relatively unstable. The stability of

these catalysts can be enhanced by loading them onto stable porous supports. It is therefore hypothesized that alkaline earth metal oxides loaded into mesoporous and macroporous SBA-15 support can enhance transesterification of seed oils into biodiesel due to the availability of strong basic sites and stability of the composite catalyst.

1.5 Aims and Objectives

Various literature reviewed in section 2.0 below have reviewed varying methods for synthesizing heterogenous catalysts. Most of these processes require higher experimental time to produce less surfaced area catalysts. This research seeks to achieve a less experimental and economical approach for synthesizing highly stabilized heterogenous catalysts. The research also seeks to increase the diffusivity rate for free pathway for bulkier and larger triglyceride transesterification. These objectives can be achieved from the following specific objectives,

- Synthesis, characterize and test the activity of novel ultra-highly dispersed mesoporous and hierarchical (meso-macroporous) magnesium and calcium species materials using TLCT method.
- Determine the effect of adding magnesium and calcium salt to the liquid crystal and subsequent composite structure.
- Optimise magnesium and calcium content for transesterification reactions, without destroying ordered nanostructure.
- Optimise reaction conditions for nanocomposite materials for transesterification reactions and concluding on the best catalyst.

1.6 Scope and limitation

Scope

This research focuses mainly on the use of transitional metal oxides incorporated in mesoporous and meso-macroporous silica as a heterogenous catalyst support characterized and used for transesterification reaction into fatty acid methyl esters.

Limitation

These things were not covered in the study;

i. Chemisorption of CO_2 to determine turnover frequencies of active sites
ii. Determination of leaching studies to find the percentage and rate of the leaching of metal oxides during reaction.
iii. Determination of stability of catalyst in reaction, that is, running same catalyst for four to five reactions.
iv. Using other alkaline earth metal oxides for comparative studies.

1.7 Research Approach

The research methods used in the focus of this work to achieve the aims and objectives are detailed below;

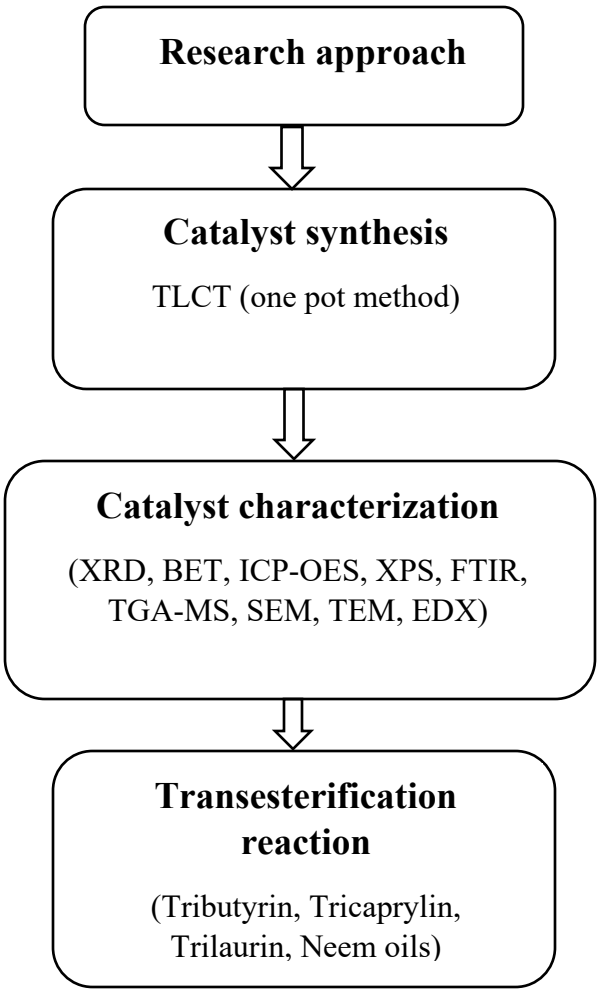

CHAPTER TWO

2.0 Literature Review

This chapter reviews the underlining theoretical principles used in this work. It focusses on the history, applications, methods and chemistry biodiesel production. The need of catalysts in increasing biodiesel production. The advantages and disadvantages in using homogenous routes and heterogenous routes. The application of mesoporous sieves to increase the stability and activity of heterogenous catalyst in the application of biodiesel production is reviewed.

2.1 Background

The hallmark of developing and developed countries depends on the ability to create sustainable solutions to meet the needs of its people. This ensures that future generations are not affected by the current solutions in place [48]. In the context of energy, fossil fuel reserves such as crude oil, tar sands, deepwater wells, shake, and gas are diminishing whiles increasing carbon resources in the ecosystem [48]. It is therefore important to meet the rising energy demands of a rapidly growing population as well as mitigating the carbon dioxide emissions and hence climate change [49–51]. Biofuels provide an alternative source of renewable energy that provides greater fuel security, reduce greenhouse gases and easy to source [52,53]. Currently, the two common biofuels [54] used in transportation sector are ethanol obtained from corn, sorghum or sugar cane are normally used in gasoline engines [55] and biodiesel that is produced from vegetable oils, animal fats, waste cooking oils, grease are used in diesel engines [56]. Food crops such as grains and sugar beet primarily serve as the source for the production of first-generation biofuels [28]. They are however limited in supply owing to the dependency of people on it for food and can therefore not be used as targets for oil product substitution. It does not provide a long-term solution to use in mitigating climate change and has low economic benefit. In an attempt to find a more long-lasting

solution, current research is based on developing biofuels produced from non-food biomass known as second-generation biofuels. Residue from the forest, energy crops purposely grown such as vegetative grasses as well as feedstocks from lignocellulose materials can help eliminate the challenges facing the use of first-generation biofuels and potentially reduce production cost with higher economic value [57].

2.2 Production of Biodiesel

Biodiesel is produced through various methods knows as pyrolysis, esterification, and transesterification. The esterification process involves the reaction of oils and fats into long-chain mono alkyl and reacting with alkyl chain alcohol in a presence of a catalyst [58–60].

Vegetable oil and animal fats can be processed as biodiesel in the transesterification reaction, a simple process of combining an "ester" and an alcohol to make another ester and another alcohol. The newly formed alcohol is called glycerol or, more commonly, glycerin [61].

Vegetable oils are obtained from edible and non-edible plant sources. Unfortunately, using edible sources for the production of first-generation biofuels has received wild criticisms due to perceiving competition between land usage for fuel crops versus traditional agricultural cultivation [62–64]. This result in the production of biodiesels from other sources other than the use of food supplies. For example, the use of waste oils and fats from restaurants and food-processing plants to produce biodiesel is becoming economical. This is a nice way to harness additional stocks of oil not needed for other purposes, to research new oilseed crops that can be sown on marginal land and to use non-edible oils from plants already growing in many areas [65,66].

There are ongoing researches to produce biodiesel from feedstocks that have little demand for landscape for example, some types of algae can produce oil. Researchers continue to experiment

with producing fuel from cheap, non-edible biomass (such as agricultural residue, wood products industry, and other grasses) that can be changed into a diesel fuel replacement [30,67,68].

2.3 Esterification

The term ***ester*** was coined in 1848 by the famous German chemist Leopold Gmelin [69]. As with the names of many functional groups, the word ester is a portmanteau. In this case, it is derived from the German *Essigather,* which describes the compound acetic ether, modern-day ethyl acetate. The process of esterification: the condensation of an alcohol and carboxylic acid (Scheme 2. 1) has been reported. Since then, this reaction has been extensively studied and several modifications, which aim to improve the ease at which the reaction occurs and the yields obtained, have been made.

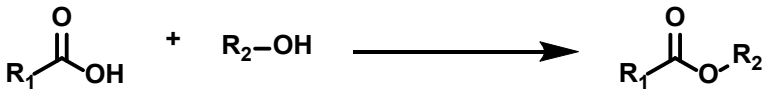

Scheme 2. 1: General scheme showing the reaction between carboxylic acid and an alcohol to form an ester (where R1 and R2 are any other groups)

Owing to the fragrant properties of many esters, it is easy to understand why esterification is so important industrially in the preparation of fragrances and flavorings. However, ester containing compounds have a much greater utility and value than just its use in preparation of fragrances and flavorings. The ester functional group is present in many blockbuster pharmaceuticals, dyes, liquid crystals, and polymers to name but a few. Indeed, almost any class of organic materials of

relevance to the demands of modern civilization feature the ester functional group. Of greater relevance to this thesis, esters in the form of triglycerides (Scheme 2. 2) are the principal constituents of fats and oils [70–74].

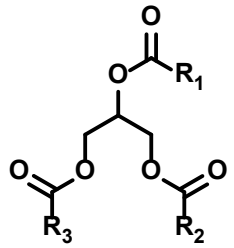

Scheme 2. 2: General formula of a triglyceride (where R1, R2 and R3 are alkyl groups)

When the alkyl groups are made up of linear hydrocarbon chains of 9 to 18 carbon atoms [75] in the length, then the triglyceride becomes attractive for the synthesis of biodiesel. However, triglycerides do not represent ideal fuels owing to their high viscosity and tendency to oxidize and form waxes. To overcome these challenges, ***transesterification*** has been identified as a potential route to esters to lower viscosity [76]. Transesterification can proceed in one step or a combination of three ways depending upon the reagents and conditions employed (Scheme 2. 3). If the R group originating from the alcohol is exchanged for another, then the process is termed ***alcoholysis***, if the R group originating from the acid is exchanged for another, then the process is termed ***acidolysis***. The final mode by which transesterification may be achieved is an ***ester-ester exchange*** where a mixture of two different esters are brought into contact and mutual exchange of the alkyl groups occurs [77–79]. For transesterification in the production of bio-oils, the overwhelmingly

preferred route is alcoholysis as the nature of the moiety from the alcohol (Scheme 2. 3) has the greatest control over the physical properties of the resultant esters.

1. Alcoholysis

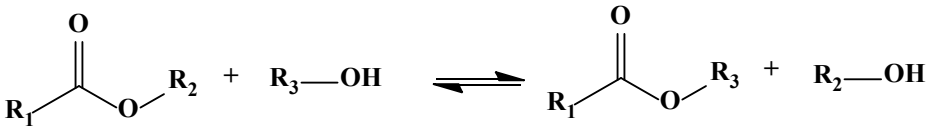

2. Acidolysis

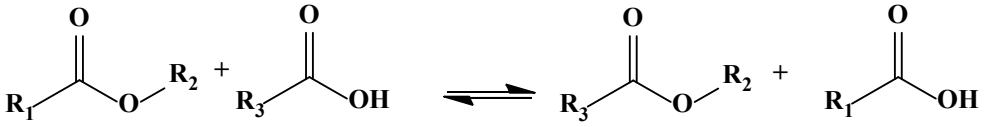

3. Ester-ester exchange

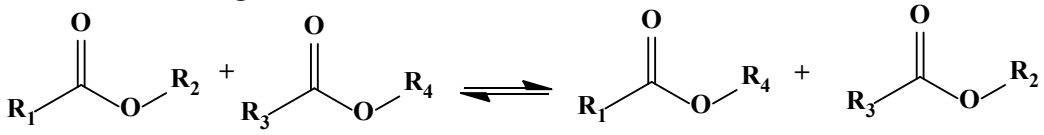

Scheme 2. 3: Schematic representation of the three processes of transesterification. See body for descriptions

Typically, in the production of biodiesels, the alcohol selected for transesterification is methanol and the resulting methyl esters are of sufficiently low viscosity. Another method in which the methyl ester can be produced, although less efficient, is through a saponification-esterification route (Scheme 2.4). Here the triglyceride is subjected to base-catalysed hydrolysis (saponification) which produces glycerol and fatty acid salts. The resulting mixture is then treated with acid to neutralize excess base and form the free fatty acid. Subsequently, through the addition of a suitable acid catalyst and methanol (or other alcohol as desired), the desired esters are formed [80].

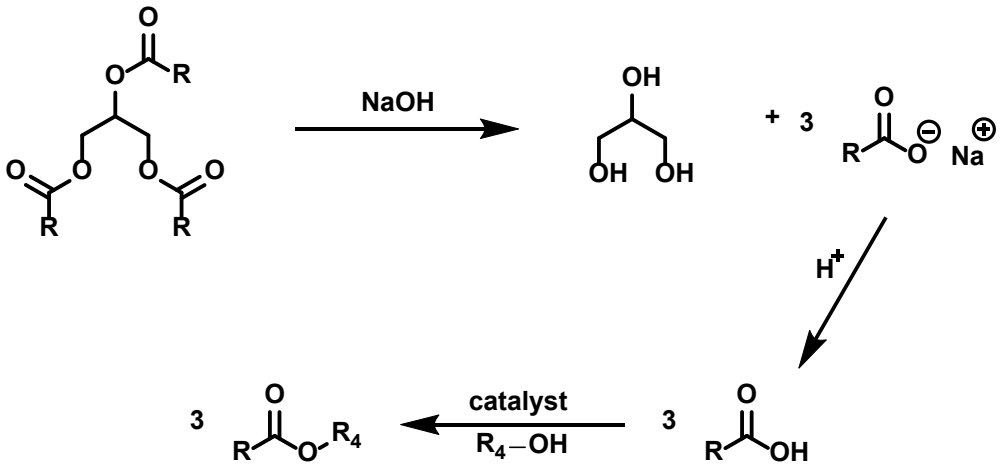

Scheme 2.4: Saponification-esterification sequence for the formation of new esters from triglycerides

2.4 Homogenously Catalysed Transesterification

This transesterification reaction method deals with catalysts that are in the same phase as the reactants. This reaction attains equilibrium more quickly by increasing the rate of both forward and revere reactions. As both the homogenous catalyst and reactants are in the same phase, there is greater interaction between the two species. The higher the degree of interaction gives a greater effective concentration which intend allows for milder conditions without reducing the reaction rate [57]. The main disadvantage with homogeneous catalysts is the difficulty with separating the catalyst from the product. This increases the difficulty, economic and environmental cost of isolating both the catalyst and product, and also leads to saponification; where triglycerides react

with water to produce soaps [81], and emulsification; which results in the loss of esters and glycerol [82]. This means additional steps are required to isolate the fatty acid methyl ester product and lengthy cleaning processes [82].

2.5 Heterogeneously Catalysed Transesterification

It has long been known that saponification, esterification, and transesterification by any of the routes discussed above can be performed homogeneously by any number of acids and bases in either catalytic or stoichiometric quantity [83,84]. Furthermore, it is known that many of these are excellent and can achieve equilibrium levels within a matter of seconds under the correct conditions. However, for processing biodiesels, these materials present several technical drawbacks which render their use unattractive. Homogeneous catalysts are difficult to recover and produce product and waste streams with extreme pHs which require neutralization prior to further processing or disposal [85]. Often, water is produced as a by-product which results in intractable emulsions requiring extensive separation efforts. For the preparation of high-quality bio-diesel, it is imperative to reduce the water content as the fatty acid methyl esters are hydrolytically unstable. Additionally, wet oils are undesirable as they contribute to engine corrosion [85–87].

Considering the above-mentioned problems encountered in the use of homogeneous materials, increasing attention is being given to heterogeneous catalysts [88]. Research to date has covered both acidic and basic materials for this purpose. Materials studied include organic, inorganic, inorganic-organic hybrid materials with structures ranging from simple particulates to highly complex structures designed to impart specific properties such as hydrophilicity/hydrophobicity, tailored pore sizes and networks amongst others [89–91]. This literature review will focus only on the use of alkaline earth metal oxides used as stand-alone catalysts and in conjunction with designer porous supports.

2.5.1 Catalysis with Magnesium Oxide

Reports have shown that for MgO catalyzed transesterification reactions there are several key parameters which affect the conversion or yield. Principally, the preparation of the MgO catalyst is of paramount importance [92–94]. Through various preparation methods, the physical properties of the MgO can be fine-tuned to obtain higher conversion which is sensitive to factors [95] such as particle size, surface area, pore volume, base site strength and density.

Various methods for preparing MgO have been reported and each of which gives materials of differing characteristics [96,97]. Simple thermal treatment of the MgO is sufficient to modulate the textural and chemical properties, providing access to a series of catalysts with systematically varying properties, thereby enabling detailed studies of the effects of their catalytic performance [98–100]. It has been demonstrated that MgO with a low surface area (0.45 m^2 g^{-1}, Table 2. 1: entry 1) gives rise to a low conversion of triacetin [84] and it was found that homogeneously catalyzed transesterification nanoMgO (Table 2. 1: entry 2b) significantly outperformed MgO catalysis (> 99 % conversion in < 5 min. compared to 18 % conversion over 7 h). However, Xu *et al.* observed that when the surface area is increased, a dramatic increase in conversion is observed (Table 2. 1: Entries 3a – 3d**,** Figure 2. 1)[94]. Using a series of MgO catalyzed prepared *via* thermal decomposition of $(MgCO_3)_4Mg(OH)_2$. Xu *et al.*, demonstrated that increasing the calcination temperature produces a net increase in the surface area with an optimum temperature of 450 ºC. Additionally, the pore volume of the MgO is found to constantly increase in the range 450 – 800 ºC. Catalytic studies reveal that optimum monoglyceride yield occurs for catalysts prepared between the temperature of 550 – 750 ºC where surface area is decreasing and pore volume increases. This result demonstrates that there is a fine balance between these two properties. To further understand this Xu *et al.* studied the basic properties of the materials using CO_2 pulse

titrations. They found that as the calcination temperature is increased there is a loss of the total number of base sites which correspond to slight decreases in base site density (mol CO_2 m^{-2}) (Table 2. 1: entries 3b and 3d,). Therefore, in this case, the increase in activity is not attributable to an increase in basicity. Rather suggest that large pores are required to provide access to a greater number of base sites.

In direct contrast to this Montero *et al.* [101] have conducted a detailed spectroscopic study on MgO prepared *via* a sol-gel route using $Mg(OMe)_2$ precursor. As with other studies, the textural and chemical properties of this MgO are controlled through calcination leading to materials with systematically varying properties. Wide angle XRD analysis (Figure 2.2) shows an increased expression of the polar (111) facet when the calcination temperature is increased. Pore sizes increase as temperature increases. These results demonstrate that increasing the calcination temperature increases the basicity (Table 2. 1: Entries 4a – 4d). Catalytic studies show that MgO calcined at higher temperatures provide greater activity, therefore demonstrating that increasing basicity increases activity. Glyceryl tributyrate conversion varied between 60-80% over 24 h.

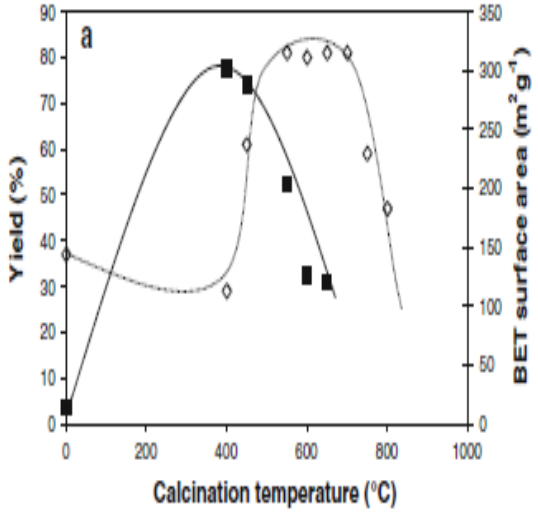

Figure 2. 1: Influence of calcination temperature, surface area on the yield of methyl esters [94]

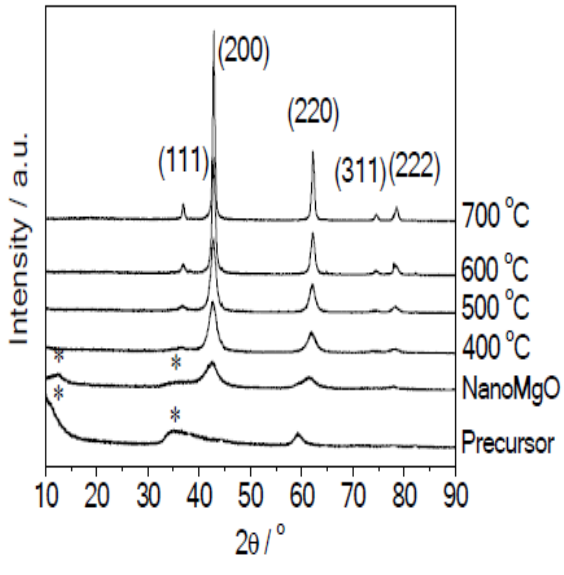

Figure 2.2: Wide angle X-Ray diffractometer spectra of nano-MgO calcined over 400-700 °C [101]

Table 2. 1: Literature showing the various reactions for the use of MgO for transesterification

Entry	Catalyst	Pre-treatment	Surface area, $m^2 g^{-1}$	Particle size, nm	Base site density, mol CO_2 m^{-2}	Pore radius, nm	Substrate	Conditions	Substrate conversion, %	Yield, %	Reference
1	MgO		0.45				Triacetin	60 °C, 8 h, 1700 rpm, 6:1 MeOH:triacetin, 2 wt. % MgO	18	-	[84]
2a	Nano-MgO			60			Soyabean oil	523 K, 2.4 MPa, 30 min, 6:1 MeOH-oil, 3 wt. % MgO	70	-	[102]
2b	Nano-MgO			60					99	-	[102]
3a	MgO	400	53			12	Vegetable oil	200 °C, 50 bar (He)		28	[94]
3b	MgO	450	292		1.18	15		15 min, 1000 rpm 6:1 MeOH-oil, 0.13 g MgO		60	[94]
3c	MgO	550	213			20				80	[94]
3d	MgO	600	166		1.10	25				78	[94]
4a	Nano-MgO	400	360	5.1			Glyceryl tributyrate	0.001mol GT, 1.5ml MeOH,0.0025mol DHE, 60,24hr, 50mg catalyst			[101]

Entry	Catalyst	Pre-treatment	Surface area, $m^2 g^{-1}$	Particle size, nm	Base site density, mol CO_2 m^{-2}	Pore radius, nm	Substrate	Conditions	Substrate conversion, %	Yield, %	Reference
4b	Nano-MgO	500	250	7.3	-		Glyceryl tributyrate	0.001mol GT, 1.5ml MeOH,0.0025mol DHE, 60 °C,24hr, 50mg catalyst			[101]
4c	Nano-MgO	600	140	10.8	-		Glyceryl tributyrate	0.001mol GT, 1.5ml MeOH,0.0025mol DHE, 60 °C,24hr, 50mg catalyst			[101]
4d	Nano-MgO	700	80	16.5	-		Glyceryl tributyrate	0.001mol GT, 1.5ml MeOH,0.0025mol DHE, 60 °C,24hr, 50mg catalyst			[101]

2.5.2 Catalysis with calcium oxide

Calcium oxide is considered as a viable catalyst for solid base catalyst since it is readily available and cheap. CaO has over the years displayed higher transesterification activity. Kouzu *et al.* [103] reviewed the use of CaO, $Ca(OH)_2$, $CaCO_3$ and CaO-air for transesterification of soyabean oil into biodiesel (Table 2. 2: entry 1-3a). CaO shows a high conversion of 93% under 1 h reaction time. $Ca(OH)_2$ shows 93% conversion as well but at 3.5 h. On the other hand, $CaCO_3$ shows absolutely no conversion at various reaction conditions. Zhu Huaping *et al.* [104] studied the transesterification of Jatropha curcas oil into biodiesel using CaO (Table 2. 2: entry 3b). Results show a 93% conversion as well as compared to that of Kouzu *et al.* operating at optimum conditions of 900 catalyst calcination temperature, 70 ^{o}C reaction temperature, 2.5 h reaction time, catalyst dosage of 1.5% and methanol/oil molar ratio of 9:1. Granados *et al* [105] researched on the catalytic activity of CaO for transesterification of sunflower oil into biodiesel (Table 2. 2 for reactions conditions). Freshly obtained fine powdered CaO (Table 2. 2 : entry 3c) experienced a weight loss of 10% which yielded an approximate conversion of 30-40%. It was concluded that the performance of catalysts depended partially on the surface of the solid with basic sites.

Table 2. 3: Table showing the literature of the use of CaO as a heterogenous catalyst for transesterification

Entry	Catalyst	Pre-treatment	Surface area, $m^2\ g^{-1}$	Particle size, nm	Base site density, mol CO_2 m^{-2}	Pore size,	Substrate	Conditions	Substrate conversion, %	Yield, %	Reference
1	CaO	900 ,1.5h , (He)	13				Soyabean oil	60 , 8 h, 1700 rpm, 6:1 MeOH:triacetin, 2 wt. % MgO	93	-	[103]
2a	$Ca(OH)_2$	He	16	-			Soyabean oil	523 K, 2.4 MPa, 30 min,	93	-	[103]
2b	$CaCO_3$		10	-			Soyabean oil	6:1 MeOH-oil, 3 wt. % MgO	0	-	[103]
3a	CaO-air	-	13			-	Jatropha curcas oil	70,2.5hr, 1000 rpm 9:1 MeOH-oil, 1.5% catalyst dosage	Below 10%	-	
3b	CaO	900	-		-	-			93	-	[104]
3c	CaO	973	-	-	-	-			30-40%	-	[105]

Research has led to the development of porous materials specifically mesoporous materials (with pore sizes within the range of 2-50 nm) where precursor solutions of metal oxide are incorporated inorder to maximize the surface areas improve stability and prevent the leaching of metal ions of a heterogeneous catalyst. Porous materials have been widely studied with regard to its application as catalysts and catalysts support [106,107]. Porous materials can be classified into three different divisions [108]; microporous materials (pore sizes < 2 nm), mesoporous materials (pore sizes between 2-50 nm), macroporous materials (pore sizes > 50 nm). Researchers are currently investigating with increasing pore sizes into mesopore range to allow larger molecules to enter the pore system to be processed there and to leave the pore systems easily. The open structure and tuneable porosities help mesoporous materials with the easy availability of metal ions and reagents [109].

2.6 Mesoporous Materials

Mesopore sizes such as pillared clays have been studied since the 1980s. These pillared clays, however, had partially opened rectangular pores and hence reagents and products could not diffuse through them. During this period, templates have not been realized. Japanese scientists in the early 1990s [110] and Mobil Oil scientists [111] distinctly described the synthesis of mesostructured silicates. Mobil reported that "quaternary ammonium" cationic surfactant such as "cetyltrimethylammonium bromide ($C_{16}H_{33}N(CH_3)_3$)-Br, CTAB)" firstly used as a template to create highly ordered M41S [110] "mesoporous silicate molecular sieves" using hydrothermal conditions. This material created uniform pore sizes from micropore to mesopore range. Hereby, the idea of "template" was hypothesized in the synthesis of mesoporous silicate materials. "Mesoporous molecular sieves" formed from organic-inorganic assemblies such as amphiphilic

surfactants and biomacromolecules as templates contribute the main mesoporous family [112]. Surfactants are mainly employed as templates.

In 1969, the first synthesis of mesoporous materials was patented however these materials failed because their characteristics were not fully exploited. In 1992, a comparable material was produced by a scientist in "Mobil Oil Corporation" who discovered these characteristics thereby opening up new fields of research in the field. MCM-41 which represent Mobil Composition of Matter No. 41 shows a highly ordered hexagonal structure with unidimensional pores width [113].

Different materials have been looked into and group II materials are more prevalent. Among the various types of mesoporous silica, mostly MCM-41 and SBA-15 have been used as supports. However, SBA-15 supported materials are more active and stable due to their larger pore sizes (which mitigates against diffusional constraints), thicker pore walls (which promotes the maintenance of structural stability). Sullivan *et al* concluded that "group II active phase is more dispersed on SBA-15 support than MCM-41". This effect leads to an increased catalytic activity of SBA-15 supported materials [114,115]. The project focuses on finding the best candidate catalyst by dispersing MgO and CaO on SBA-15 using their respective precursor solutions.

2.6.1 Catalysis with MgO/SBA-15

From Table 2. 3 - Table 2. 5, Eugena *et al* [116] conducted a series of catalytic activities of various MgO functionalized mesoporous materials prepared using "*in-situ"* coating method and incipient wetness impregnation method in the transesterification of vegetable oils. Low angle XRD patterns (Figure 2. 3) of these series of catalysts showed that the mesostructure of the catalysts maintained after MgO loadings. Surface areas range from 200-600 m^2. g^{-1} although in-situ coated SBA-15 with MgO using the acetate as the anion salt precursor showed the highest surface area.

Additionally, “in-situ” coating MgO/SBA-15 showed the highest pore sizes as well as pore volumes. Among all the catalysts tested, SBA-15 impregnated with MgO with anion salt as the precursor was found to be most active under the specified conditions. However, this experiment was done at an extremely high temperature of 220 ^{o}C.

Table 2. 4: Properties of as-prepared SBA-15

Entry	Catalyst	Pre-treatment	Surface area, $m^2 g^{-1}$	Pore size(Å)	Pore volume(cc/g)	MgO %	Substrate	Conditions	Substrate conversion, %	Yield, %	Reference
1	SBA-15	550, 4 h	679	50.3	0.85	-	Vegetable oil	220, 5 h, 1700 rpm, 17:5 EOH:oil, 1g catalyst	-	-	[116]

Table 2. 5: Properties of in-situ coating of MgO on SBA-15

Entry	Catalyst	Pre-treatment	Surface area, $m^2 g^{-1}$	Pore size(Å)	Pore volume(cc/g)	MgO %	Substrate	Conditions	Substrate conversion, %	Yield, %	Reference
1	MgO(A)-S	550, 6 h	531	69.6	0.92	4.58	Vegetable oil	220, 5 h, 1700 rpm, 17:5 EOH: oil, 1g cata.	-	-	[116]
2	MgO(N)-S	550, 6 h	524	69.4	0.91	1.45	Vegetable oil	220, 5 h, 1700 rpm, 17:5 EOH:oil, 1g catalyst	-	-	[116]

Table 2. 6: Properties of incipient wetness impregnation of MgO on SBA-15

Entry	Catalyst	Pre-treatment	Surface area, $m^2 g^{-1}$	Pore size(Å)	Pore volume(cc/g)	MgO %	Substrate	Conditions	Substrate conversion, %	Yield, %	Reference
1	S/MgO(A)	550, 6 h	252	37.6	0.24	15.41	Vegetable oil	220, 5 h, 1700 rpm, 17:5 EOH: oil, 1g catalyst	96	-	[116]
2	S/MgO(N)	550, 6 h	315	25.2	0.20	15.26	Vegetable oil	220 °C, 5 h, 1700 rpm, 17:5 EOH:oil, 1g catalyst	-	-	[116]

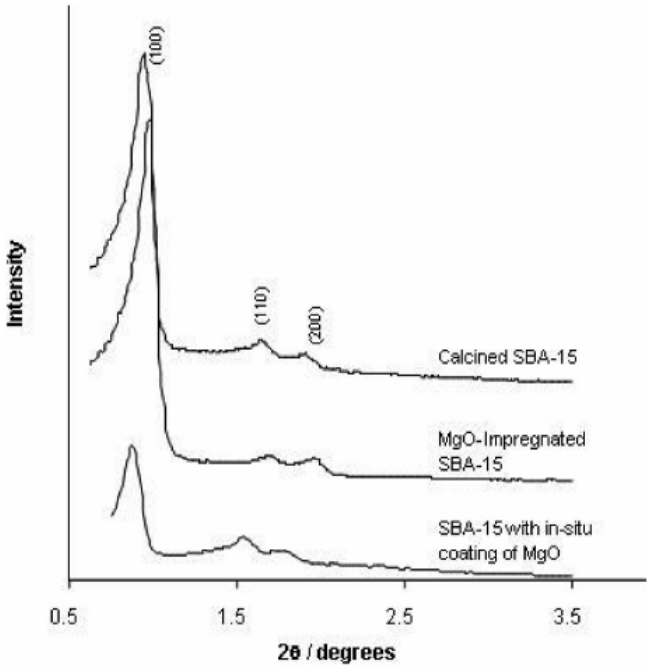

Figure 2. 3: Low angle X-Ray diffractometer patterns showing the mesostructure of MgO/SBA-15 [116]

2.6.2 Catalysis with CaO/SBA-15

There are few reports of the formation of CaO on SBA-15. W.Xie *et al* [117] synthesized CaO-MoO_3-SBA-15 catalyst by incipient wetness impregnation. The findings from this experiment show that the activity of the catalyst depends on the temperature the material was calcined at and the loading amount of calcium and molybdenum oxides. The solid catalyst could afford the oil conversion of 83.2% by using 6 wt.% catalyst with methanol/oil molar ratio of 50:1 under reflux condition. Most literature has widely reported the synthesis of CaO/SBA-15 to obtain widely dispersed calcium species. Biodiesel yield of as high as 99.1% was achieved on the 0.5 CaO/SBA-15 catalyst at a reaction temperature of 200 ºC for 8 h by Hui Sun *et al* [118].

Albuquerque *et al* [119] reported on the synthesis of 14 wt.% of CaO supported on SBA-15 as the most active catalyst with 7.4 $m^2.g^{-1}$ surface area, the pore diameter of 5.4 nm and pore volume of 0.019 $cm^3.g^{-1}$. The transesterifying activity of the catalyst showed as high as 95% with sunflower oil (after 5 h reaction time) and 65% with castor oil (after 1 h reaction time) under the reaction conditions of 1 wt.% catalyst, 12:1 methanol to oil ratio, 338K, 1250 rpm.

Sullivan *et al* reported the synthesis of CaO/SBA-15. The catalyst had a surface area of 653 $m^2.g^{-1}$ and pore size 9.6 nm. At a reaction temperature of 50, there was no leaching of group II materials from the catalyst to the solution during the reaction and are most effective [114].

2.7 Synthesis Mechanisms and Pathway

Various methods [120–123] have been investigated in the formation of mesostructures using the "surfactant self-assembly" method. The first "liquid crystal" templating method was proposed by Mobil scientists were investigated to be "true" since the pathways included all possibilities. Two

main pathways seem to be effective in the preparation of mesostructures and these include the "cooperative self-assembly" and "true liquid crystal templating" [124].

2.7.1 Surfactants

Surfactants used in synthesizing highly ordered mesostructures are uniformly mixed in water. They are grouped as cationic, anionic and nonionic surfactants. Some are able to react as base or acid and has been researched on collectively as amphoteric surfactants. Additionally, ordered mesoporous silicate substances can be effectively synthesized using "Quaternary cationic surfactants ($C_NH_{2N+1}N(CH_3)_3Br(n = 8\text{-}22)$". Commercially available CTAB is often used [125]. The novel frameworks formed by cationic surfactants make it important as structure directing agents. Heating cationic surfactants increase its solubility and subsequently causes a rise in micelle temperature but become toxic [126]. Recently, anionic surfactant terminal carboxylic acid is adapted as template for the synthesis of "mesoporous silica". Alternatively, the use of nonionic surfactants can significantly increase pore structure through intercalation with other compounds to produce large interlayer spacing and more stable compounds than cationic compounds. They are biodegradable, nontoxic and very cheap for industrial-scale production [127–129]. Pore sizes of about 3nm are preferred. Examples of mesoporous materials with uniform pore sizes and highly ordered greater than 5 nm were synthesized by using "poly(ethylene oxide)-*b*-poly(propylene oxide)-*b*-poly(ethylene oxide) (PEO-PPO-PEO) triblock copolymers" as templates in acidic aqueous media [130].

2.7.2 Cooperative self-assembly of surfactants and silica source to form a mesostructure

The ability for small molecules to cooperatively interplay has been found to have massive effect on the nano structuring of materials. This idea was initially proposed by Stucky and coworkers [131] and later accepted by most researchers. Cooperative self-assembly in organic surfactant and inorganic precursors are generally involved in the formation of mesostructured composites. Mesoporous molecular sieves are produced upon removing the surfactant [132]. Surfactant system provides a quick method for reducing interfacial tensions in removing organic pollutants. Goldfarb and co-workers [133] investigated the formation mechanism of mesoporous silica SBA-15 and observed a constant change from spheroidal micelles into threadlike micelles then to form bundles due to a reduction in polarity and water content. Before the hydrothermal treatment, the major portion of PEO chains inserts into silicate frameworks, which generate micropores after the removal of templates. The amount of PEO chains found in the silicate micropores are dependent on hydrothermal aging temperature and the Si/P123 molar ratio [133,134]. Flodstrom *et al*. [135] studied "the formation dynamics of SBA-15 on the basis of time-resolved *in-situ* H NMR and TEM investigations". Four stages were detected during the "cooperative assembly", which is the "adsorption of silicates on globular micelles", the "association of globular micelles into floes", the "precipitation of floes", and the "micelle-micelle coalescence".

2.7.3 Liquid crystal templating

Ordered mesoporous materials can be synthesized using a surfactant templating approach known as the True or Semi-Liquid Crystal Templating. Attard *et al* [47] used "nonionic surfactant" to synthesized mesoporous silicas as templates. The condensation of inorganic precursors is

improved owing to the confined growth around the surfactants thereby forming a ceramic-like framework. After the condensation, the organic templates can be removed by calcination and extraction. The inorganic materials “cast” the mesostructures, pore sizes, and symmetries from the liquid-crystal scaffolds.

2.8 Bifunctional materials

Conventional multistep reactions occur using multiple catalytic materials, over many steps with costly labour-intensive separation steps in between. By performing these sequential reactions in one pot using a single catalyst, these expensive purification and separation steps can be negated. In 2015, Parlett *et al* [136] used a bifunctionalised meso-macroporous SBA-15 to oxidize cinnamyl alcohol to cinnamaldehyde, then to cinnamic acid using spatially separated palladium and platinum species working synergistically [137]. This cascade reaction, which requires a selectivity towards the hydroxide species, leaving the alkene species intact. The first step is selectively catalysed by palladium; however, the second step is selectively catalysed by platinum. By spatially separating these noble metal species into a hierarchical system, illustrated in Figure 2.4, overall conversion to the cinnamic acid is favored. The hierarchical nature of the material, paired with the increased diffusion throughout the material results in a superior catalytic species.

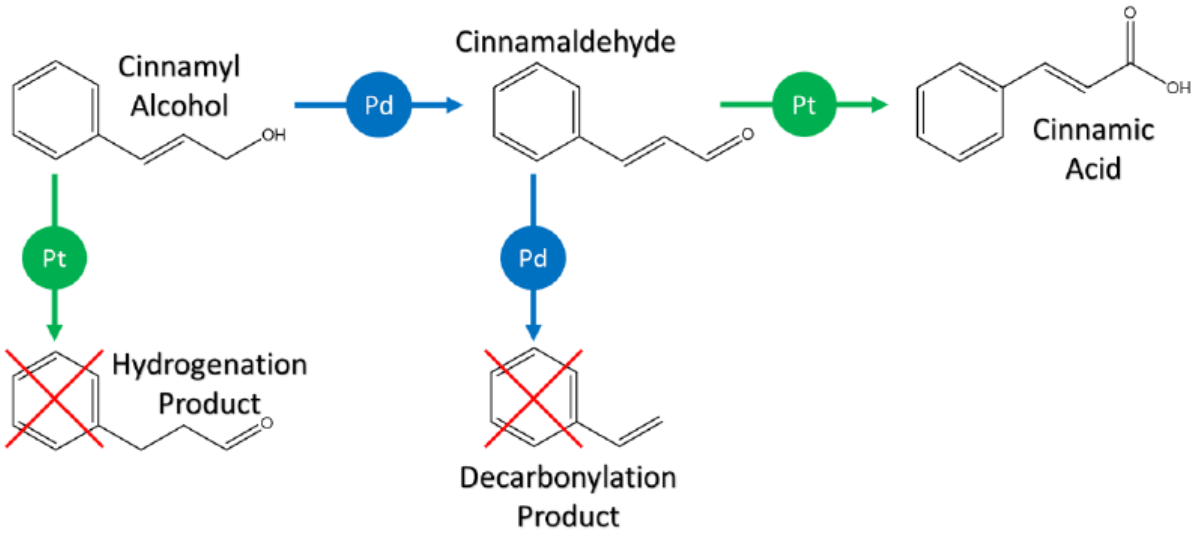

Figure 2.4: Selective oxidation pathways of cinnamyl alcohol to cinnamic acid using palladium and platinum species [137]

2.9 Summary

The increasing emissions of carbon dioxide paired with the finite nature of petroleum resources mean alternative fuel sources are imperative to reduce the impact of global warming. Biodiesel is an excellent replacement for petrochemical fuels, as it can be produced by renewable, non-competitive and reabsorbs all CO_2 emitted.

The current industrial practice uses homogeneous alkaline alkoxides and hydroxides catalysts to produce biodiesel, which requires aqueous quenching and neutralization steps to remove fatty acid impurities as well as difficult separation of products. Alternatively, a solid acid-base hierarchical material could esterify the fatty acid impurity, and transesterification of triglyceride compounds simultaneously in a tandem reaction, with easy separation through filtration. While many basic species can, and have been used successfully, alkaline earth oxide species are well suited to this reaction. Of this family of catalysts, MgO and CaO are very promising.

CHAPTER THREE

3.0 Materials and Experimental Techniques

This chapter focuses on the experimental methodology used in the work. The materials and chemicals used, the catalyst preparation method and characterization method were highlighted in this chapter. The materials and chemicals used were detailed in section 3.1. The order of methodology used in solving the problem were highlighted in section 3.2.1 - 3.2.6. the various characterization methods used in characterizing the catalyst were carefully highlighted in section 3.3. Various catalytic processes were performed to screen the catalysts created for transesterification reaction in section 3.4.

3.1 Chapter overview

The general outline of the project:

(i) Materials and chemicals

(ii) Catalyst preparation method:

3.2 Materials and Chemicals

All reagents used for this work were of analytical grade and needed no further purification as shown Table 3. 1- Table 3. 3

Below are the chemicals used.

Table 3. 1 Materials for synthesis

Chemical	Supplier	Purity
Pluronic 123 (P123)	Sigma Aldrich	MW 5800 g/mol^{-1}
Hydrochloric acid (HCl pH = 2)	VWR Chemicals	37%

Magnesium nitrate hexahydrate ($Mg(NO_3)_2.6H_2O$)	Sigma Aldrich	≥99%
Calcium nitrate tetrahydrate	Sigma Aldrich	≥99%
Potassium sulfate (K_2SO_4)	Sigma Aldrich	≥99%
Styrene	Sigma Aldrich	99%
Sodium Hydroxide	Sigma Aldrich	98%
Tetramethoxysilane (TMOS)	Sigma Aldrich	98%

Table 3. 2: Material for characterisation

Chemical	**Supplier**	**Purity**
Ammonium Fluoride (NH_4F)	Sigma Aldrich	98%
Sulphuric Acid (H_2SO_4)	Fisher	95%
Nitric acid (HNO_3)	VWR chemicals	64%
Boric acid (H_3BO_3)	Fluka	4%

Table 3. 3: Materials for catalytic testing

Chemical	Supplier	Purity
Tributyrin	Sigma Aldrich	97%
Tricaprylin	Sigma Aldrich	99%
Trilaurin	Tokyo Chemical Industry	98%
Dihexyl ether	Sigma Aldrich	97%
Methanol	VWR chemicals	100%
Butanol	Honeywell	99.4%

3.3 Experimental Methods

These catalysts were prepared using a method reported by Attard *et al* (1995) [47]. Therefore, a series of catalysts were prepared using varying masses of magnesium nitrate or calcium nitrate salts dissolved directly into the aqueous phase of the liquid crystal. The varying masses of the metal salt was to examine changes the amount of metal salt introduced to the sol-gel mixture might have on the mesoporous structure, as well as to prepare a range of catalysts for catalytic testing. The following sections (3.3.1 - 3.3.6) deal with the synthesis of polystyrene colloidal nanospheres and various catalysts supported on SBA-15 using the catalyst liquid crystal templating method.

3.3.1 Preparation of polystyrene colloidal nanospheres

This preparation was done in a 2 L Radleys reactor ready at 80^oC at 300 rpm. Deionised water was degassed under N_2 gas overnight. A 100 mL round-bottomed flask was charged with 0.33 g of potassium sulfate initiator and dissolved in 50 mL of deionized water and degassed under N_2 with stirring.

A 105 mL of styrene monomer was measured into a separating funnel. The polystyrene was washed with 100 mL of 1 M NaOH solution to remove the butyl catechol inhibitor. This was repeated 5 times and washed 5 times also with 100 mL deionized water. The washed polystyrene was added to the degassed water. The potassium sulfate solution was also added dropwise over 15 minutes. After 22 h of reaction, the solution was collected and centrifuged at 8000 rpm for 3 h and resulting solid was air dried to produce the polystyrene colloidal nanospheres also known as polystyrene beads. This was incorporated in course of preparation of catalyst to introduce macroporosity.

3.3.2 MgO/ Mesoporous SBA-15 catalyst using true liquid crystal templating method

2.00 g of P123 was weighed into a beaker and 2.00 g of HCl (pH = 2) was added. 0.25-1.50 g of magnesium nitrate hexahydrate was added to each beaker to obtain 5 different catalyst loadings. The above mixture was stirred for 1 h in an ultrasonic bath. 4.1 mL of TMOS was added to each beaker whiles stirring. Methanol produced from the hydrolysis and condensation of the TMOS silica source was then removed by vacuum drying at 40 °C overnight. The organic surfactant was then removed by calcining at $550^{o}C$ for 5 h at a heating rate of $5^{o}C$ /min. Materials were donated x wt.% MgO/(TLCT)SBA-15, where x is the weight percent of magnesium calculated through ICP-OES.

3.3.3 CaO/ Mesoporous SBA-15 catalyst using true liquid crystal templating method

These series of catalysts were prepared using the liquid crystal templating method used for mesoporous MgO/(TLCT)SBA-15 catalyst described in section 3.2.2 using the appropriate

calcium nitrate tetrahydrate of 0.40 g - 2.50 g to form 5 different loadings of the metal. Materials were donated x wt.% CaO/(TLCT)SBA-15, where x is the weight percent of calcium calculated through ICP-OES.

3.3.4 CaO/ Mesoporous SBA-15 at 800^{o}C using true liquid crystal templating method

Catalysts already prepared in section 3.2.3 were recalcined in the presence of oxygen. Materials were donated CaO/(TLCT)SBA-15 – 800.

3.3.5 MgO/ Mesomacroporous SBA-15 catalyst using true liquid crystal templating method

2.00 g of P123 and HCl (pH = 2) was weighed into a beaker. 0.25-1.50 g of magnesium nitrate hexahydrate was added to each beaker to obtain 5 different catalysts with varying amounts of magnesium nitrate. The solution was stirred in an ultrasonic bath for 1 h. 4.1 mL of TMOS was added to each beaker while stirring until a homogenous mixture is obtained. 6.00 g of polystyrene beads prepared in section 3.2.1 were added to each beaker whiles stirring. The resultant mixture was vacuum dried at 40 °C overnight and calcined at 550 °C for 5 h at a rate of 5 °C/min. Materials were donated x wt.% MgO/MM-(TLCT) SBA-15, where x is the weight percent of magnesium calculated through ICP-OES.

3.3.6 CaO/ Mesomacroporous SBA-15 catalyst using true liquid crystal templating method

These family of catalysts were prepared as described in section 3.2.4 using the appropriate calcium nitrate tetrahydrate ranging from 0.40 g to 2.50 g as used in section 3.2.4. Materials were donated

x wt.% CaO/MM-(TLCT) SBA-15, where x is the weight percent of calcium calculated through ICP-OES.

3.4 Material Characterization methods

These are characterization methods that were used to give the structural information, chemical compositional and physical analysis. Specifications of each equipment used in the characterization were provided

3.4.1 Inductively coupled plasma optical emission spectroscopy (ICP OES)

This is an analytical technique used to detect and quantify trace metals present in materials. Inductively coupled plasma is used to produce ions and excited electrons, which emit electromagnetic wavelength characteristic to particular elements. The intensity of the radiation is used to quantify the concentration of a particular metal when referenced to a calibration curve.

Optical emission spectroscopy was performed using a Thermo iCAP 700^0 calibrated against a series of standards between 1 and 100 ppm. Samples (10 mg) were digested using a mixture of ammonium fluoride (100 mg, Sigma Aldrich), sulfuric acid (2 cm^3, VWR chemicals), water (2 cm^3) and nitric acid (5 cm^3, VWR chemicals) prior to fluoride neutralization with boric acid (3% solution, 1 cm^3, Fluka). Acid digestion mixtures were diluted to 10% prior to analysis and measurements were repeated 3 times against 3 distinct wavelengths per element.

3.4.2 Powder X-Ray diffraction (XRD)

The Powder X-Ray diffractometer is used to determine the crystalline or amorphous nature of the material. In this method, X-ray from an X-Ray source strikes a polycrystalline at an incidence angle of 2θ and gives rise to a diffraction pattern. Atoms in a crystalline material are arranged in a certain regular manner forming planes which scatter the X-ray depending on the plane

spacing (d). The Bragg's Law can be used to describe the crystal structure of the material. [138] (Equation 3.1).

$$n\lambda = 2d \sin\theta$$

Equation 3.1: Bragg Formula

where n = order of interference (integer), **λ**= incident wavelength, d = lattice spacing and θ= diffraction angle.

XRD patterns were recorded with a Bruker D8 Advance diffractometer fitted with a LynxEye high-speed strip detector, both using CuKα (1.54Å) sources with a nickel filter, calibrated against Corundum (Bruker) standards. Low angle patterns were recorded over a range of 2θ = 0.3 - 8° (step-size 0.01°, scan speed 0.014° s^{-1}) and wide-angle patterns over a range of 2θ = 10 - 80° (step-size 0.02°, scan speed 0.020° s^{-1}).

3.4.3 Nitrogen absorption measurements

Nitrogen (N_2) absorption is an extremely useful technique, used to determine physical properties and structural characteristics of solid porous materials. Material properties are determined by the deposition and removal of nitrogen at known pressures. Nitrogen is added incrementally to the void above the sample, with the amount of N_2 absorbed being measures at specific pressures. Vacuum is applied in stages, to cause the nitrogen to desorb from the surface, which is also quantified. Nitrogen and argon are commonly used, although carbon monoxide and hydrogen can also be used. The adsorption/desorption behavior results in an isotherm, of which there are six types, as seen in Figure 3. 1, which are characteristic of the specific porous nature of the material.

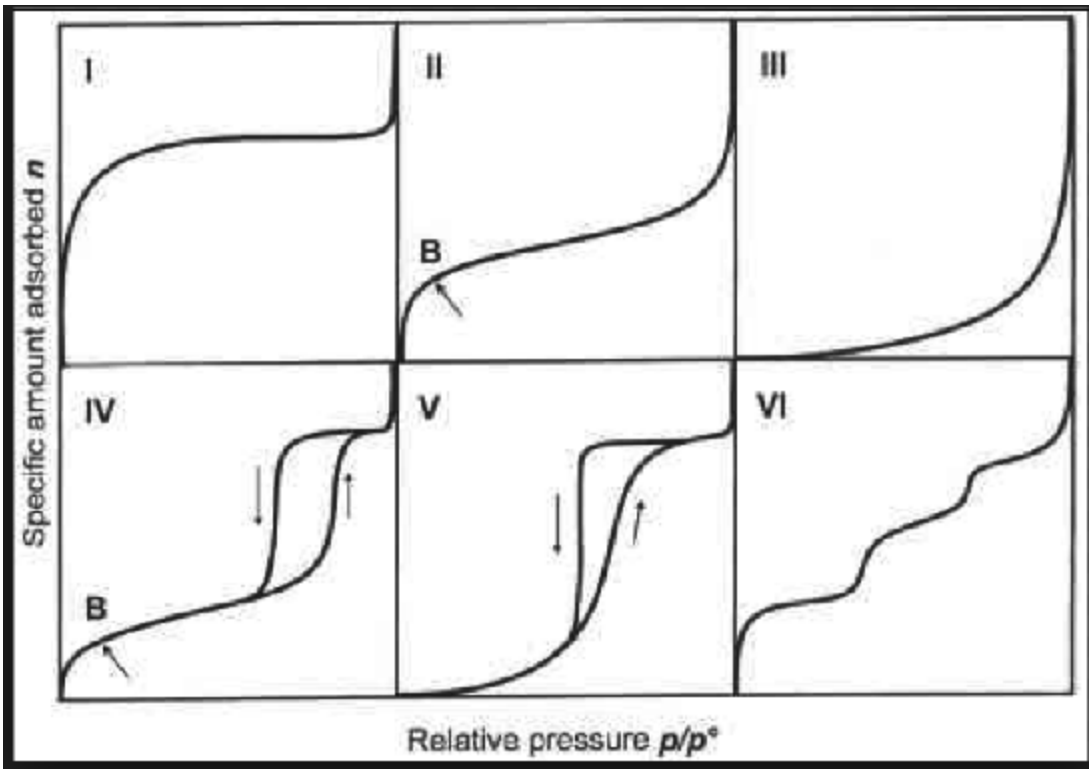

Figure 3. 1: Types of different isotherms [3]

The first isotherm, type I, is seen by microporous materials with strong interactions between absorbent and adsorbate, such as zeolites. Type II isotherms are typically materials lacking porosity and having weak interactions with the adsorbate. Type III isotherms are very rare, having a weak interaction with the gas. Type V isotherms are often from mesoporous or macroporous solids with weak interactions. Type VI isotherms are characteristic of well-defined uniform porous solids. Type IV isotherms are characteristic of SBA-15 and other ordered mesoporous solids and will be the most important for this work. They exhibit a hysteresis of the adsorption/desorption curve, which is observed due to nitrogen bound in the mesopores being trapped by the nitrogen adsorbed at the pore entrance.

The surface area is calculated using the Brunauer-Emmet-Teller (BET) equation [139], shown below (equation 3.2), and is conducted at a constant temperature of 77.5 K.

$$\frac{P}{V_{a(P_o-P)}} = \frac{1}{V_m C} + \frac{C-1}{V_M C}\left(\frac{P}{P_o}\right)$$

Equation 3.2: BET equation;

P = pressure, P_0 = saturation pressure, Va = volume adsorbed, Vm = monolayer volume, C = multilayer adsorption parameter

Porosity and surface area were measured using Quantochrome NOVA 4200e instrument by N_2 adsorption using Novawin v11.0 analysis software. Samples were degassed under vacuum at 120 °C for 24 h prior to analysis. Adsorption and desorption isotherms were recorded at -196 °C. BET surface areas were calculated over the relative pressure range 0.05-0.50 where a linear relationship was observed. Mesopore diameters were calculated applying the BJH method to the desorption branch. The material exposed to nitrogen physisorption adsorbs a certain volume of gas on its surface, and the instrument records the partial pressures at which this occurs, giving rise to isotherms of adsorption and desorption.

3.4.4 X-Ray Photoelectron Spectroscopy (XPS)

X-Ray photoelectron spectroscopy (XPS) is an analytical technique that is used to determine the surface of a material, providing information about the surface elemental composition and chemical environment of the sample being probed. The X-Ray photons excite and consequently eject core level electrons from the atoms in the sample. The binding energy of these electrons E_B; the energy required to promote an electron from a given electronic level to the Fermi level- is characteristic of the elements in the solid being investigated and it is this that gives rise to the discrete peaks in

an XP spectrum. The binding energy can be calculated by measuring the kinetic energy of the emitted electrons according to the following equation [140];

$$E_B = hv - E_K - \phi$$

Equation 3.3;

where E_B the binding energy of emitted electron, hv = the emitted X-Ray photon energy, E_K = the kinetic energy of the emitted electron, $\boldsymbol{\phi}$ = the spectrometer work function

XPS spectra were acquired using a Kratos Supra XPS fitted with a monochromated Al X-ray anode (1486.69 eV) and a charge neutraliser. All spectra were recorded with a base pressure below 10^8 Torr. Wide scans were acquired using a pass energy of 160, and high-resolution scans with a pass energy of 20. All spectra were calibrated to adventitious carbon (284.8 eV). All spectra were processed using CASAXPS v2.3.15 with backgrounds fit and subtracted using a Shirley baseline. GL (30) line shapes were used in all cases. Mg 2p XP peaks were fit using a FWHM of 2.20 eV and a doublet separation of 0.28 eV, Si 2p XP peaks were fit using a FWHM of 1.422 eV and a doublet separation of 0.61 eV and O 1s XP peaks were fit using a FWHM of 1.98 eV.

3.4.5 Thermogravimetric analysis-Mass Spectroscopy (TGA-DTA)

TGA checks the changes in the sample's mass on heating, which can provide useful compositional information about the materials of interest. Loss of water of crystallization, or of other adsorbed surface species, and decomposition of bulk phases resulting in the production of gases, can all be identified with this technique. DTA provides additional insight into thermal (endothermic or exothermic) processes occurring within the sample on heating, such as changes in state or crystalline structure, where a mass loss is not necessarily involved. This is achieved by computing the differences in temperature between the sample and inert reference material during heating.

Thermogravimetric analysis was conducted using Mettler-Toledo TGA/DSC 2 STAR* system at 10 ^{o}C min^{-1} under flowing N_2/O_2 (80:20 v/v 20 $cm^3.min^{-1}$) fitted with a Pfeiffer ThermoStar mas spectrometer.

3.4.6 Fourier Transform Infrared Spectroscopy (FTIR)

The infrared beam is focused onto the sample to allow it interact with the material in varying ways. Back reflected, diffusely scattered infrared radiation, which will have been partially absorbed by molecules within the sample is then collected by the Smart collector accessory which focuses the diffuse radiation onto the detector. Fourier-transformed infrared analysis was acquired using a Thermo Nicolet is 50 spectrophotometer fitted with a diamond ATR crystal. Data was analysed using OMNIC 9.2.98.

3.4.7 Scanning Electron Microscopy-Energy Dispersive X-Ray analysis (SEM - EDX analysis)

This technique has a large array of uses. However, the applications for this work are imaging the pore size, structure and thickness. It can also be used to determine particle size and shape, as well as elemental characterization. In scanning electron microscopy (SEM), a beam of electrons is directed onto the sample surface. On reaching the sample, the primary electrons lose energy through a variety of interactions, generating high energy backscattered electrons, secondary electrons through inelastic scattering and X-ray radiation. In secondary electron imaging (SEI) mode, utilized throughout this investigation, it is the secondary electrons that are detected and can give information relating to the topography of the sample [141]. The generated X-rays were also analysed with the energy dispersive X-ray (EDX) system attached to the SEM instrument. The process of EDX analysis is similar to XRF, with the only difference being the excitation radiation utilized [142] which in an EDX system is the beams of electrons generated by the SEM electron

gun. Fresh samples were analysed using JEOL 7800F Prime FEG SEM fitted with a BSE and SE detector. Samples were affixed by carbon tape and images were recorded at a probe current of 3 mA and an accelerating voltage between 1-15 kV.

3.4.8 Scanning Transmission Electron Microscope (STEM)

High resolution high angle annular dark field STEM images were acquired on an aberration-corrected JEOL 2100-F microscope at 200 kV and analysed using the ImageJ 1.41 software. Samples were dispersed in methanol and drop cast on 200-mesh carbon coated copper grids and dried under ambient conditions.

Electrons are emitted from an electron gun at the top of the microscope and then travel through a vacuum under the microscope. Electromagnetic lenses focus the electrons on a very thin beam so that it can go through the specimen. At the bottom of the microscope, the unscattered electrons hit a fluorescent screen, which gives rise to a "shadow image" of the specimen with its different parts displayed in varied darkness according to their density. Figure 3.2 shows a diagram of the STEM machine.

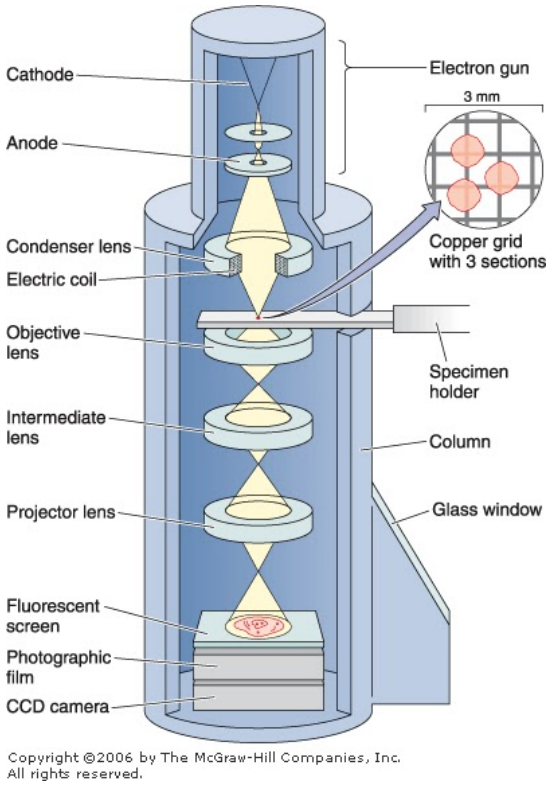

Figure 3.2: Schematic diagram of STEM [8]

3.5 Catalysis

3.5.1 Transesterification Reaction

Transesterification reactions were performed on a Radley's carousel at both 60 °C and 90 °C. At 60 °C, individual reaction tubes were charged with glyceryl tributyrate (0.01 mol, Aldrich, 98%) in methanol (12.2 mL), with dihexyl ether (0.001 mol, Aldrich, 97%) as an internal standard. Reactions were performed in air with 50 mg of catalyst. At 90 °C, Compositional analysis of periodically withdrawn, quenched aliquots were performed on using a calibrated Shimazu GC-2010 fitted with a CP-5 column. Higher triglycerides such as tricaprylin used in the course of experiment required the use of 37 wt. % of butanol (Honeywell, 99.4%) on a Radley's batch reactor

at 90 ºC. The reaction preceded in Ace pressure flasks fitted with a sampling vent stirred at 700 rpm in excess methanol. Initial rates of the catalysts were determined over the first part of the reaction, when conversion rises linearly as a function of time, typically within 60 – 120 mins. An example calculation for 1.5 wt.% MgO/ (TLCT) SBA-15 is outlined in Figure 3. 3.

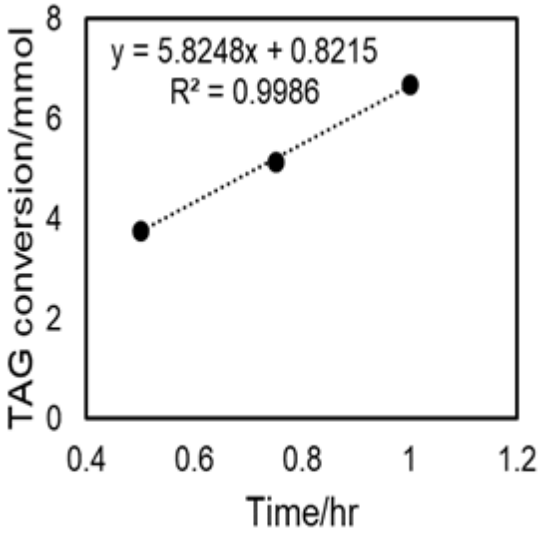

Figure 3. 3: Linear portion of a reaction profile for transesterification of tributyrin over MgO/ (TLCT) SBA-15 for calculation of initial activity

Example calculation of initial activity;

Conversion per min (taken from gradient in Figure 3. 3**: 5.8248 mmol.hr^{-1}**

CHAPTER FOUR

4.0 Results and Discussion

This chapter presents and discusses the characterization of all synthesized heterogenous catalysts for transesterification reaction. The results of the characterization and catalytic activity for transesterification were discussed as well.

4.1 Catalyst Support Characterisation: MgO/TLCT SBA-15 and MgO/(TLCT) MM-SBA-15, CaO/TLCT SBA-15 and CaO/(TLCT) MM-SBA-15

Magnesia supported on mesoporous and meso-macroporous materials and also calcium supported on mesoporous and meso-macroporous materials using the cooperative self-assembly method were synthesized. These family of materials were characterized using variety of analytical techniques such as XRD, ICP-OES, N_2 porosimetry, XPS, FTIR, TGA-MS, SEM and TEM to give the structural information, chemical compositional and physical analysis.

4.1.1 X-Ray Diffraction

X-ray diffractometry was performed to obtain the structural information and crystal identification of the synthesized materials. Low angle XRD pattern of an undoped (TLCT) SBA-15 found in the top right corner of Figure 4.1(I) show 3 peaks characteristic of the two-dimensional *P6mm* hexagonal ordering of the long-range ordered SBA-15 pore network which is the (100), (110) and (200) reflections. Figure 4.1 (I & II) show low angle XRD patterns for synthesized mesoporous MgO/(TLCT) SBA-15 and CaO/TLCT SBA-15 respectively and Figure 4.2 (III – IV) show low angle XRD patterns for synthesized MgO/(TLCT) MM-SBA-15 and CaO/(TLCT) MM-SBA-15 respectively. All synthesized materials for both mesoporous and hierarchical exhibit the typical two-dimensional hexagonal pore orders of *p6mm* space group identical to that of (TLCT) SBA-15

as shown in Figure 4.1(I), an indication of the presence of mesoscopic order in these nanosynthesized composites. This mesoscopic order is favourable with those reported in highly dispersed PtCo nanoparticles on micro/nano-structured pyrolytic carbon from refined sugar for methanol electro-oxidation in acid media [143]. This mesoscopic order is evident due to the presence of (100), (110), (200) peaks that show long-range ordering. Due to the nature of liquid crystals, the long-range order is present; as such the (110) and (200) reflections are observed, however some of these reflections can be rather weak, and on occasion, be difficult to identify. It is observed from Figure 4.1(II) that the highest loading of calcium precursor salts in CaO/TLCT SBA-15 showed the presence of only the (100) peak. This distortion in the (110) and (200) reflections can be as a result of increased mass loading of calcium oxide interrupting the crystallinity of the material. This shows a less ordered structure but although there are peaks of long-range order still maintained. For CaO/(TLCT) MM-SBA-15 from Figure 4.2 (IV), there was a drastic decrease in the (100) peaks upon addition of higher amounts of precursor salts. Fewer crystallinity reflections of the silica phases show higher amounts of amorphocity due to the addition of polystyrene beads for macroporosity [144].

Figure 4.3 (V & VI) show the wide-angle XRD patterns for MgO/(TLCT) SBA-15 and CaO/(TLCT) SBA-15 respectively and Figure 4.4(VII-VIII) shows the wide-angle XRD patterns for, MgO/(TLCT) MM-SBA-15 and CaO/(TLCT) MM-SBA-15 respectively. All synthesized materials do not show large agglomerate particles of MgO crystallization periclase phases and CaO nanoparticles, which indicate that the MgO and CaO nanoparticles are evenly dispersed in the SBA-15 silica support. However, CaO/(TLCT) SBA-15 in Figure 4.3(VI) and CaO/(TLCT) MM-SBA-15 in Figure 4.4(VIII), it is observed that there are surface carbonate species found at 2θ of 29° to 30° from CaO conversion into $CaCO_3$ [145](see section 4.1.6; TGA-MS). It is also

shown that all synthesized materials show a distinctive broad peak at 2θ of 25º indicative of amorphous silica. This could be an indication that there was unsuccessful impregnation of magnesium and calcium precursor salts into silica support. To determine if this is true, inductively coupled plasma elemental analysis was conducted on all synthesized materials to check the actual mass of MgO and CaO present in the mesopores of the SBA-15 respectively. It is clearly evident that wide angle XRD (WAXRD) run for both CaO/(TLCT) SBA-15 (mesoporous) and CaO/MM-(TLCT) SBA-15 (hierarchical) found in Figure 4.3(VI) and Figure 4.4(VIII) showed the presence of calcium carbonates formation at approximately 27 ºC to 30 ºC. Reactions run based on these materials showed that initial rate of reaction for tributyrin reaction in Figure 4.4 (VII) and (VIII) did not increase as calcium contents increased greatly. This phenomenon could be as a result of carbonate poisoning which hindered the reaction profile during the first 1 hour of the catalytic reaction of the tributyrin. TGA-MS data analysis of both mesoporous and hierarchical materials in Figure 4. 19 (II) and Figure 4. 20 (II) shows the presence of desorption of calcium carbonates at a temperature of 580 ºC to 800 ºC. Due to the presence of surface carbonates, mesoporous materials were then recalcined at 800 ºC in the presence of oxygen. This was done to oxidize all the calcium carbonates to form calcium oxide and carbondioxide which further escapes. Wide angle and low angle XRD were performed on the lowest (3.59 wt.%) and highest (18.62 wt.%) series of CaO/(TLCT) SBA-15 to provide the structural information after the catalysts were subjected to 800 ºC under oxygen.

From Figure 4. 5 (IX), 3.59 wt.% CaO/(TLCT) SBA-15- 800, WAXRD show a distinctive broad peak 20 ºC-30 ºC indicative of amorphous silica with no other distinctive peak. For 18.62 wt.% of CaO/(TLCT) SBA-15, the distinctive broad peak was distorted and this could be as a result of

breakage of the silica structure by subjecting it to high temperature and also an increase in the calcium species.

LAXRD is shown in Figure 4. 5 (X) for 3.59 wt.% CaO/(TLCT) SBA-15-800 maintained into mesoporosity by exhibiting well-defined peaks associated with the (100), (110) and (200) planes of the *p6mm* space group for the hexagonal arrangement of mesoporous channels. Addition of more calcium species destroyed the long-range order of the mesostructured phase. The crystallinity of (100) decrease to a high extent.

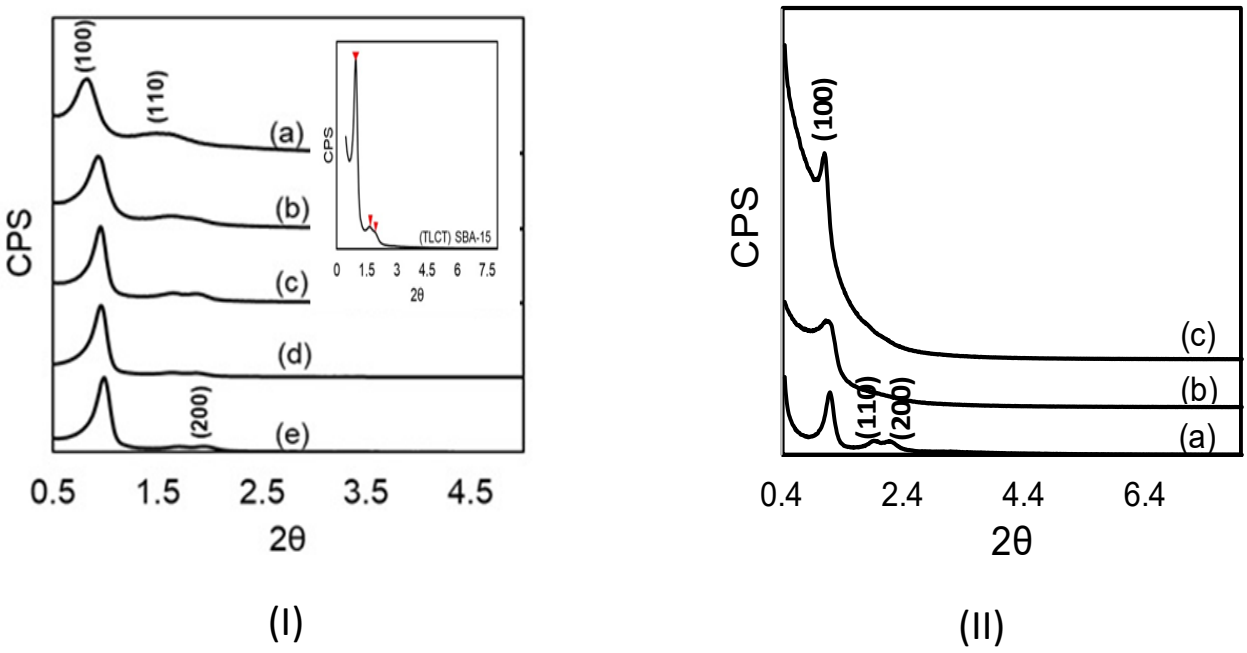

Figure 4.1: XRD patterns of; (I) Low angle X-ray diffraction pattern of MgO/(TLCT) SBA-15 (a-e): 1.45 wt.%, 3.03 wt.%, 5.05 wt.%, 5.66 wt.%, 8.33 wt.% of MgO in the mesopores of SBA-15, (II): Low angle X-ray diffraction pattern (LAXRD) of CaO/(TLCT) SBA-15 (a-c): 3.59 wt.%, 11.03 wt.%, 18.62 wt.% CaO in mesopores of SBA-15

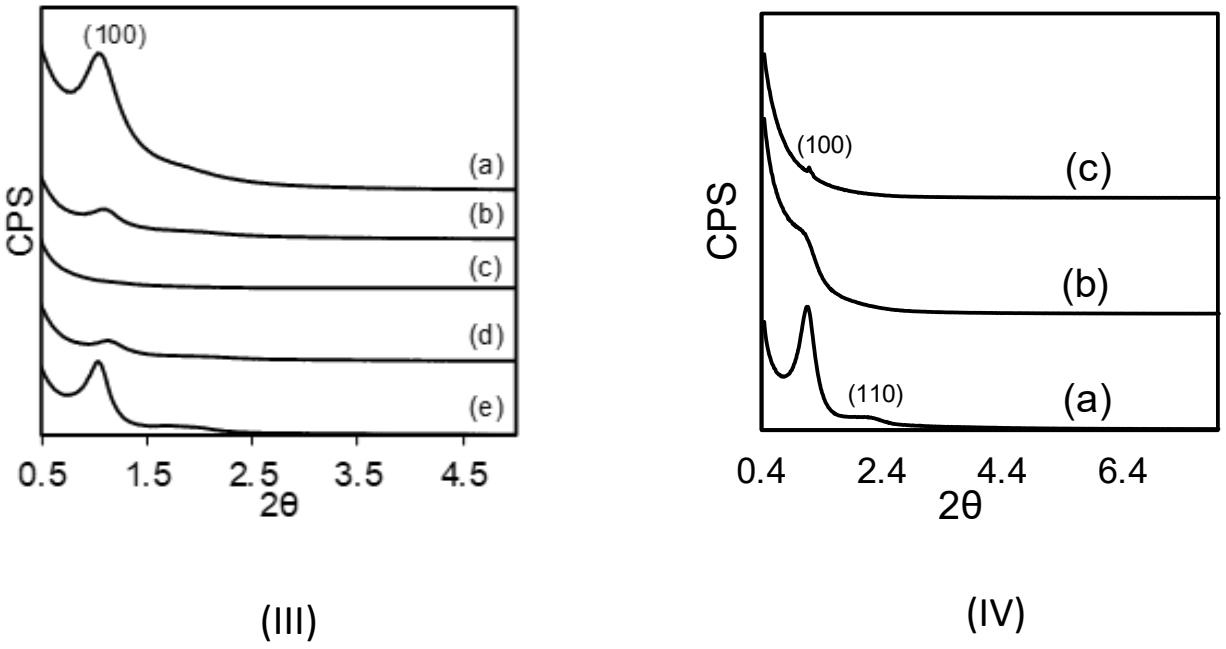

Figure 4.2: XRD patterns showing; (III) Low angle X-ray diffraction pattern (LAXRD) of MgO/MM TLCT-SBA-15 (a-e): 3.07 wt.%, 3.26 wt.%, 4.46 wt.%, 6.90 wt.%, 8.51 wt.% MgO in mesomacropores of SBA-15, (IV): Low angle XRD diffractograms of CaO/MM TLCT SBA-15 (a-c): 3.39 wt.%, 10.59 wt.%, 15.78 wt.% of CaO in mesomacropores of SBA-15

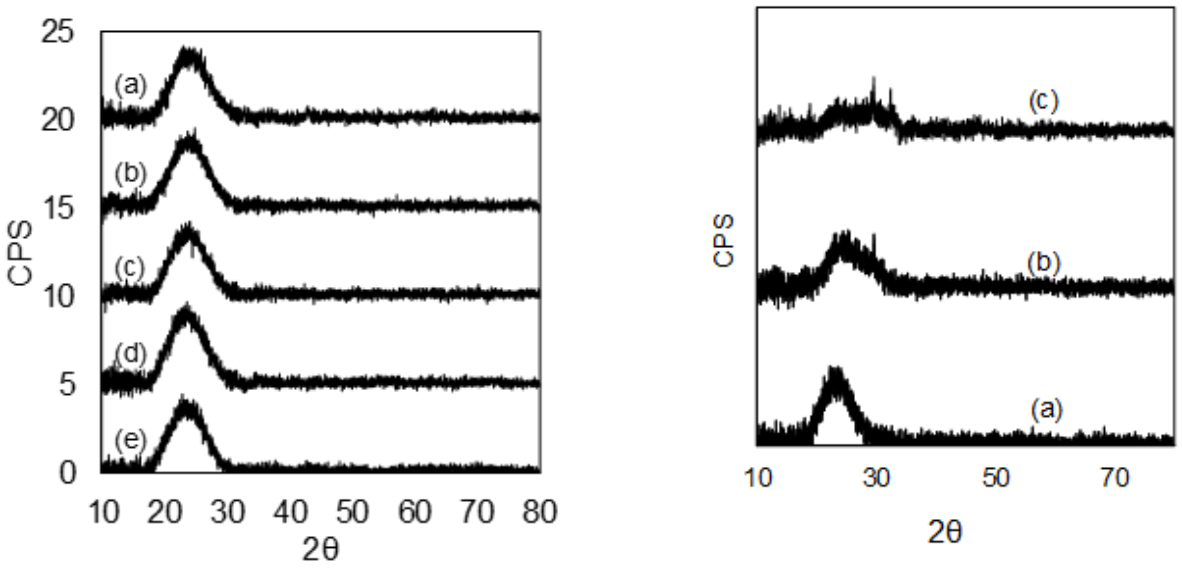

(V) (VI)

Figure 4.3: XRD patterns showing; (V) Wide angle X-Ray diffraction pattern (WAXRD) of MgO/(TLCT) SBA-15 (a-e): 1.45 wt.%, 3.03 wt.%, 5.05 wt.%, 5.66 wt.%, 8.33 wt.% of MgO in the mesopores of SBA-15 (VI) Wide angle X-Ray diffraction pattern (WAXRD) of CaO/(TLCT) SBA-15 (a-c): 3.59 wt.%, 11.03 wt.%, 18.62 wt.% CaO in mesopores of SBA-15

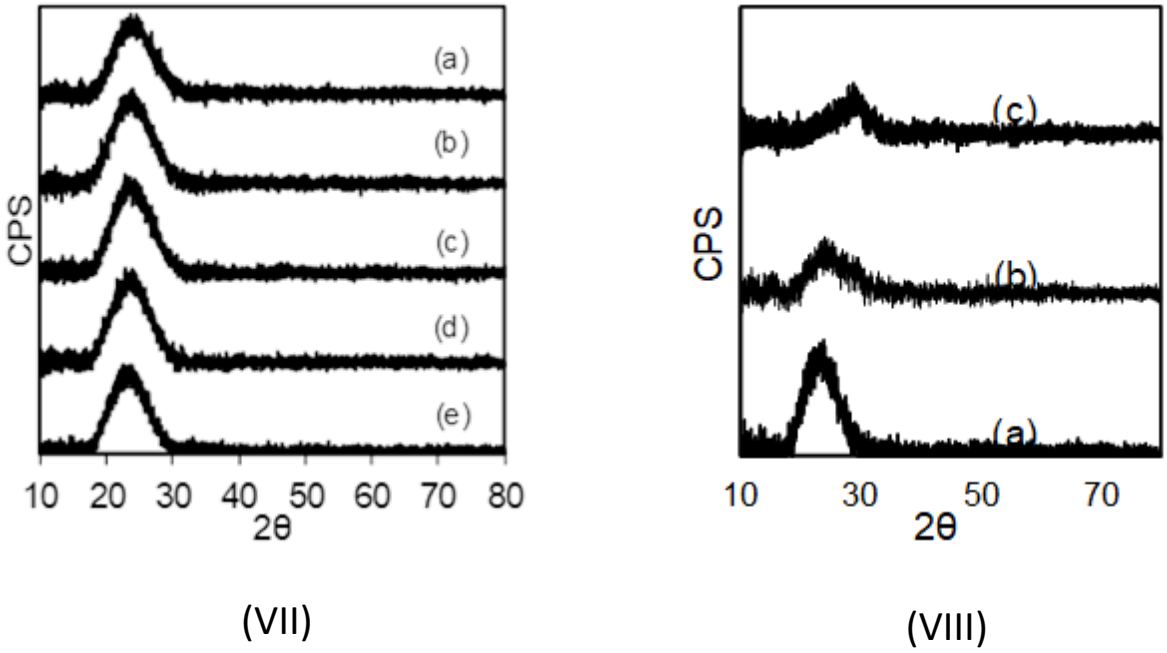

Figure 4.4: XRD patterns showing; (VII) Wide angle X-Ray diffraction pattern (WAXRD) of MgO/MM TLCT-SBA-15 (a-e): 3.07 wt.%, 3.26 wt.%, 4.46 wt.%, 6.90 wt.%, 8.51 wt.% (VIII) CaO/MM TLCT SBA-15 (a-c): 3.39 wt.%, 10.59 wt.%, 15.78 wt.% of CaO in mesomacropores of SBA-15

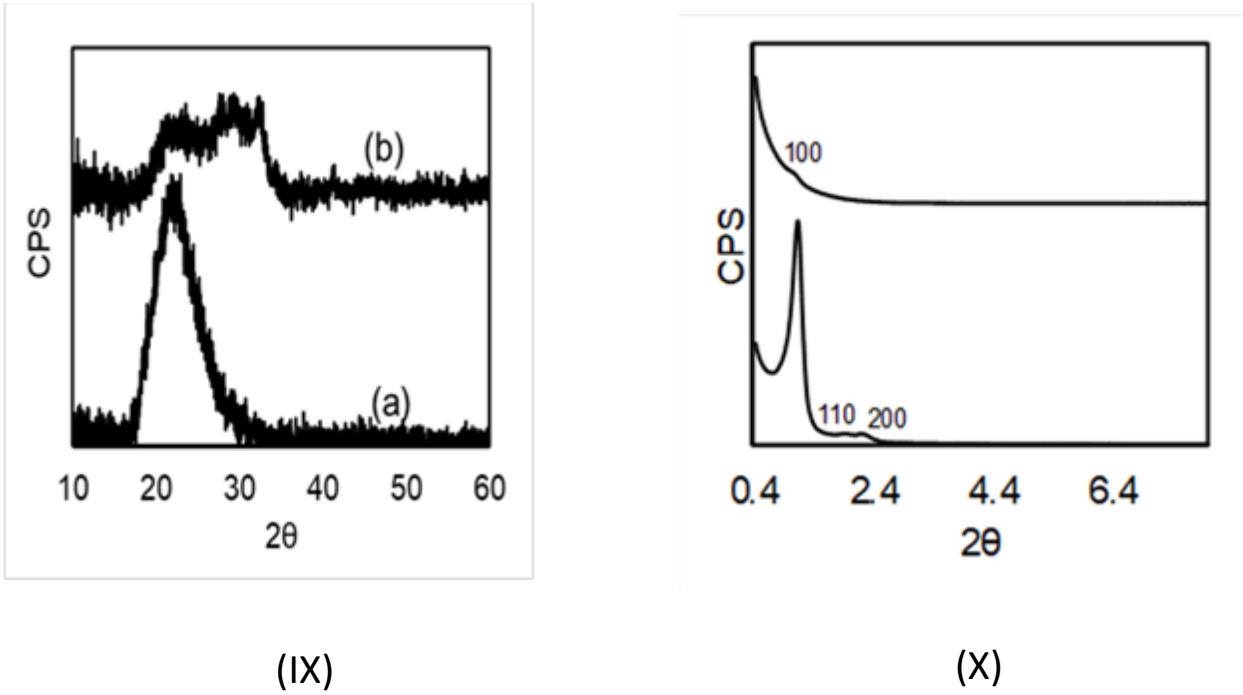

(IX) (X)

Figure 4. 5: XRD patterns showing; (IX) Wide angle XRD diffractograms for CaO/(TLCT) SBA-15 diffractograms (a & b): 3.59 wt.%, 18.62 wt.% of CaO in mesopores of SBA-15 after recalcination at 800 ºC (X) Low angle XRD diffractograms exhibiting *p6mm* symmetry after recalcination at 800 ºC to eliminate surface carbonates

4.1.2 Inductively coupled plasma optical emission spectroscopy (ICP OES)

ICP OES was performed on MgO/(TLCT) SBA-15(Figure 4. 6 I), CaO/(TLCT) SBA-15 (Figure 4. 6, II), MgO/MM TLCT-SBA-15 (Figure 4.7 III) and CaO/MM TLCT SBA-15 (Figure 4.7 IV)to determine the actual bulk weight percentages of magnesium oxide or calcium oxide impregnated into SBA-15 silica support after a mass of magnesium nitrate and calcium nitrate precursor solutions have been added. Nominal weight percentages were calculated assuming a 100% yield of silica condensation as expected per calculation when precursor solutions are incorporated into silica support. This quantitative elemental analysis determined that magnesium and calcium have been successfully functionalized into the SBA-15 silica support in a linear trend near to the

nominal loading. Both MgO/(TLCT) SBA-15 and MgO/MM-(TLCT) SBA-15 show a linear decrease near to the linear trend in the actual weight percentages as precursor solution was incorporated into the silica support. CaO/(TLCT) SBA-15 and CaO/MM TLCT SBA-15 show a linear increase above nominal loading.

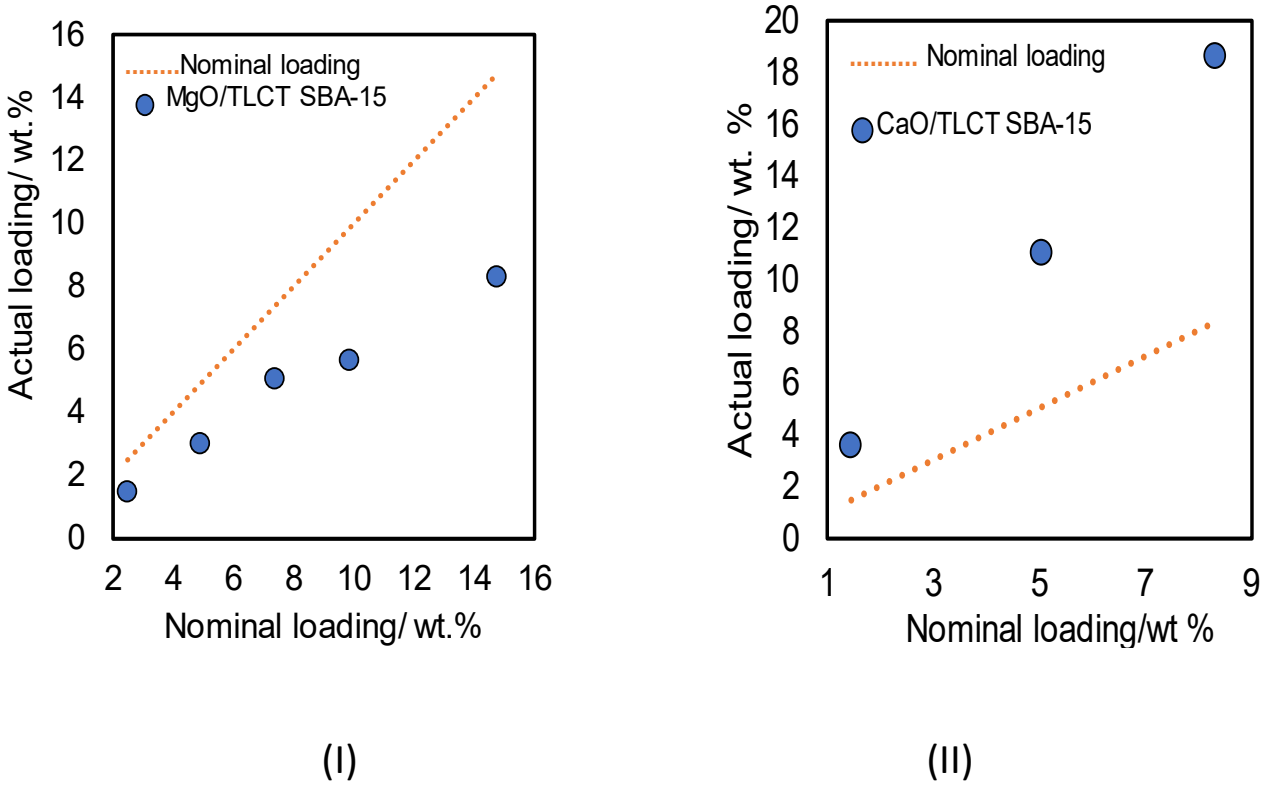

Figure 4. 6: ICP-OES results showing; (I) Magnesium weight percentage in the MgO/(TLCT) SBA-15 (II) Calcium weight percentage present in CaO/(TLCT) SBA-15 materials

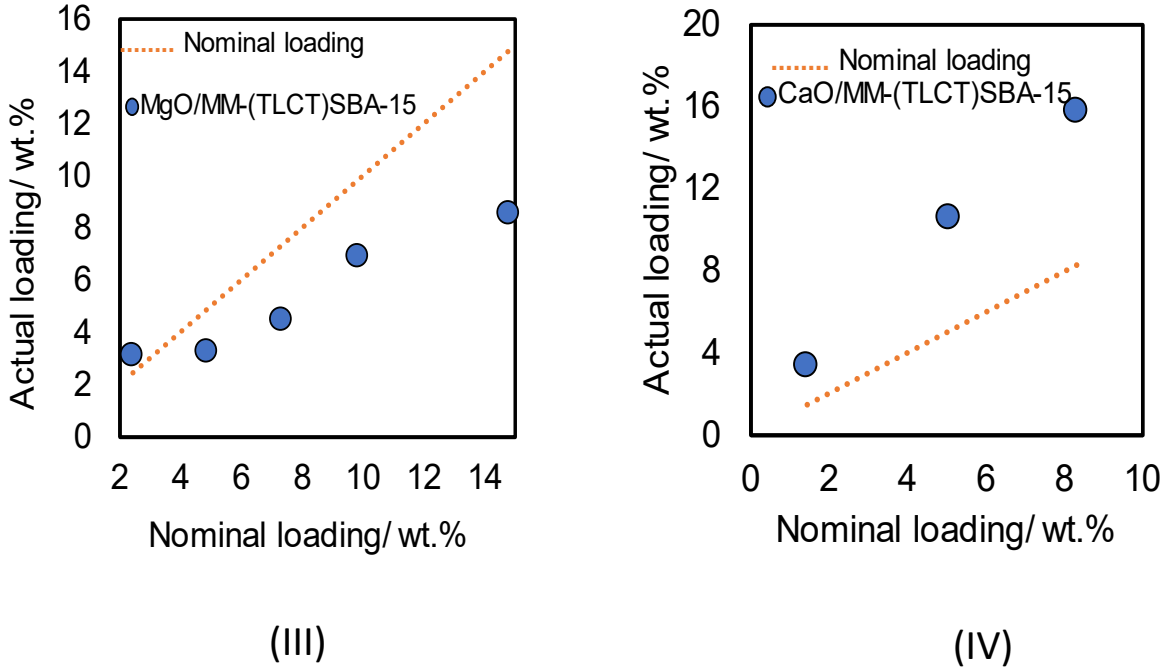

Figure 4.7: ICP-OES results showing; (III) Magnesium weight percentage in the MgO/MM-(TLCT) SBA-15, (IV) Calcium weight percentage present in CaO/MM-(TLCT) SBA-15 materials, plotted against their nominal loading.

4.1.3 Nitrogen Porosimetry

The Brunauer-Emmett-Teller (BET) nitrogen adsorption analysis was used to determine the surface area of the materials. Unfunctionalized SBA-15 silica support found on the top right corner of Figure 4. 8 (I) shows the presence of type IV of the H1 hysteresis loop which confirms a mesoporous structure as discussed in "in situ coating of SBA-15 with MgO" [146]. The in situ preparation method has higher surface areas, pore diameters as compared to incipient wetness impregnation method [116]. This proves that "in situ preparation" method maintains the mesostructured nature of SBA-15 whiles introducing basicity in synthesised materials. It was found that all the synthesized MgO/(TLCT) SBA-15 showed the presence of the hysteresis curves in Figure 4. 8 (I), which confirms an ordered mesoporous material was synthesized. The pore size

distribution was evaluated from the BJH plots as shown in Figure 4. 8 (II). 1.45 wt.% and 3.03 wt.% of MgO/(TLCT) SBA-15 shows a wide pore size distribution around 5 nm while 5.05 wt.% showed two maxima of pore size distribution around 3 nm and 5 nm leaving 6.51 wt.% and 8.33 wt.% with pores size distribution around 3 nm as discussed by Zhao *et al* [115]. The larger pores happen to be more remnant of the primary mesopores of MgO/(TLCT) SBA-15. Table 4. 1 shows a decrease in the mean pore diameter as the magnesium content increases until approximately 5 wt.% Mg loading, where it plateau's at approximately 3.5 nm. This initial decrease in mean pore diameter could be attributed to this increasing amount of magnesium nanoparticles present inside the mesoporous domain. The plateau witnessed above four percent could indicate the pore network has become saturated with magnesium, and therefore forming magnesium oxide outside the pores on the bulk. Higher pore diameters are reported in this work as compared to the ones discussed by *Eugena et al* [116]. The surface area exhibits an increasing trend from 470 $m^2. g^{-1}$ to 550 $m^2. g^{-1}$ as magnesium content is increased in Table 4. 1 as discussed in the literature for transesterification of vegetable oil to biodiesel over MgO functionalized mesoporous catalysts [116].

Similarly, for CaO/(TLCT) SBA-15 in Figure 4. 9(III), all the isotherms were of type IV of H1 hysteresis loop very similar to SBA-15. This strongly shows that a pure silica SBA-15 and all synthesized CaO/(TLCT) SBA-15 are of the ordered mesoporous structure. However, there was a decrease in the hysteresis loop due to high loading of calcium in the SBA-15 which led to saturation or blockage of pores by the CaO particles as observed by *Amos et al* [147]. BJH plots from Figure 4. 9(IV) shows a wide pore size distribution around 4 nm, however, the lowest loading (3.59 wt.%) had two maxima of pore size distribution around 4 nm and 5 nm. However, the pore distribution around 4 nm is dominating. The highest loading (18.63 wt.%) had an extremely wider pore size distribution. This could be due to the formation of newer pores. Tabulated values as

shown in Table 4. 2 showed a drastic decrease in surface area from 400 $m^2 . g^{-1}$ to 200 $m^2 . g^{-1}$. There was an interesting trend in the pore diameter as calcium content increased. This phenomenon could be further explained using more experimental data. These results show that there can be confidence that the addition of the magnesium or calcium nitrate salt does not detrimentally affect the mesophase of the surfactant or the condensation of the silica, allowing SBA-15 like mesoporous silica containing magnesium oxide and calcium oxide nanoparticles to be prepared by a cheap one-pot synthesis approach. These results are in agreement with the discussion made by Wang *et al* [145].

Figure 4.10 shows the N_2 adsorption isotherms and pore size distributions for MgO/MM-(TLCT) SBA-15 (V and VI) and CaO/MM-(TLCT) SBA-15 (VII and VIII) respectively. It can be seen from Figure 4.10(V), that the isotherms of all synthesized catalysts can be described as type IV with H1 hysteresis loop which is typical of SBA-15 with pore diameters within the range of 3.00 – 3.45nm. There is, however, a constriction in the hysteresis loop as magnesium content increases. This may be due to the formation of new pores with smaller sizes probably due to the blockage of mesopores. From Figure 4.10(VI), pore size distribution curve was obtained from BJH plots. There is, however, a wide pore size distribution around 3.5 nm as magnesium content increases. However, the lowest loading of MgO/MM-(TLCT) SBA-15 has three possible maxima of pore size distribution that occurs around 3.5nm, 4nm and 6nm but the larger pores happen to be more remnant of the primary mesopore of MgO/MM-(TLCT) SBA-15. From Table 4. 3, textural information shows an increase in pore volume as magnesium content increased. BET surface areas were within 550 $m^2 . g^{-1}$ to 610 $m^2 . g^{-1}$. A typical adsorption-desorption isotherm for the series shown in Figure 4. 11(VII) is a typical IV hysteresis loop characterization of mesoporous materials with pore diameters between 3.4 nm to 3.8 nm. There is a reduction in the hysteresis loop as

calcium content is increased. The difference in the lower adsorption branch and upper desorption portion of the hysteresis loop reflect the mechanisms of pore filling and emptying which occurs *via* capillary condensation and evaporation [148]. The more detailed structural analysis was obtained from the BJH plots from Figure 4. 11(VIII). There was a wider pore size distribution around 3 nm dominant for all catalysts. There was a reduction in the pores size distribution as calcium content increased. This could be associated with the formation of new pores. Table 4. 4 showed the BET surfaces areas within 410 $m^2. g^{-1}$ and 460 $m^2. g^{-1}$ with a decreasing pore volume as calcium content is increased.

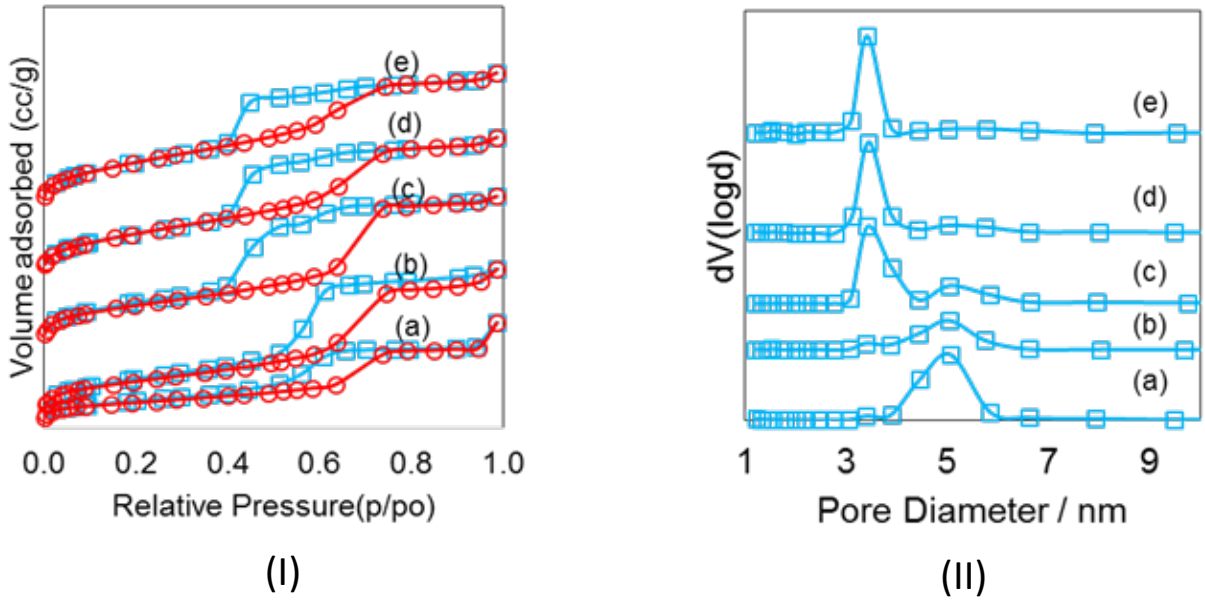

Figure 4. 8: (I) N_2 adsorption isotherms exhibiting typical IV character with H1 hysteresis loop (a-e): 1.45wt.%, 3.03 wt.%, 5.05 wt.%, 5.66 wt.%, 8.33 wt.% MgO/(TLCT) SBA-15, (II) BJH plots of MgO/(TLCT) SBA-15 (a-e): 1.45wt.%, 3.03 wt.%, 5.05 wt.%, 5.66 wt.%, 8.33 wt.% MgO/(TLCT) SBA-15

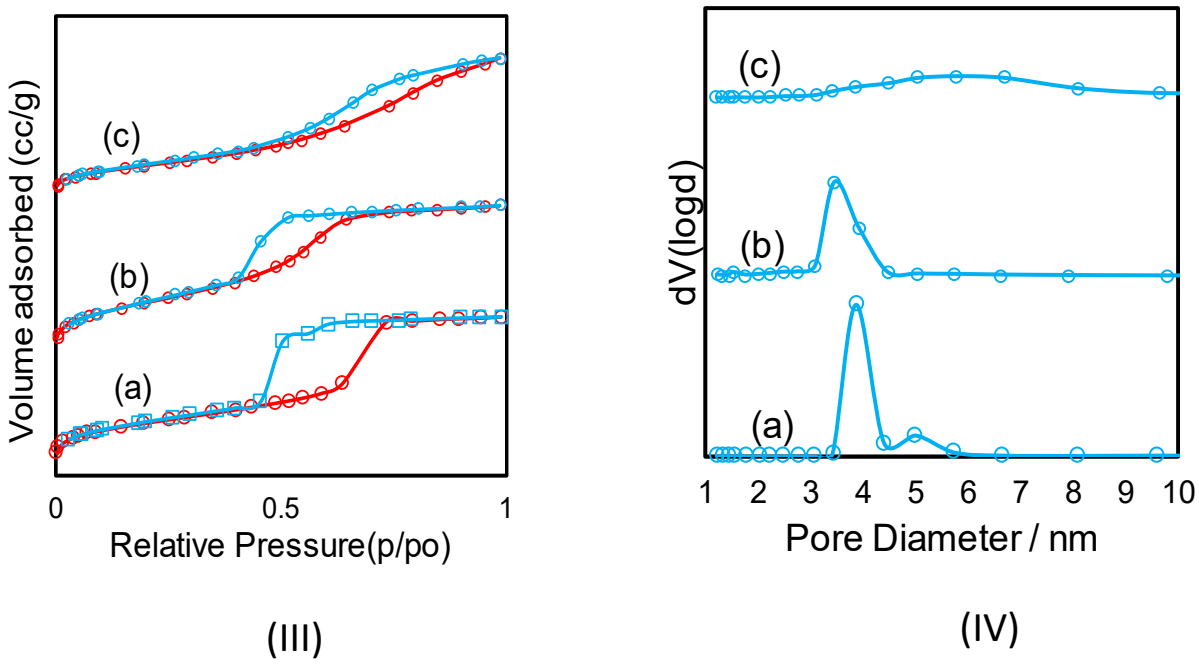

Figure 4. 9: (III) N_2 adsorption isotherms exhibiting typical IV character with H1 hysteresis loop (a-c): 3.59 wt.%, 11.03 wt.%, 18.63 wt.% CaO in the mesopores of SBA-15, (IV) BJH plots with increased $CaNO_3$ (a-c): 3.59 wt.%, 11.03 wt.%, 18.63 wt.% CaO in the mesopores of SBA-15

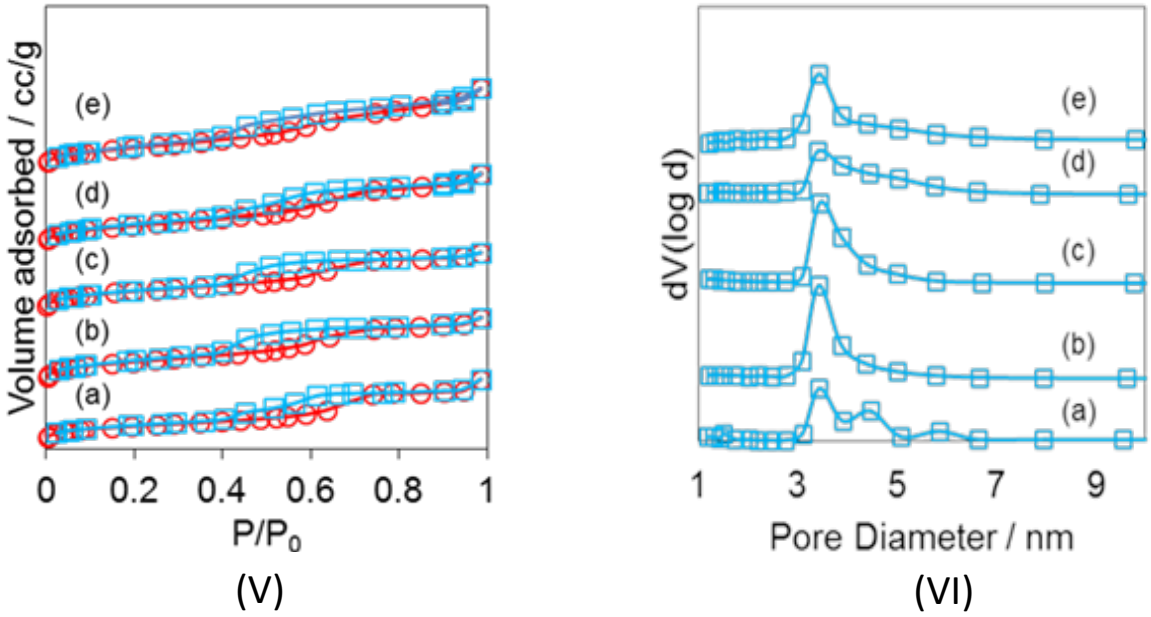

Figure 4.10: (V) N_2 adsorption isotherms of MgO/ MM-(TLCT) SBA-15 exhibiting typical IV character with H1 hysteresis loop (a-e): 3.07 wt.%, 3.26 wt.%, 4.46 wt.%, 6.90 wt.%, 8.51 wt.% MgO in mesomacropores of SBA-15, (VI) BJH plots of MgO/ MM-(TLCT) SBA-15 (a-e): 3.07 wt.%, 3.26 wt.%, 4.46 wt.%, 6.90 wt.%, 8.51 wt.% MgO in mesomacropores of SBA-15

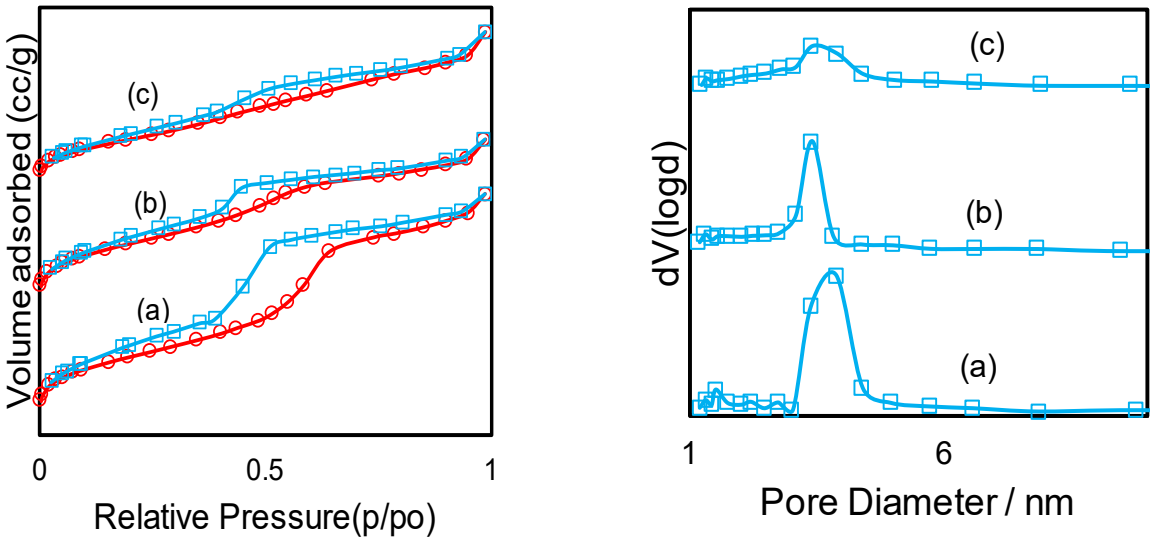

(VII) (VIII)

Figure 4. 11: (VII) N_2 adsorption isotherms of CaO/MM-(TLCT) SBA-15 exhibiting typical IV character with H1 hysteresis loop (a-c): 3.39 wt.%, 10.59 wt.%, 15.78 wt.% of CaO in mesomacropores of SBA-15, (VIII) BJH plots of CaO/MM-(TLCT) SBA-15 (a-c): 3.59 wt.%, 11.03 wt.%, 18.63 wt.% CaO in the mesopores of SBA-15

Table 4. 1: Tabulated values for surface area and pore diameters and pore volumes for MgO/(TLCT)SBA-15 materials

Mg wt.%	Surface area /m^2. g^{-1}	Pore diameter(nm)	Pore volume ($cc.g^{-1}$)
1.46	470	5.06	0.685
3.02	250	5.03	0.367
5.05	530	3.42	0.751
5.66	550	3.44	0.678
8.33	570	3.41	0.656

Table 4. 2: Tabulated values for surface area and pore diameters and pore volumes for CaO/(TLCT)SBA-15 materials

Ca/wt. %	Surface area / m^2. g^{-1}	Pore diameter/nm	Pore volume/cc. g^{-1}
3.59	405.100	3.863	0.577
11.03	453.676	3.449	0.576
18.62	263.432	5.032	0.498

Table 4. 3: Tabulated values for surface area and pore diameters and pore volumes for MgO/MM-(TLCT) SBA-15 materials

Mass of $MgNO_3$/g	Surface Area/m^2. g^{-1}	Pore diameter/nm	Pore volume/cc. g^{-1}
0.25	550	3.43	0.629
0.50	650	3.42	0.719
0.75	610	3.45	0.654
1.00	600	3.41	0.784
1.50	610	3.42	0.867

Table 4. 4: Tabulated values for surface area and pore diameters and pore volumes for CaO/MM-(TLCT) SBA-15 materials

Ca/wt. %	Surface area / $m^2 . g^{-1}$	Pore diameter/nm	Pore volume/cc. g^{-1}
3.59	462.798	3.882	0.632
11.03	413.360	3.411	0.443
18.62	310.306	3.408	0.388

4.1.4 X-Ray Photoelectron Spectroscopy (XPS)

X-Ray photoelectron effect was further employed to quantitatively assess the differences in surface electronic structure and therefore basicity of the samples. The use of spectroscopic techniques allows direct measurement of surface basicity, without the need for chemical probes or titrant that could interact with the basic sites. XPS data analysis was performed for MgO/(TLCT) SBA-15 from Figure 4.12 (I) - Figure 4.14 (V) and MgO/MM-(TLCT) SBA-15 from Figure 4.14 (VI) - Figure 4. 16(X) to provide the surface properties as magnesium weight content was increased. As shown in Figure 4.12, the binding energies of Mg *2p* and Si *2p* were 52.0 eV and 103.5eV respectively. Figure 4.12 (I) shows the resultant Mg *2p* XPS stack spectra indicating deconvoluted Mg-O-Mg and Mg-O-Si species for mesoporous SBA-15 as well as Figure 4.12 (II) shows the Si spectra indicating deconvoluted Mg-O-Mg and Mg-O-Si species for mesoporous SBA-15 in agreement with XPS data discussed by Wang et al [149]. This is in agreement with ICP data that confirms the existence of MgO. A graph of bulk weight percentages obtained from ICP to surface ratios of Mg weight percentages was obtained from the deconvolution of Mg and Si XP spectra can be found in Figure 4.13 (III). From the graph, it shows that an increased in the bulk Mg weight percentages obtained from the ICP caused an increase in the surface weight percentage of Mg. It can also be observed that the highest loading of Mg on SBA-15, which is 8.33 wt. % yielded about

2.50 wt. % of Mg on the surface of the silica framework. This attests to the fact that most of the Mg content of about approximately 5.83 wt. % can be found in the mesopores of the SBA-15 framework. This observation can be seen in the lower loading catalysts as well. Figure 4.13(IV) shows graphs from the deconvolution of Mg and Si XP spectra. From the graph, it can be observed that there is an increase in Mg-O-Mg bonds and a decrease in the Mg-O-Si bonds as Mg content was increased. This could be associated with the formation of more Mg-O-Mg bonds as well as isolated species of Mg-O-Mg as magnesium content was increased. Figure 4.14 (V) shows clearly the increase in the Si-O-Mg bonds as magnesium content was increased to confirm results as shown in the deconvolution of the Mg XP spectra. This XPS analysis gives us an insight into the growth mode of the magnesium oxide, as we are unable to prove this using diffraction or microscopy. The binding energy shifts would suggest that at low loadings the magnesium is largely incorporated into the framework of the silica, at the pore-wall interface which is then able to act as nucleation sites for the growth of MgO crystallites with increasing magnesium content [150].

The same analysis was performed for all synthesized catalysts as polystyrene beads were added to introduce macroporosity. A graph of bulk to surface weight ratios determined from the ICP and XPS analysis as shown in Figure 4.14 (VI) for MgO/MM-(TLCT) SBA-15. From this graph, it is evident that an increase in the magnesium content causes an increase in the bulk weight percent measured by the ICP and also causes an increase in the surface weight percentages measured by the XPS. The lowest nominal loading of 0.25 g of the $MgNO_3$ yielded about 1.46 wt.% of Mg in bulk concentration and yielded about 0.20 wt.% on the surface. The highest loading of 1.50 g of $MgNO_3$ yielded about 8.60 wt.% of magnesium in bulk and that shown a yield of 2.6 wt.% on the surface. It is important to note that MgO in mesomacropores of the SBA-15 yielded a higher amount of MgO on the surface (about 2.60 wt.%) as compared to the MgO in the mesopores SBA-

15 (2.20 wt.%). This can be associated with the theory that there are several pore channels when macroporosity is introduced in the framework. Figure 4.15(VII) shows the relationship between Mg-O-Mg bonds and Mg-O-Si spectra as we increase magnesium content normalized to the nearest percentage. This shows the effect of increasing magnesium content on the silica - nanoparticle framework bond (Si-O-Mg bond). It is also obvious that an increase in the magnesium content causes an increase in the Mg-O-Mg bond whilst causing a decrease in the Mg-O-Si bond. This can be related to the fact that an increase in the magnesium content causes the formation of more Mg-O-Mg bonds and more individual metal nanoparticles rather than the Mg-O-Si bond. This is also evident in Figure 4.15(VIII) where an increase in the magnesium content caused an increase in Si-O-Mg bond. Figure 4. 16(IX) represents the Mg 2p XPS spectra indicating deconvoluted Mg-O-Mg and Mg-O-Si species for mesoporous SBA-15. Figure 4. 16(X) represents the Si 2p XPS stack spectra indicating deconvoluted Si-O-Mg and Si-O-Si species for mesoporous SBA-15.

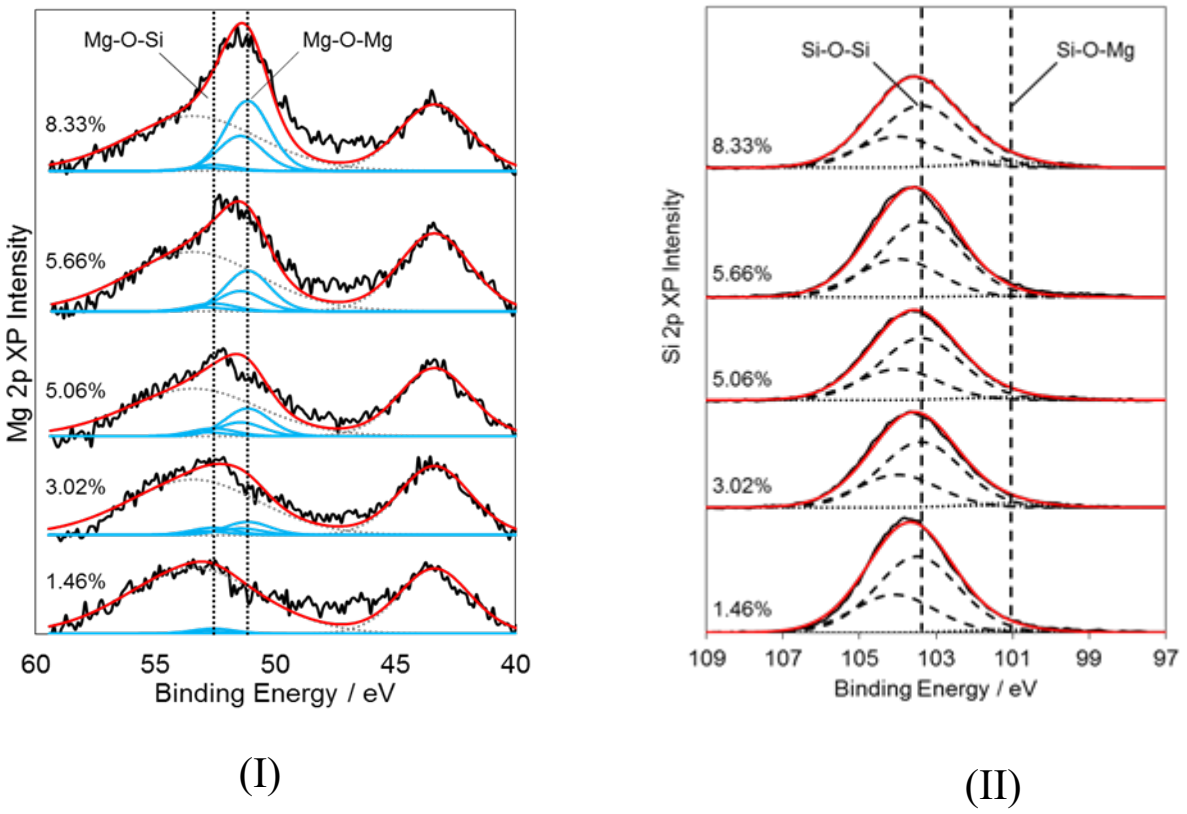

Figure 4.12: XPS analysis spectrum showing: (I) Mg 2p XPS spectra indicating deconvoluted Mg-O-Mg and Mg-O-Si species for MgO/(TLCT) SBA-15, (II) Si 2p XPS spectra indicating deconvoluted Mg-O-Mg and Mg-O-Si species for MgO/(TLCT) SBA-15

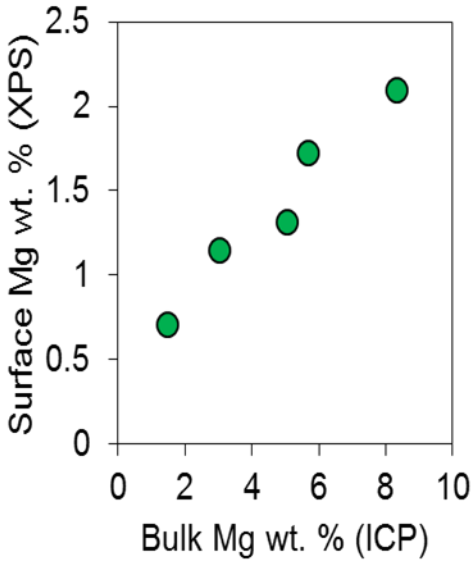

(III)

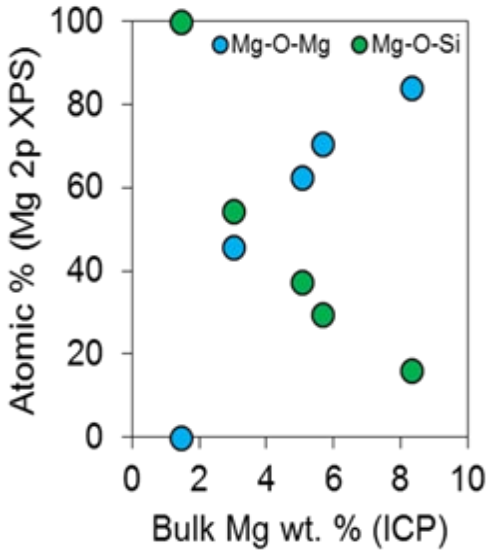

(IV)

Figure 4.13: XPS analysis spectrum showing: (III) Mg surface to bulk ratios determined by ICP and XPS for MgO/(TLCT) SBA-15 (IV) Mg-O-Mg and Mg-O-Mg species quantities, determined via Mg 2p XP spectra deconvolution for MgO/(TLCT) SBA-15

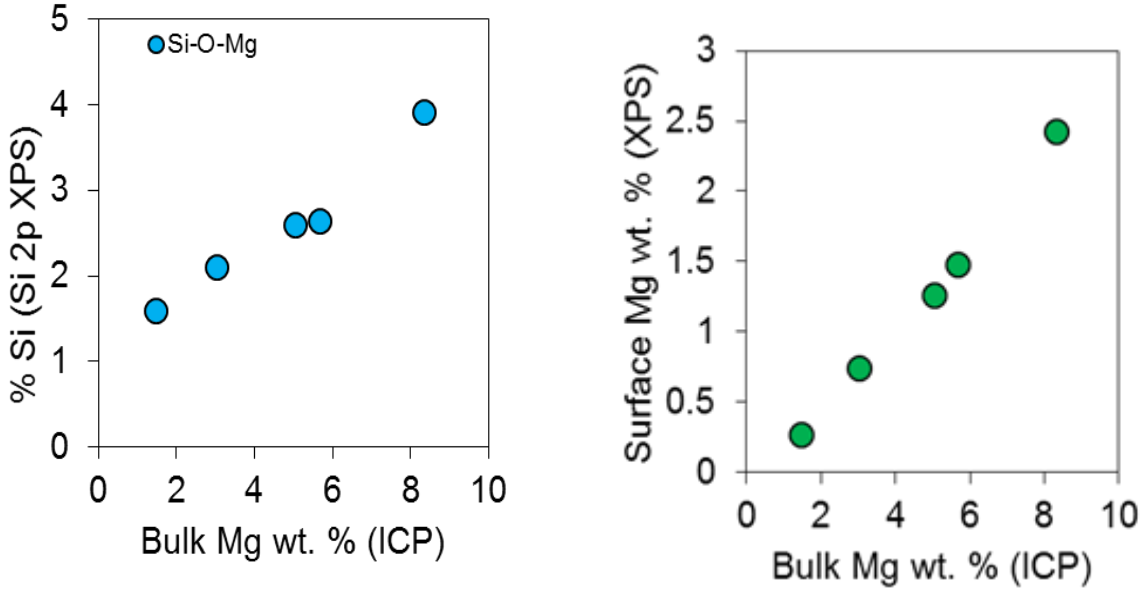

(V) (VI)

Figure 4.14: XPS analysis spectrum showing: (V) Si-O-Mg species quantities determined via Si 2p XP spectra deconvolution for MgO/(TLCT) SBA-15 (VI) Mg surface to bulk ratios determined by ICP and XPS for MgO/MM-(TLCT) SBA-15

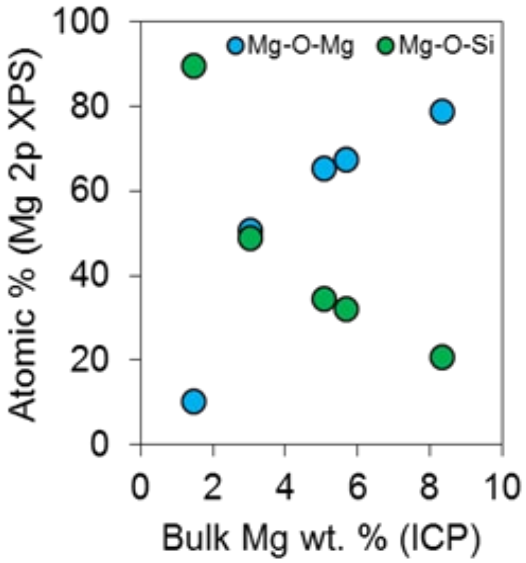

(VII)

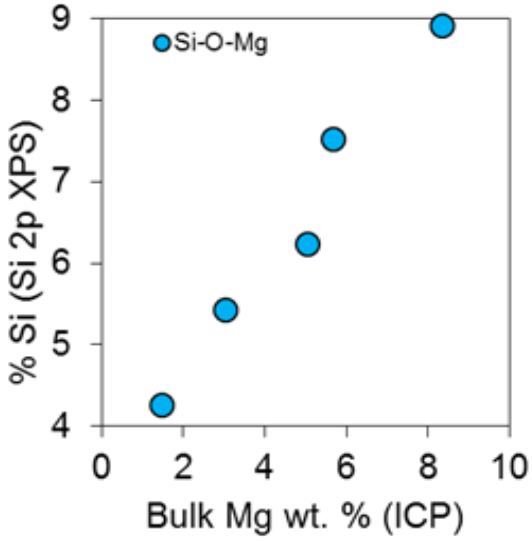

(VIII)

Figure 4.15: XPS analysis spectrum showing: (VII) Mg-O-Mg and Mg-O-Mg species quantities, determined via Mg 2p XP spectra deconvolution for mesoporous SBA-15 for MgO/MM-(TLCT) SBA-15 (VIII) Si-O-Mg species quantities determined via Si 2p XP spectra deconvolution for MgO/MM-(TLCT) SBA-15

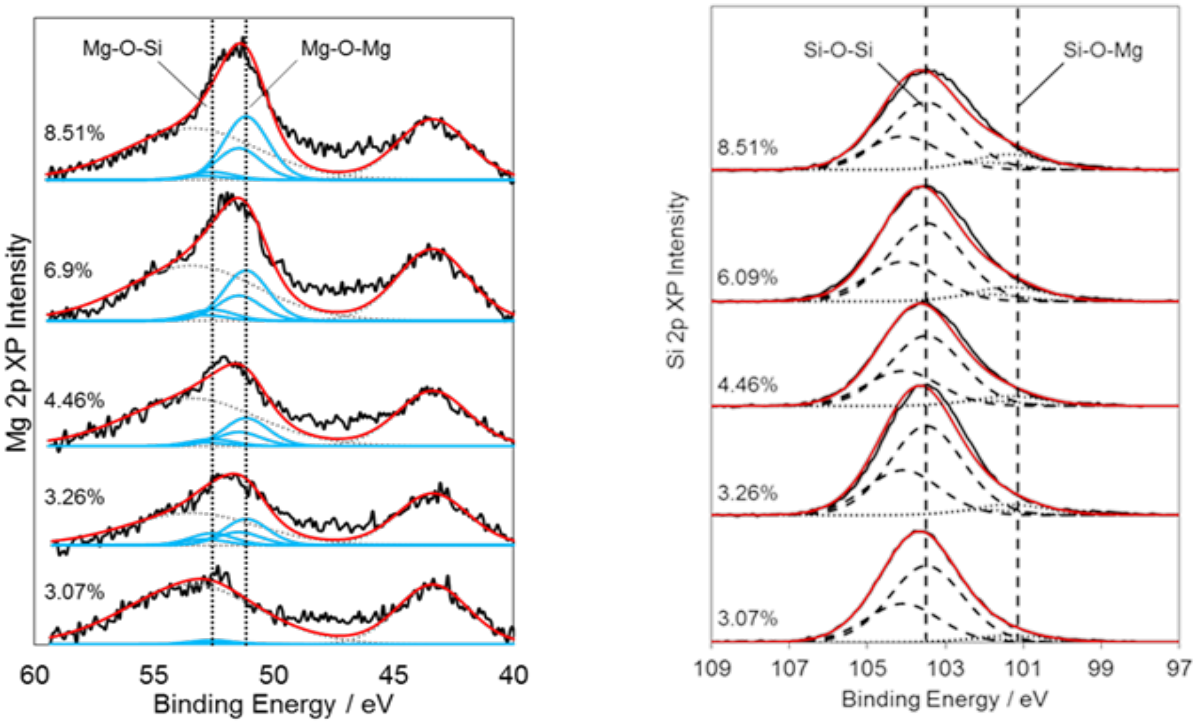

(IX) (X)

Figure 4. 16: XPS analysis spectrum showing: (IX) Mg 2p XPS spectra indicating deconvoluted Mg-O-Mg and Mg-O-Si species for MgO/MM-(TLCT) SBA-15 (X) Si 2p XPS spectra indicating deconvoluted Mg-O-Mg and Mg-O-Si species for MgO for MgO/MM-(TLCT) SBA-15

4.1.5 Fourier Transform Spectroscopy

Figure 4. 17 shows the FTIR spectra with all functional groups present in the MgO/(TLCT) SBA-15, CaO/(TLCT) SBA-15 respectively whiles Figure 4.18 shows all the functional groups present in MgO/ MM (TLCT)-SBA-15 and CaO/ MM (TLCT)-SBA-15 respectively. Unfunctionalized (TLCT) SBA-15 and MM-(TLCT) SBA-15 were also tested as a reference to respective functionalized ones. All synthesized catalysts stated above had the same presence of peaks as that of unfunctionalized (TLCT) SBA-15 and MM-(TLCT) SBA-15. For all the catalysts, there was

the absence of O-H stretching vibration usually observed within the range of 3000-4000 cm^{-1}. This showed that all chemisorbed water has been removed in the course of synthesizing these materials [151]. FTIR analysis for both mesoporous (TLCT) SBA-15 and hierarchical MM-(TLCT) SBA-15 shown in Figure 4. 17 - Figure 4.18(I - IV) display four distinct peaks present in all synthesized materials as magnesium and calcium content is increased. These peaks are found at wave numbers approximately of; 783 cm^{-1}, 1020 cm^{-1}, 1640 cm^{-1} and 2160 cm^{-1}. Peaks present at 783 cm^{-1} and 1020 cm^{-1} approximately can be attributed to the asymmetric and symmetric stretching nodes of Si-O-Si lattice vibrations [145][152]. There is, however, a slight decrease in this peak as magnesium content is increased. This can be best explained as an interaction between silicon and magnesium/calcium as magnesium/calcium content is increased. The peak at 1650 cm^{-1} can be associated with silanol groups [145]. The transmission band formed at approximately 2160 cm^{-1} could be attributed with the bending mode of OH groups of physically adsorbed water [145].

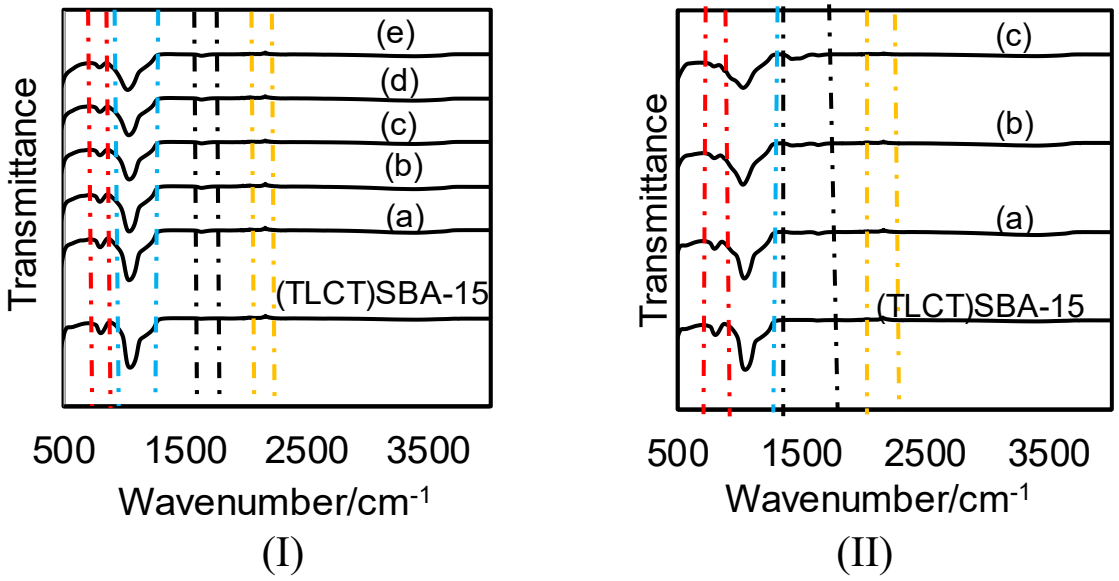

Figure 4. 17: FTIR spectra of (I): MgO/(TLCT) SBA-15 materials (a-e): 1.45 wt.%, 3.03 wt.%, 5.05 wt.%, 5.66 wt.%, 8.33 wt.% MgO/(TLCT) SBA-15 (II): CaO/(TLCT) SBA-15 diffractograms (a-c): 3.59 wt.%, 11.03 wt.%, 18.62wt.% CaO in mesopores of SBA-15

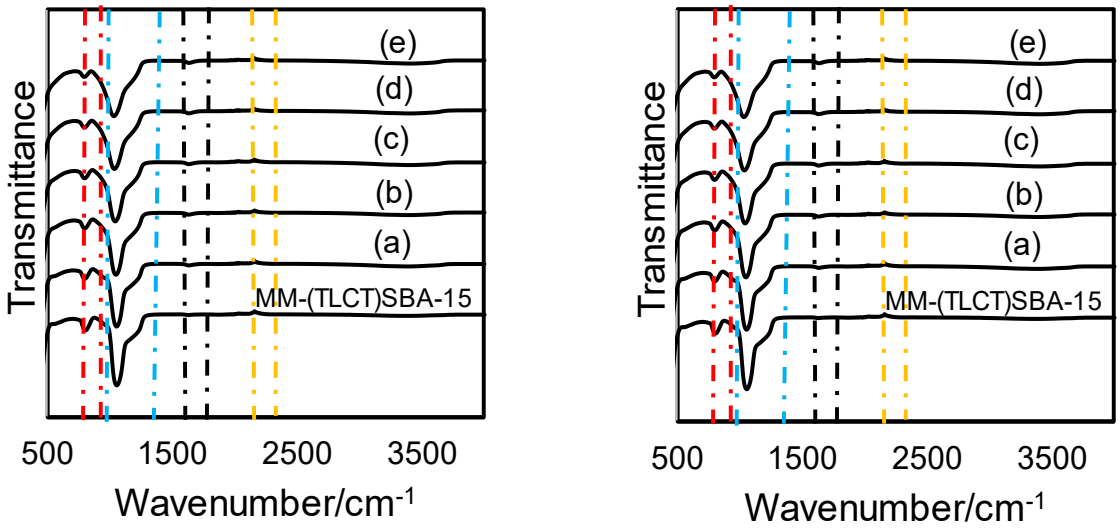

Figure 4.18: FTIR spectra of (III) MgO/ MM (TLCT)-SBA-15 (a-e): 3.07 wt.%, 3.26 wt.%, 4.46 wt.%, 6.90 wt.%, 1.8.51 wt.% MgO in mesomacropores of SBA-15 (IV) CaO/ MM (TLCT)-SBA-15 (a-c): 3.39 wt.%, 10.59 wt.%, 15.78 wt.% CaO in the mesomacropores of SBA-15

4.1.6 Thermogravimetric analysis -Mass spectroscopy (TGA-MS)

TGA-MS was performed to determine the thermal stability of all synthesized materials. As shown in Figure 4. 19, all synthesised samples exhibit a huge mass loss in the region between 50 ºC to 100 ºC. This is due to the elimination of physisorbed water or water of crystallization (dehydration). In Figure 4. 19 (I) for MgO/(TLCT) SBA-15, there is a slight mass drop at about 300 ºC which can be attributed to the removal of carbonate species from the surface. This is evident as no similar mass drop at comparable temperatures alluding to no desorption of gases in all samples. It is evident from Figure 4. 19 (II) representing the desorption of gases associated with CaO/(TLCT) SBA-15. Two distinct peaks are observed from 50 ºC to 500 ºC and the other from 540 ºC-680 ºC for 3.59 wt.% and 11.03 wt.% of CaO in the mesopores of SBA-15. Peaks formed

at 50 ºC to 500 ºC can be attributed to the loss of carbonate species on the surface of the materials. It is obvious that more carbonate species was expelled from 11.03 wt.% as compared to 3.59 wt.%. Peaks formed from 540 ºC-680 ºC can be associated with calcium carbonate formed from the adsorption of atmospheric carbon dioxide. For 18.62 wt.% CaO in the mesopores of SBA-15, three distinct peaks are observed over the temperature range. Bidentate peaks are formed within the range of 50 ºC-500 ºC which can be attributed with the removal of carbon monoxide and carbon dioxide forming a bidentate carbon species from the surface of the material. Peaks formed from 540ºC-680ºC can be associated with calcium carbonate formed from the adsorption of atmospheric carbon dioxide [153].

Further corroboration of the composition of MgO/ MM (TLCT)-SBA-15 (Figure 4. 20, III) and CaO/MM (TLCT)-SBA-15 (Figure 4. 20, IV) was found using the TGA-MS. As shown, all synthesized materials show one peak weight loss from 40 ºC-100 ºC signifying the loss of physisorbed water and or water of crystallization. In the case of MgO/MM (TLCT)-SBA-15, a further mass loss was recorded from 100 ºC to 200 ºC as magnesium content increases. This could be attributed to the further removal of water. CaO/MM (TLCT)-SBA-15 also exhibit a huge mass loss from 105 ºC to 487 ºC. This can be ascribed to the removal of surface carbonate and hydroxide groups from the material [153]. It is evident that this peak increase as calcium content is increased thereby creating more carbonates to be evolved from the surface. A similar mass loss initiated around 580 ºC to 800 ºC may be due to the presence of calcium carbonates formed from the adsorption of atmospheric carbon dioxide.

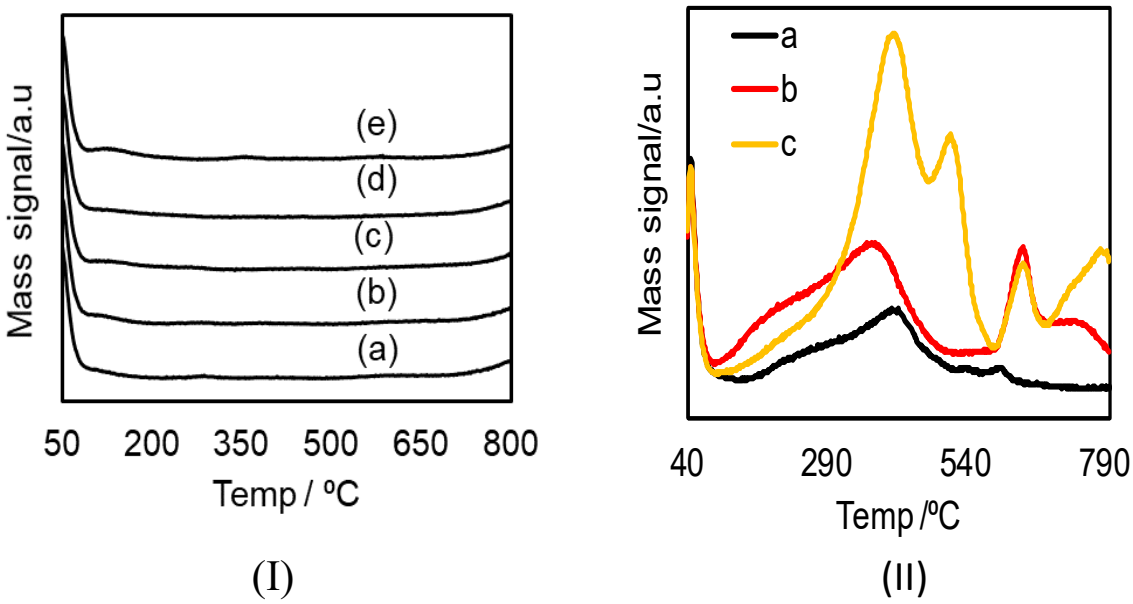

Figure 4. 19: TGA MS profiles of (I): MgO/(TLCT) SBA-15 showing desorption of gases (a-e): 1.45 wt.%, 3.03 wt.%, 5.05 wt.%, 5.66 wt.%, 8.33 wt.% of MgO in the mesopores of SBA-15 (II): CaO/(TLCT) SBA-15 showing desorption of various gasses at different temperatures (a-c): 3.59 wt.%, 11.03 wt.%, 18.62 wt.% CaO in the mesopores of SBA-15

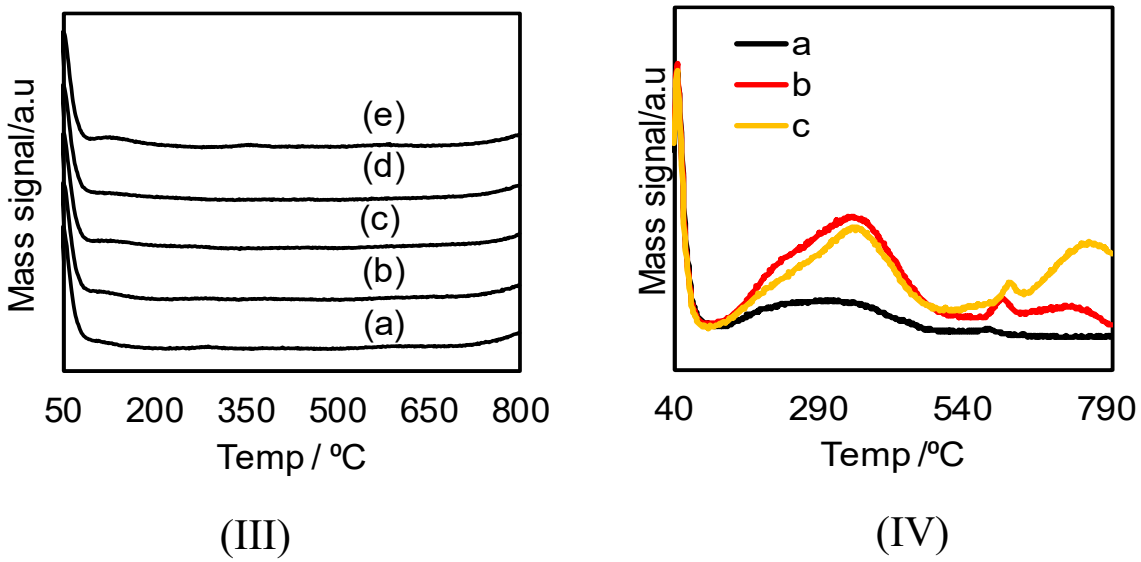

Figure 4. 20: TGA MS profiles of; (III) MgO/ MM (TLCT)-SBA-15 (a-e): 3.07 wt.%, 3.26 wt.%, 4.46 wt.%, 6.90 wt.%, 1.8.51 wt.% MgO in mesomacropores of SBA-15, (IV): CaO/ MM (TLCT)-SBA-15 (a-c): 3.39 wt.%, 10.59 wt.%, 15.78 wt.% CaO in the mesomacropores of SBA-15

4.1.7 Scanning Electron Microscope (SEM)

SEM experiments were conducted to show the surface morphology. Figure 4. 21(a) is a SEM image of 1.45 wt.% of MgO/(TLCT) SBA-15 whereas Figure 4. 21(b) shows SEM image of 8.33 wt.% of MgO/(TLCT) SBA-15. Figure 4. 22(c) is SEM image of 3.59 wt.% CaO/(TLCT) SBA-15 and Figure 4. 22 (d) shows SEM image of 18.62 wt.% CaO/(TLCT) SBA-15. Figure 4. 23(e) is a SEM image of the lowest loading (1.45 wt.%) of MgO/ MM (TLCT)-SBA-15 and Figure 4. 23(f) shows the SEM image of highest loading (8.33 wt.%) of MgO/ MM (TLCT)-SBA-15. Figure 4. 24 (g & h) represent the lowest loading (3.39 wt.%) and highest loading (15.78 wt.%) of CaO in mesomacroporous SBA-15 respectively. All SEM images were taken under different magnification and are not recommended for comparative purposes. All MgO/(TLCT) SBA-15

synthesized materials have a fibrous structure, which is an agglomerate of long fibers that are constituted from a small rod-like sub-particles [154].

Figure 4. 21 (a) shows dispersed particles on the surface due to less incorporation of MgO species. There was more agglomeration of particles found in Figure 4. 21(b) due to the high incorporation of MgO species. As can be observed, CaO/TLCT SBA-15 materials from Figure 4. 22 (c) and (d) exhibit aggregating of the regular rod-shaped particle [155] as commonly observed in pure SBA-15 silica [155]. The CaO/TLCT SBA-15 catalyst was solid with wheat like structure, a different aggregation pattern of rod-shaped. Figure 4. 21(b) have particles, which are smaller and irregular due to the higher incorporation of calcium. Macroporous materials from Figure 4. 23 - Figure 4. 24 show mesopores evenly dispersed with macropores packed and interconnected to each other with windows opening from one macropore into another neighboring macropore. Figure 4. 23(e) show loosely packed macropores with Figure 4. 23(f) on the other hand, showing densely packed macropore. This is because of higher loading of MgO forming more agglomeration of particles than the lower loading. In viewing the surface morphologies of the synthesized CaO/ MM (TLCT)-SBA-15 materials, all synthesized materials show the formation of macropore template with the presence of mesopores within them. Figure 4. 24 however shows a level of cloudiness due to higher amounts of calcium on the surface of the material. These findings prove results obtained from XRD, porosimetry for the successful synthesis of these materials.

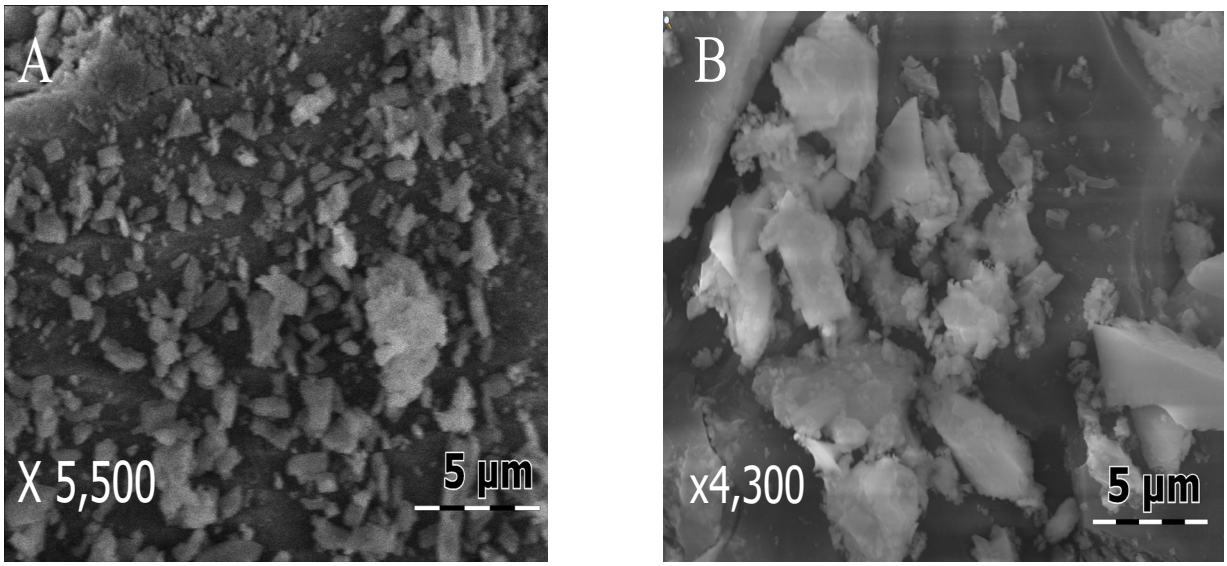

Figure 4. 21: SEM images of; (A) 1.45 wt.% MgO/TLCT SBA-15 (*magnification x5,500*) and (B) 8.33 wt.% MgO/TLCT SBA-15 (*magnification x4,300*)

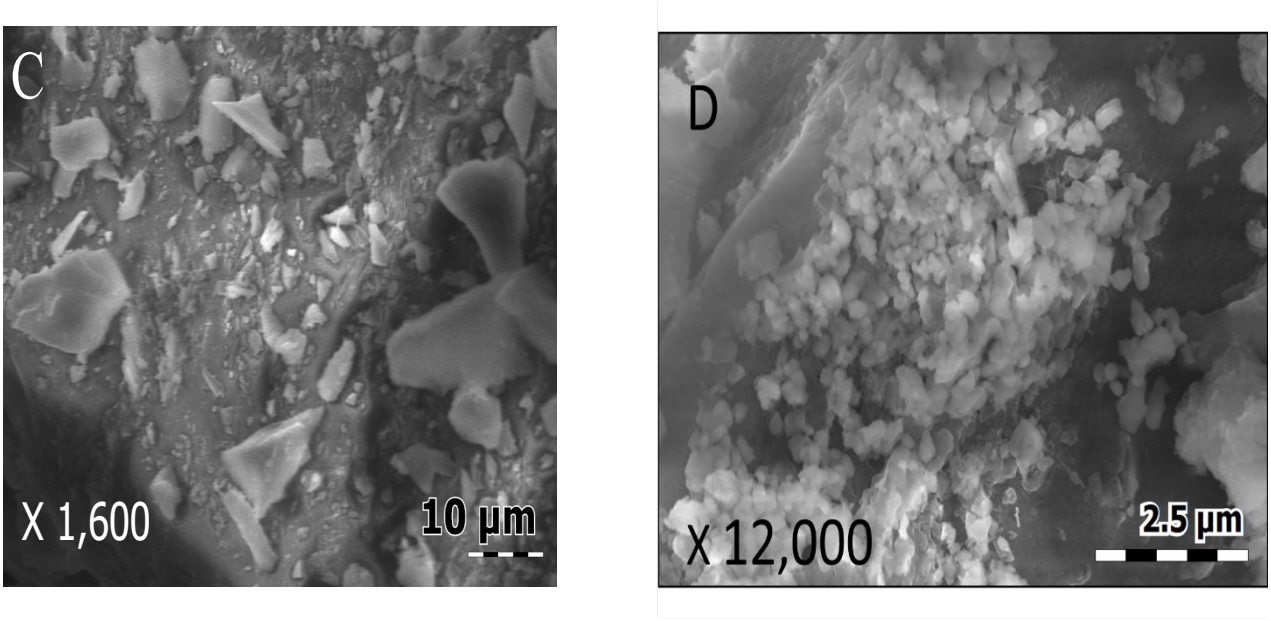

Figure 4. 22: SEM images of (C) 3.59 wt.% CaO/TLCT SBA-15 (*magnification x1,600*) and (D) 18.62 wt.% CaO/TLCT SBA-15 (*magnification x12,000*)

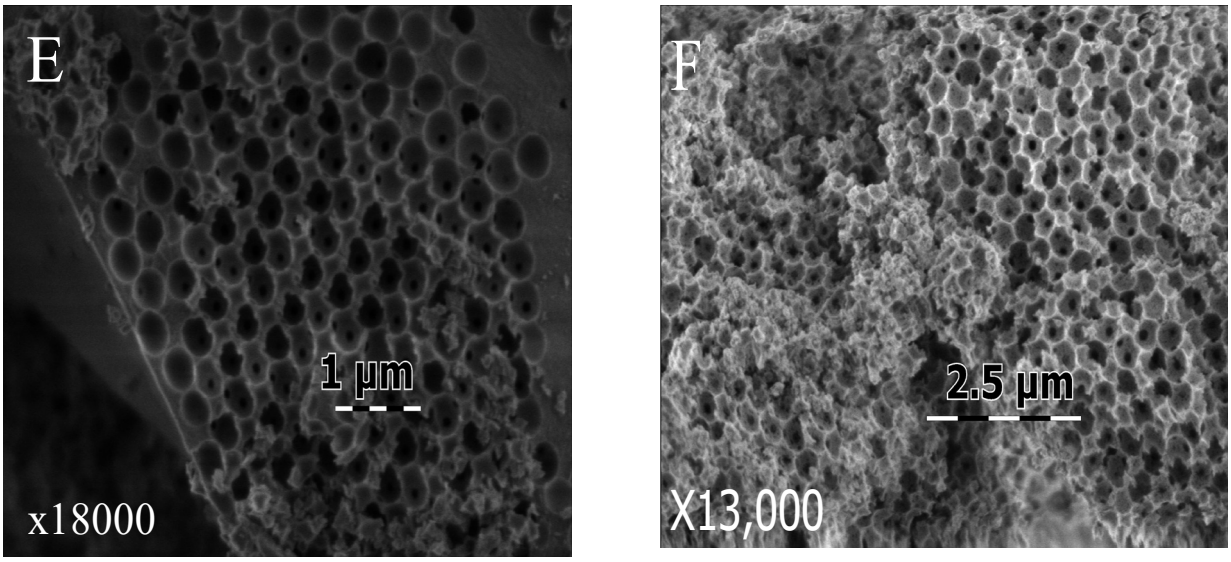

Figure 4. 23: SEM images of (E) 1.45 wt.% MgO/ MM (TLCT)-SBA-15 (*magnification x18,000*) and (F) 8.33 wt.% MgO/ MM (TLCT)-SBA-15(magnification x13,000)

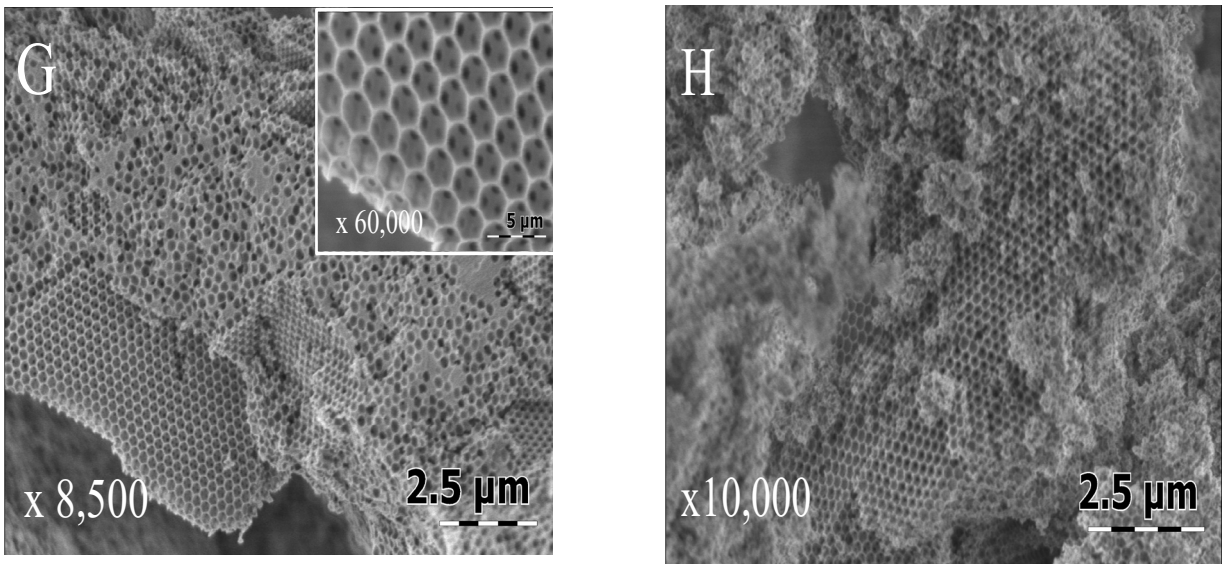

Figure 4. 24: SEM images of (G) 3.39 wt.% CaO/ MM (TLCT)-SBA-15 (*magnification x8,500*) and (H) 10.58 wt.% CaO/ MM (TLCT)-SBA-15 (*magnification x10,000)*

4.1.8 Scanning Transmission Electron Microscope (STEM)

Further structural characterization with TEM again substantiates the differences in overall morphology determined by SEM analysis. All images were taken at different magnification to obtain a much clearer image of the structural morphology therefore cannot be used for comparison purposes. Figure 4. 25(a) show the TEM image of 1.45 wt.% of MgO/(TLCT) SBA-15, Figure 4. 25(b) shows 8.33 wt.% of MgO/TLCT SBA-15. Figure 4. 26(c) is a TEM image of the lowest loading (1.45 wt.%) of MgO in the mesomacropores of SBA-15 whiles Figure 4. 26 (d) shows the highest loading (8.33 wt.%) of MgO in the mesomacropores of SBA-15, Figure 4. 27 (e) represents 3.39 wt.% of CaO in mesomacropores of SBA-15) and Figure 4. 27(f) represents the highest loading (15.78 wt.%) of CaO in the mesomacropores of SBA-15 All synthesized materials as shown in Figure 4. 25 exhibit the morphology of 2D hexagonal array of nanochannels with uniform pore size along the (110) direction [155] which is similar to the structure of a typical SBA-15 material supported by literature [156]. Although high amounts of MgO was functionalised on the SBA-15, it did not affect the morphology of the SBA-15, which is in good agreement with XRD and porosimetry results. Also, no aggregates of MgO nanoparticles was observed which shows that it has been highly distributed inside the channels of SBA-15. TEM was used to determine the long-range ordering channels evident in mesoporous materials. All macroporous synthesized materials show a conclusive evidence of ordered macrostructured silicate visibility of hexagonal ordering. SEM Image of Figure 4. 25 show a clumsy structure due to higher loading of MgO in the mesomacropores of SBA-15. Figure 4. 26 and Figure 4. 27 shows how macropore framework silica is formed of highly concentric mesoporous channels resulting from self-assembly of the block copolymer solution around polystyrene beads. The high curvature of the mesopore channels in the macropores could suggest a strong electrostatic and hydrogen bonding between polystyrene

beads, the block copolymer, and silica precursor. The curvature could arise from the strain on the block copolymer walls in the liquid crystal in conforming to the PS beads. This may result in a slightly contracted mesoporous channel in the hierarchical material [157]. TEM images confirm the XRD results obtained which shows an intense crystalline phase reflection peak (section 4.2.1).

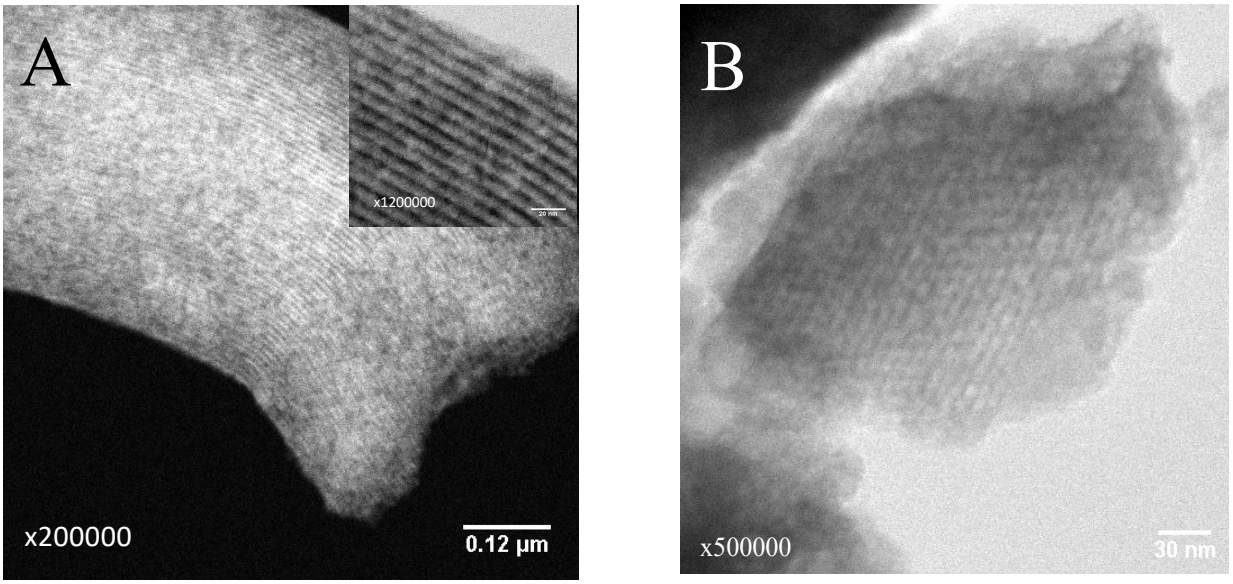

Figure 4. 25: TEM images recorded for (A) 1.45 wt.% MgO/(TLCT) SBA-15 (*magnification x200,000*) (B) 8.33 wt.% MgO/(TLCT) SBA-15 (*magnification x500,000*)

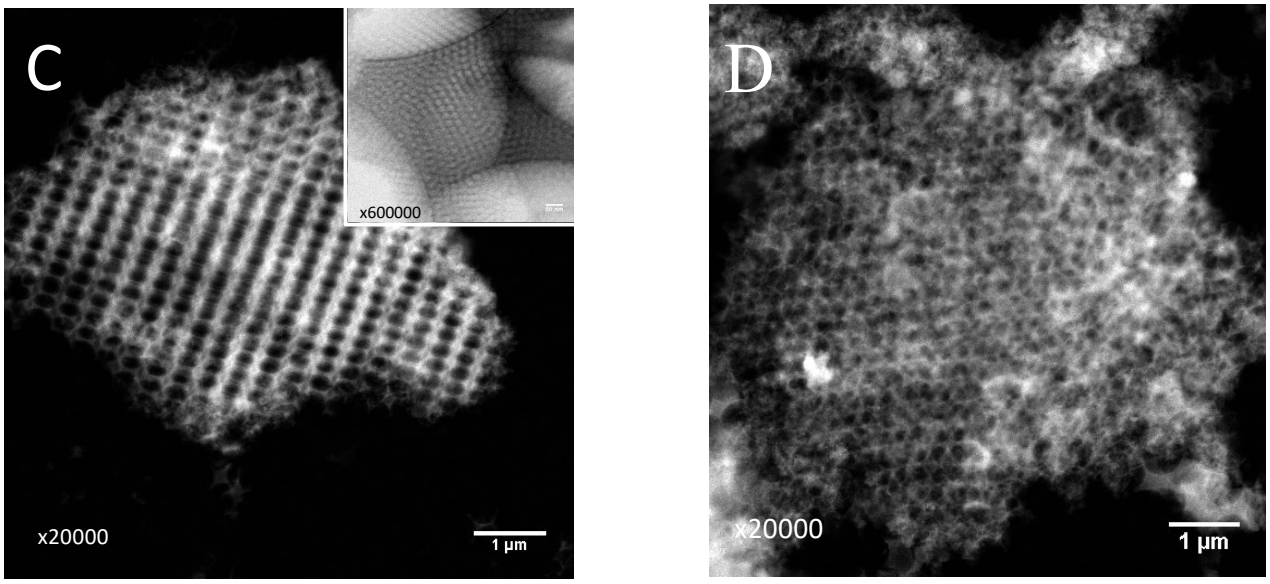

Figure 4. 26: TEM images recorded for (C) 1.45wt.% MgO/ MM (TLCT)-SBA-15 (*magnification x20,000*) (D) 8.33wt.% MgO/ MM (TLCT)-SBA-15 (*magnification x20,000*)

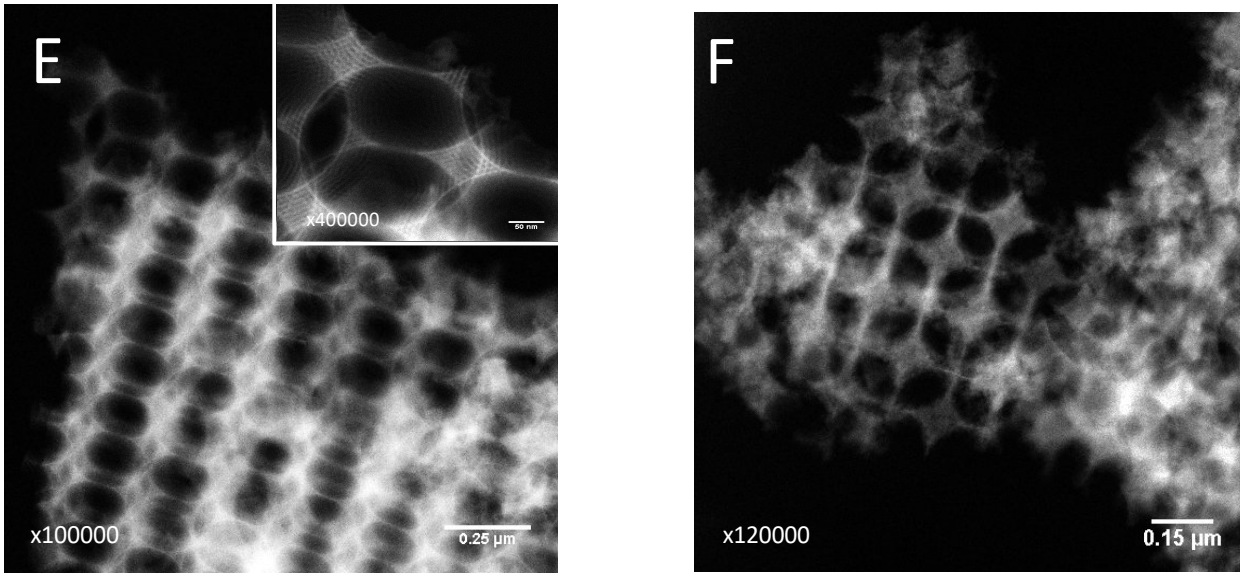

Figure 4. 27: TEM images recorded for (E) 3.39wt.% CaO/ MM (TLCT)-SBA-15 (*magnification x100, 000*) and (F) 15.78wt.% CaO/ MM (TLCT)-SBA-15 (*magnification x120,000*)

4.1.9 Energy Dispersive X-Ray analysis (EDX)

Energy Dispersive X-ray spectra were taken from the SEM equipment to provide further details on chemical characterization of bulk and surface of individual nanoparticles. From Figure 4. 28(a), magnesium atoms are shown as green dots present inside the channels of SBA-15. Figure 4. 28(b) showed magnesium as green dots, silicon as a red interface with oxygen atoms as blue dots. It is evident that Mg, Si, O atoms are homogenously dispersed on the surface of the composites as clearly shown in the SEM-EDX mapping images from Figure 4. 28(b) which clearly coincides with XRD results. From EDX data analysis as shown in Figure 4. 28 (c), it is clear that more Ca species as shown as green dots are homogenously spread in the SBA-15 channels. However, it is important to note that Ca is the only element detected except the SBA-15 framework elements which are Si and O. These results are in alignment with XRD and ICP OES data which shows minute amounts of impregnated species.

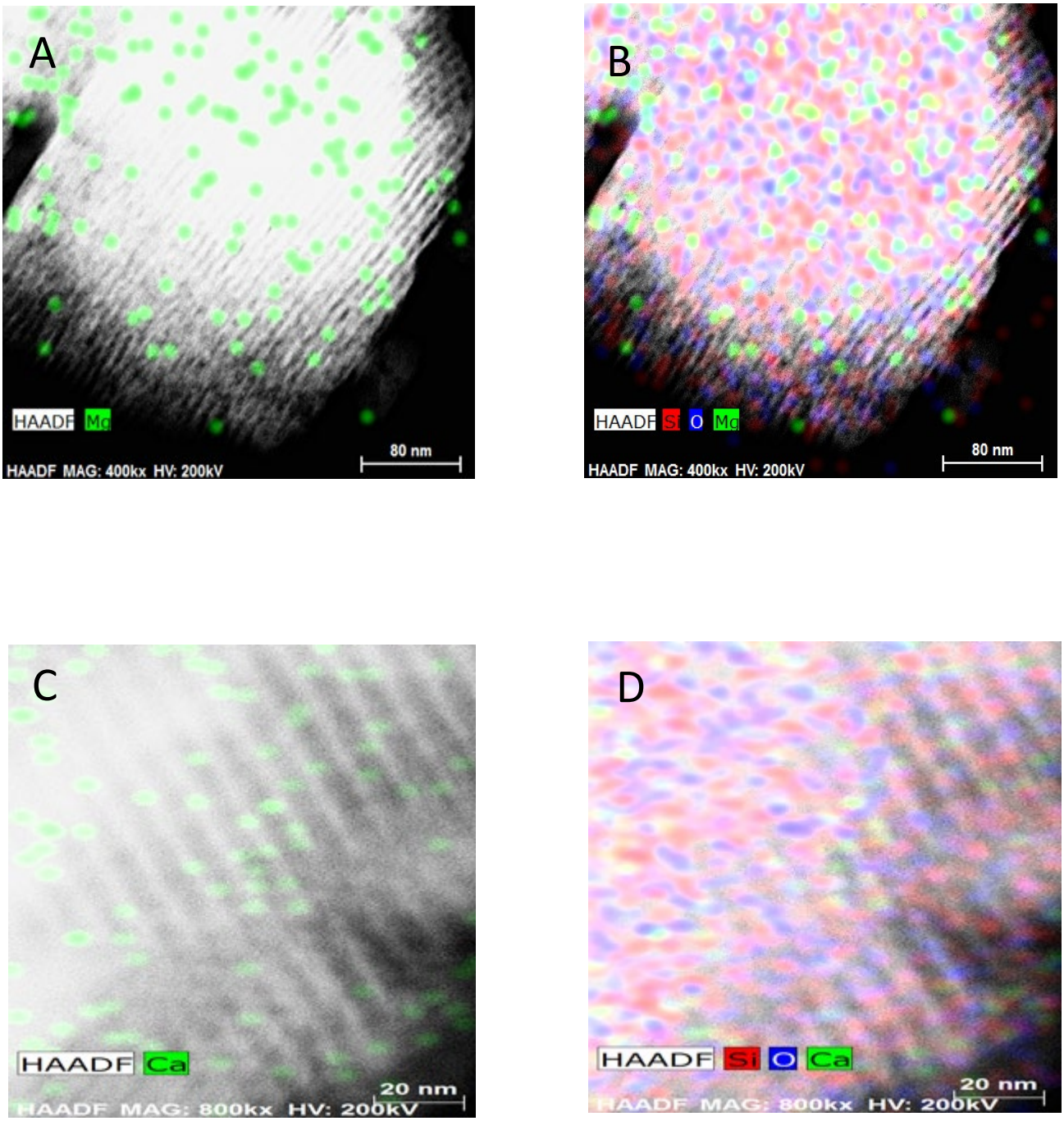

Figure 4. 28: EDX images (a and b) showing the presence of MgO in mesopores of SBA-15 (c and d) showing the presence of CaO in mesopores of SBA-15

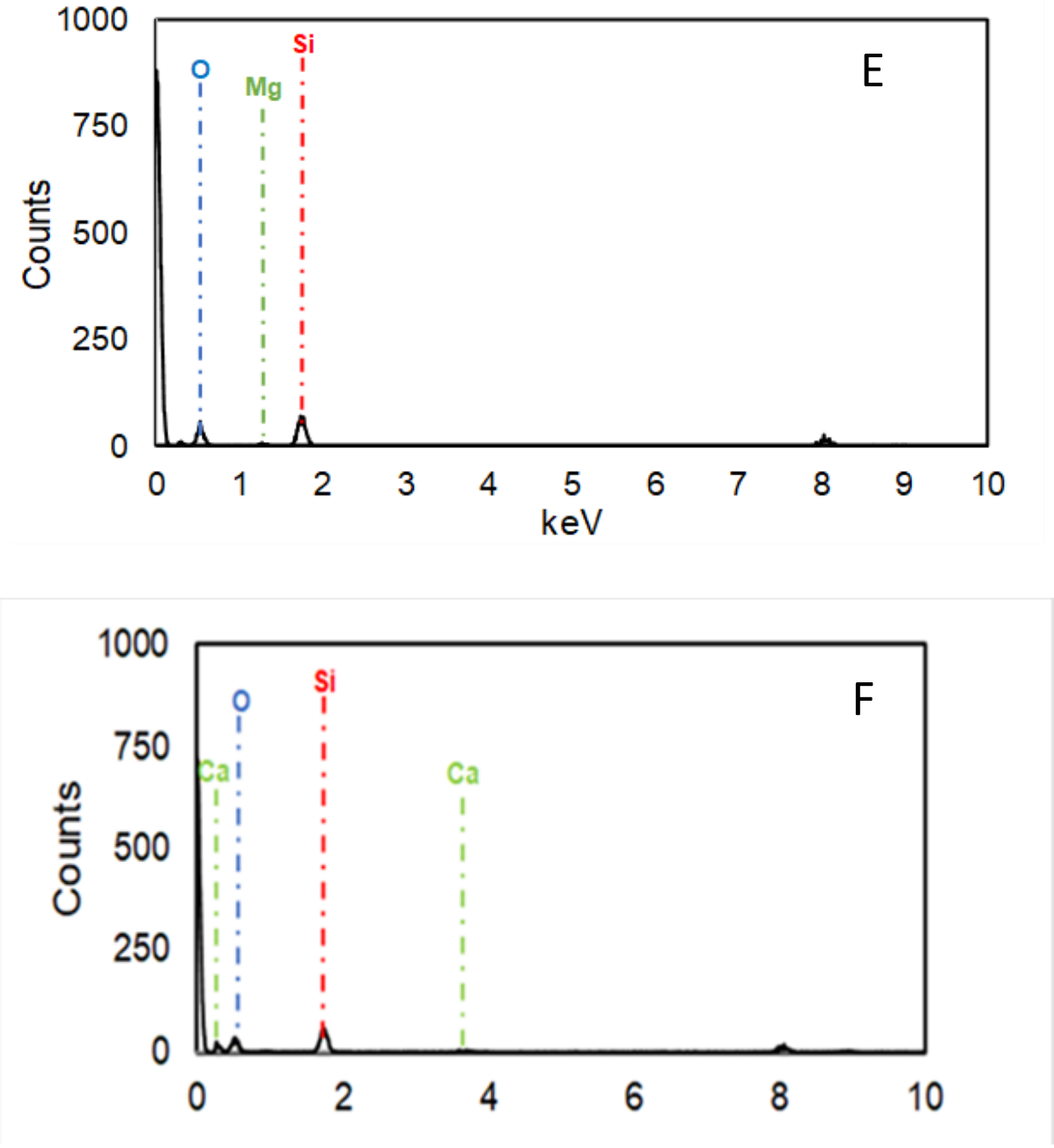

Figure 4. 29: EDX images (e) showing the corresponding EDX spectrum of MgO/(TLCT) SBA-15 with 1.45 wt.% MgO loading (f) showing the corresponding EDX spectrum of CaO/(TLCT) SBA-15 with 3.59 wt.% CaO loading

4.2 Performance/Yield of Catalysts Using Lower Triglycerides– Tributyrin Transesterification Characterisation

The impact of tuning catalysts, surface termination and its basicity upon the resulting catalytic reactivity was subsequently assessed towards the transesterification of tributyrin. MgO/TLCT SBA-15, MgO/ MM-(TLCT) SBA-15, CaO/(TLCT) SBA-15 and CaO/ MM-(TLCT) SBA-15 catalysts were screened with tributyrin for transesterification reactions to produce methyl tributyrate as corresponding methyl esters of fatty acid. These are short-chain saturated triglyceride models that are typically used to produce commercial biodiesel from palm oil and are a useful reaction for evaluating solid basicity. Comparisons were drawn between MgO/TLCT SBA-15 and MgO/ MM-(TLCT) SBA-15 then CaO/(TLCT) SBA-15 and CaO/ MM-(TLCT) SBA-15.

4.2.1 Tributyrin Transesterification: MgO/(TLCT) SBA-15 and MgO/MM-(TLCT) SBA-15

Transesterification of tributyrin is a three-step reaction where three fatty acids are sequentially cleaved from the triglyceride compound resulting in the formation of fatty acid methyl esters and glycerol [155]. Transesterification reactions were performed at 60 ^{o}C to determine the efficiency of these novel catalysts.

Tributyrin conversion for MgO/(TLCT) SBA-15 catalysts were first tested for transesterification as shown in Figure 4. 30(I). It was observed the highest magnesium weight content (8.33 wt.% MgO/(TLCT) SBA-15) yielded a tributyrin conversion of about 40% after 24 h. The least percentage of magnesium content showed a conversion rate of about 10%. Initial rate was calculated from the reaction profile in mmol.h^{-1} as shown in Figure 4. 30 (II). There was an increase

in the initial rate as magnesium content was increased showing the initial rate of about 0.6 mmol/h at the highest loading of magnesium. The initial rate was normalized to one gram of magnesium based on the magnesium quantity present within the catalyst as shown in Figure 4. 30 (II). There was however a decrease in the initial rate when normalized per gram of magnesium as the magnesium content increased. This could be due to the formation of small and more dispersed particles within the catalyst at a lower magnesium content leading to the magnesium oxide nanoparticles available for catalysis rather than the bulk metal within the particle. These results confirm that these series of catalysts have successfully worked for transesterification reaction and performed better than catalysts prepared by in situ method discussed by Eugena *et al* [116]. The lower, middle and higher metal loadings of MgO/(TLCT) SBA-15 were screened for transesterification reaction using tributyrin at 90 ^{o}C to maximize the yield of fatty acid methyl esters (FAME) production. It was realized that the highest loading of catalyst yielded about 70% conversion. MgO/ MM-(TLCT) SBA-15 were screened for tributyrin conversion was performed at 90 ^{o}C as shown in Figure 4. 31 (III) and (IV). It was realized that when macropores were introduced into the mesopores of SBA-15, there is an increase in the tributyrin conversion as magnesium content increases. The highest loading of MgO/ MM-(TLCT) SBA-15 (8.51 wt. %) showed a much higher conversion of about 75%. This shows that incorporation of macropores into mesopore networks improves biofuel catalyst by enhancing bulky triglyceride diffusion.

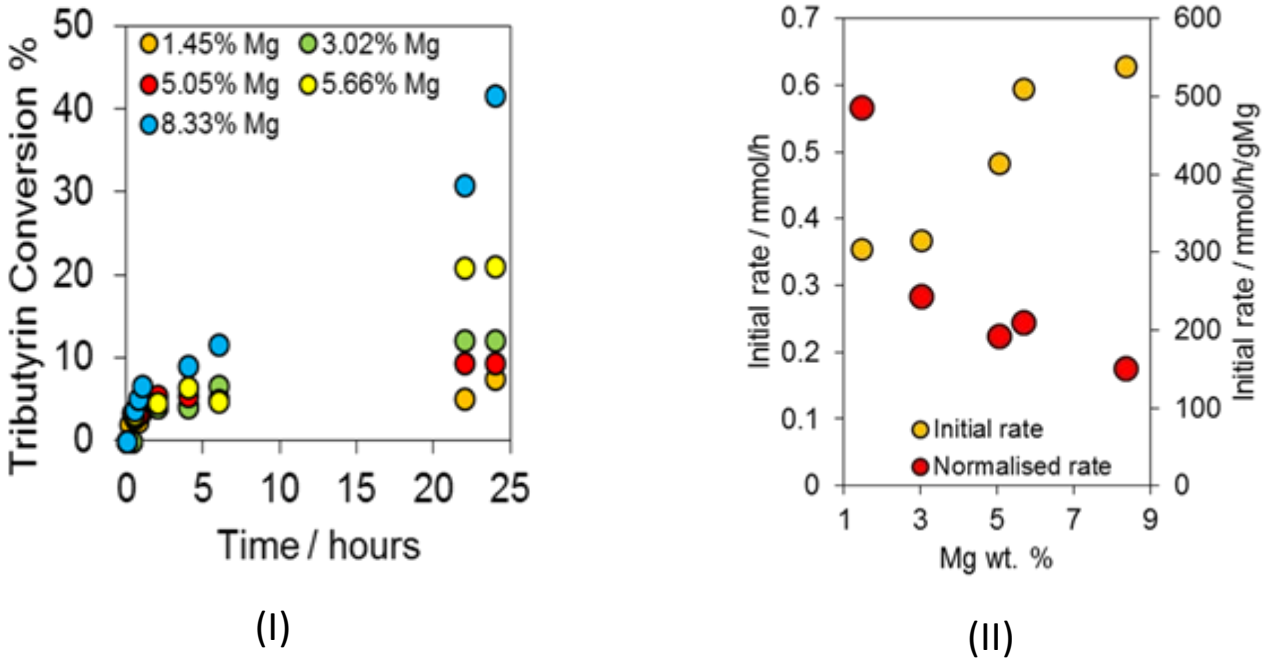

Figure 4. 30: (I) Tributyrin conversion of MgO/TLCT SBA-15, (II) Initial rate in mmol.h^{-1}, normalized rate per 1 g Mg as a function of magnesium content

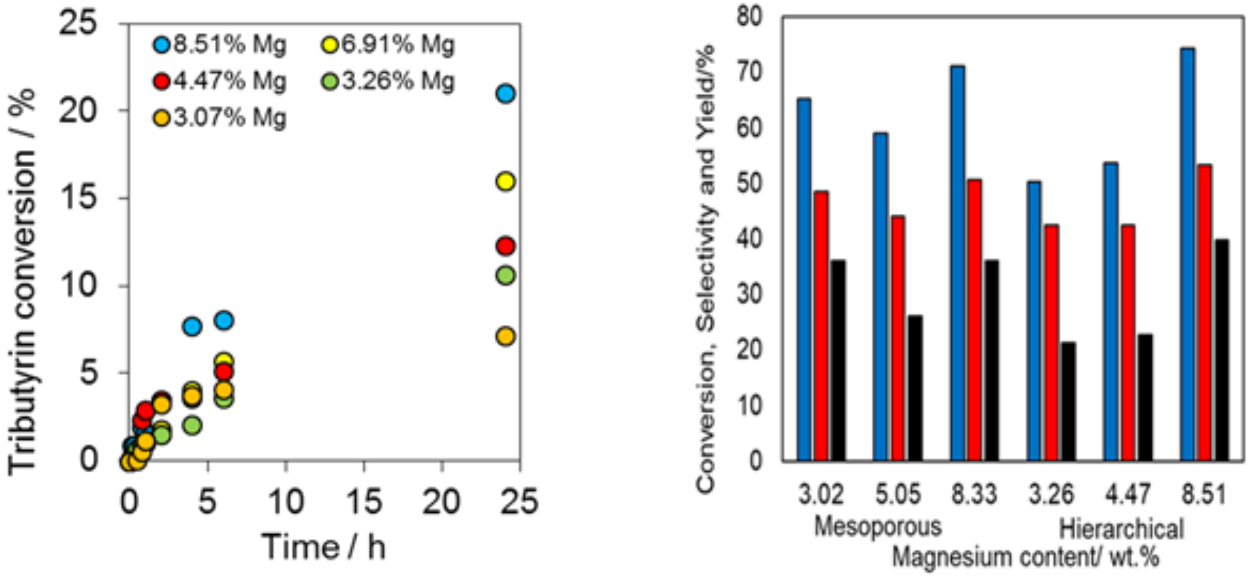

(III) (IV)

Figure 4. 31: (III) Tributyrin conversion of MgO/TLCT MM SBA-15, (IV) Tributyrin conversion, methyl butyrate selectivity and biodiesel yield of both MgO/TLCT SBA-15 and MgO/TLCT MM SBA-15 expressed as a percentage as a function of magnesium weight content

4.2.2 Tributyrin Transesterification: CaO/(TLCT) SBA-15 and CaO/MM-(TLCT) SBA-15

The efficiency of all synthesized CaO materials was also evaluated towards transesterification using tributyrin at 60 ºC. It is observed that CaO/(TLCT) SBA-15 outperformed better than CaO/MM (TLCT) SBA-15 as shown in Figure 4. 32. Higher loading of CaO/MM (TLCT) SBA-15 (15.78 wt.%) shows about 65% conversion as compared to the highest loading of CaO/(TLCT) SBA-15 (18.62 wt.%) which shows 82% conversion. The same trend is seen for the formation of methyl butyrate as seen in Figure 4. 32 (II) where mesoporous materials produce higher fatty acid methyl esters yield as compared to the hierarchical materials. For all materials, an increase in calcium species causes a decrease in initial reaction rate recorded within the first 1 h of the reaction.

From CaO/(TLCT) SBA-15 in Figure 4. 33 (III), the highest loading (18.62 wt.%) of the materials shows a dramatic decrease in initial reaction rate followed by the lowest loading (3.59 wt.%) then by the middle loading (11.03 wt.%). The same trend is evident in hierarchical materials in Figure 4. 33 (IV) where an increase in calcium species decreases the conversion rate. This can be associated with the formation of high calcium carbonate species that poisons the reaction thereby causing a slower reaction rate for especially the higher loading calcium species [158]. In Figure 4. 34(V), all mesoporous and hierarchical materials were tested for tributyrin conversion, selectivity and fatty acid methyl esters (FAME) yield at 90 ºC. At 90 ºC, all materials attained reaction completion after 24 h. as expected in a discussion by Albuquerque *et al* [119] although reaction conditions differ. Higher selectivity to FAME production was seen for lowest loading for both CaO/(TLCT) SBA-15 materials (3.59 wt.%) and CaO/MM-(TLCT) SBA-15 materials (3.39 wt.%). FAME yield increased as well for lowest loadings of mesoporous and hierarchical materials. Recalcined 3.59 wt.% and 18.62 wt.% CaO/(TLCT) SBA-15 at 800ºC were screened using the tributyrin reaction as well as shown in Figure 4. 34 (VI). The tributyrin conversion attained maximum at higher calcium weight percentage (18.62 wt.% CaO/(TLCT) SBA-15). From the graph shown below, after 1 h of reaction, there was no significant increase in initial rate for higher loading (18.62 wt.%) as compared to lowest loading (3.59 wt.%) after recalcination. WAXRD in Figure 4.1 (IX) showed a distortion in structure of the highest loading catalyst (18.62 wt.%). This may influence the initial rate of the tributyrin reaction. Comparing both magnesium and calcium series of catalysts, it is evident that the calcium series of catalyst performs better than the magnesium series of catalysts in total. All synthesized catalysts were further screened for higher triglycerides. It is very relevant to note that other than methyl butyrate, glycerol and the intermediate compound–dibutyrin and monobutyrin expected from the stepwise transesterification

of tributyrin, were seen in any of the gas chromatograph traces, including those recorded for samples taken after 24 h. This means that there are no alternative routes over the materials analysed and that selectivity to methyl ester is governed only by overall triglyceride conversion and that this should reach 100% completion when all the tributyrin and subsequent intermediated are reacted. Figure 4. 35 shows the initial rate of the reaction calculated from the reaction profile in $mmol.h^{-1}$. Initial rate was normalized to one gram of magnesium and calcium based on the magnesium and calcium quantity present within the catalyst. A comparison was made between magnesium and calcium to which performs better. From experimental analysis, calcium species have a faster rate of reaction as compared to magnesium. Lower weight percentages of Mg and Ca outperforms than higher weight percentages. This may be due to blockages of pores due to higher weight percentages. However, lower weight percentage of Ca (3.59 wt.%) proves to be a better catalyst with an initial rate of about 11 $mmol.h^{-1}g^{-1}$.

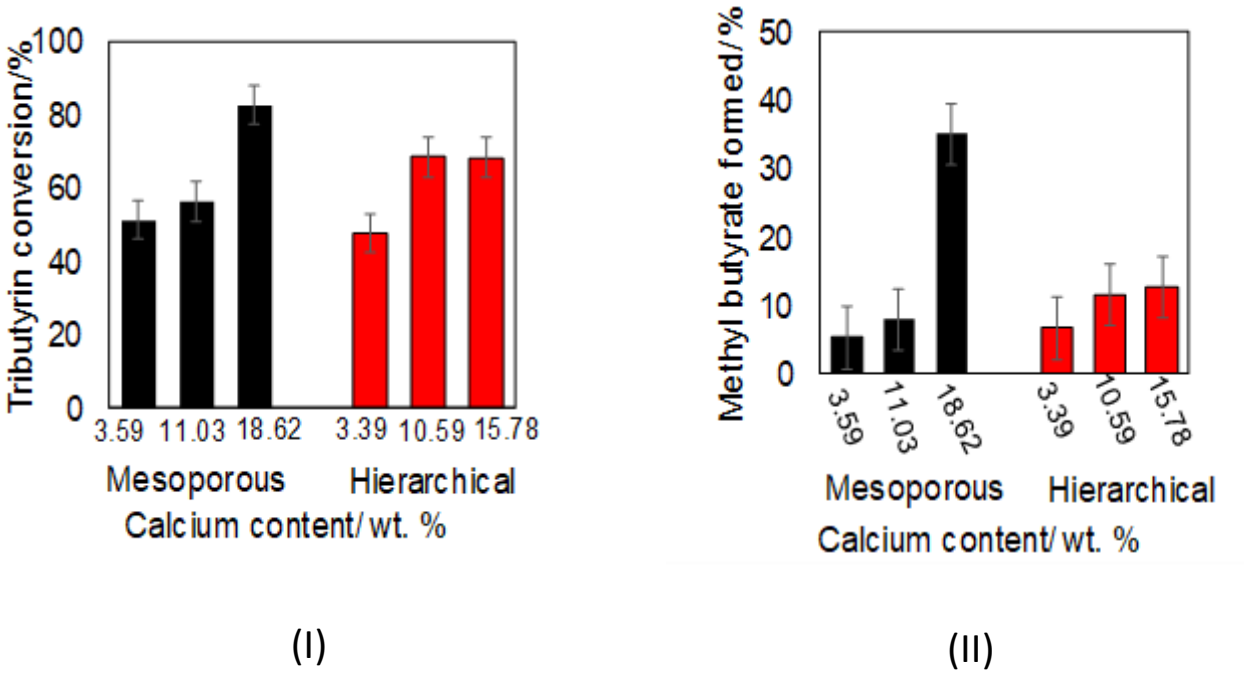

Figure 4. 32: (I) Tributyrin conversion for both CaO/(TLCT) SBA-15 (mesoporous) and CaO/ MM-(TLCT) SBA-15 (hierarchical) as calcium content increases at 60 ºC (II) Methyl butyrate formed for both CaO/(TLCT) SBA-15 (mesoporous) and CaO/ MM-(TLCT) SBA-15 (hierarchical) as calcium content increases at 60 ºC

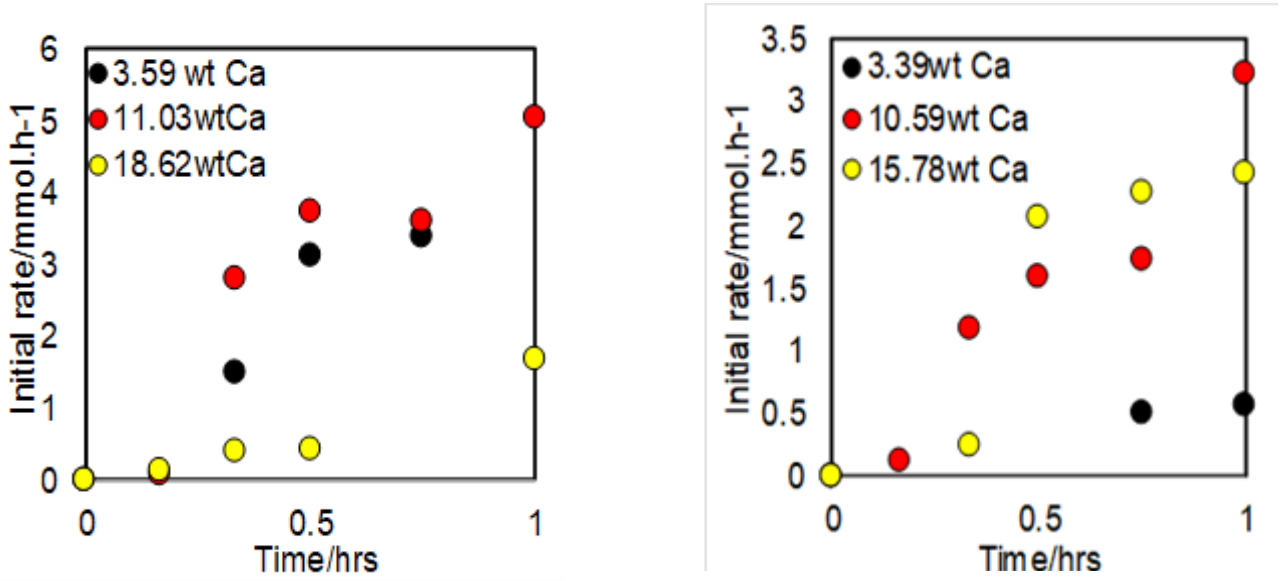

(III) (IV)

Figure 4. 33: (III) Initial rate for CaO/(TLCT) SBA-15 as calcium content increases at 60 ºC (IV) Initial rate formed for CaO/ MM-(TLCT) SBA-15 as calcium content is increased at 60 ºC

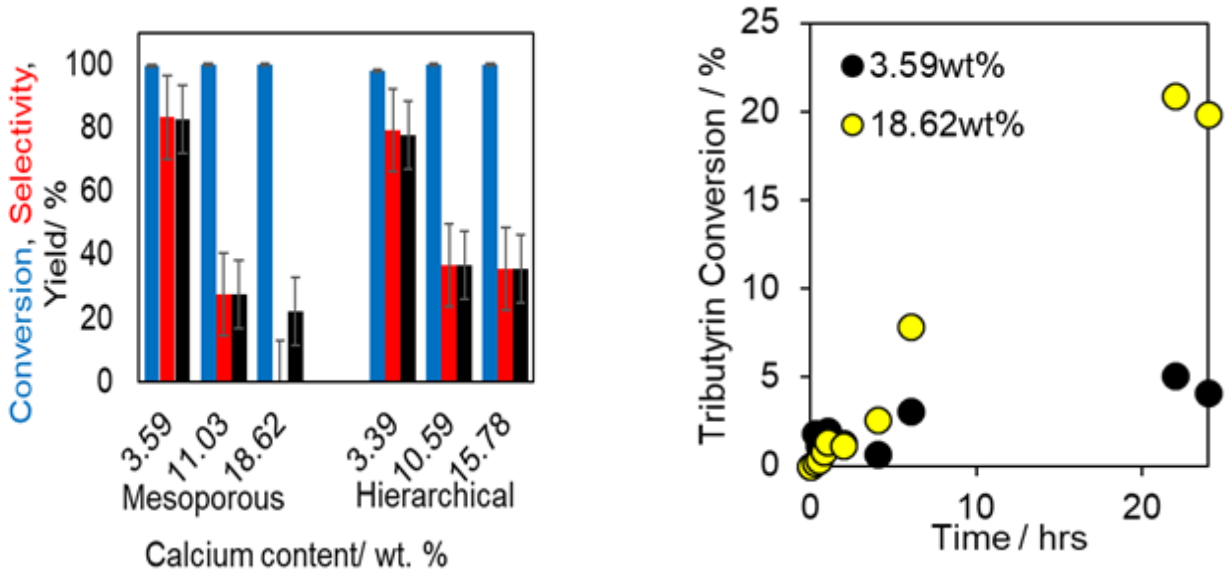

(V) (VI)

Figure 4. 34: (V) Conversion, methyl butyrate selectivity and FAME yield for both CaO/(TLCT) SBA-15 (mesoporous) and CaO/ MM-(TLCT) SBA-15(hierarchical) as calcium content increases at 90 ºC, (VI) Tributyrin conversion performed at 60ºC after CaO/(TLCT) SBA-15 catalysts are recalcined at 800 ºC

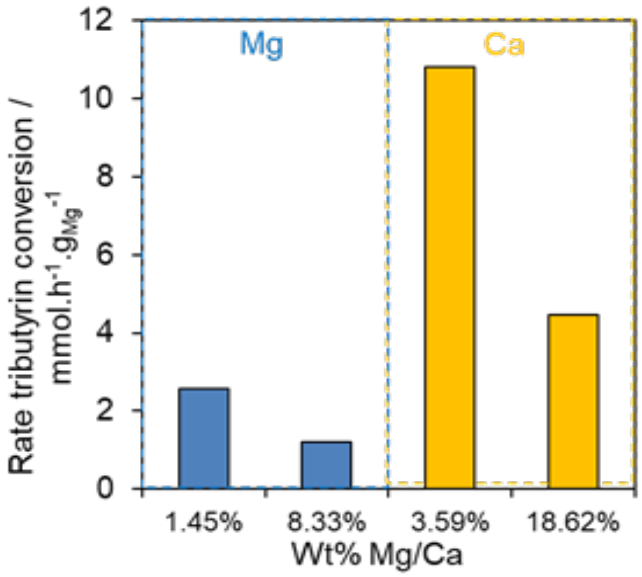

Figure 4. 35: Rate of tributyrin conversion for MgO/(TLCT) SBA-15 and CaO/(TLCT) SBA-15 at a reaction temperature of 60ºC using recalcined catalyst at 800ºC.

4.3 Performance/Yield of Catalysts using Higher Triglycerides - Tricaprylin Transesterification

Higher triglycerides were used to test the activity and stability of all synthesized catalysts. All synthesized catalysts were screened using tricaprylin, a C12 model triglycerides compound to produce tricaprylate as the corresponding fatty acid methyl ester.

4.3.1 Tricaprylin Transesterification: - MgO/(TLCT) SBA-15 and MgO/MM-(TLCT) SBA-15

MgO/(TLCT) SBA-15 and MgO/ MM-(TLCT) SBA-15 both showed activity for tricaprylin transesterification although lower than that of tributyrin due to being a larger triglyceride shown in Figure 4. 36. Reaction conditions could be adjusted to obtain high conversion and hence high yield of methyl tricaprylate however that was not of main interest. The greater interest was to study

the impact of the macropores upon the conversion rate. Figure 4. 36 shows a striking enhancement in the conversion rate as a function of macropore addition. The highest loading of MgO/MM-(TLCT) SBA-15 (8.51 wt.%) gave about 52% conversion as compared to the highest loading of MgO/(TLCT) SBA-15 (8.33 wt.%) giving about 45% conversion rate. This enhanced reactivity could be attributed to the greater accessibility of more basic sites present inside the mesopores of MgO/ MM-(TLCT) SBA-15 network. The higher mass transports throughout the pore network could occur in two (2) ways. First, the interpenetrating macropores could simply act as large conduits to boost tricaprylin bulk diffusion throughout catalyst particles. Secondly, by breaking up the mesopore domain size macropore incorporation may increase the density of accessible basic sites which are likely formed at the entrances to these mesopores [26].

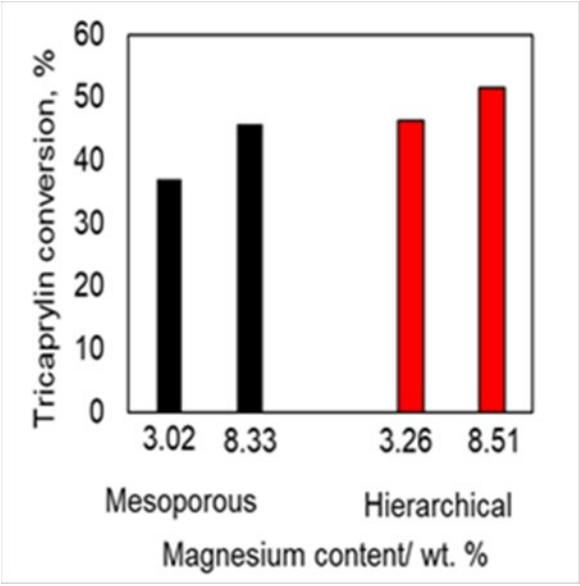

Figure 4. 36: Tricaprylin conversion for: MgO/(TLCT) SBA-15 and MgO/MM-(TLCT) SBA-15

4.3.2 Tricaprylin Transesterfication: CaO/(TLCT) SBA-15 and CaO/MM-(TLCT) SBA-15

Lower and higher loading of CaO/(TLCT) SBA-15 and CaO/MM-(TLCT) SBA-15 were tested for transesterification using tricaprylin, a model C_8 triglyceride at 90 ^oC. Figure 4. 37 shows that hierarchical materials showed a higher conversion rate than mesoporous materials as a function of an increase in calcium content. Therefore, introduction of macroporosity increases the rate of conversion due to higher diffusion.

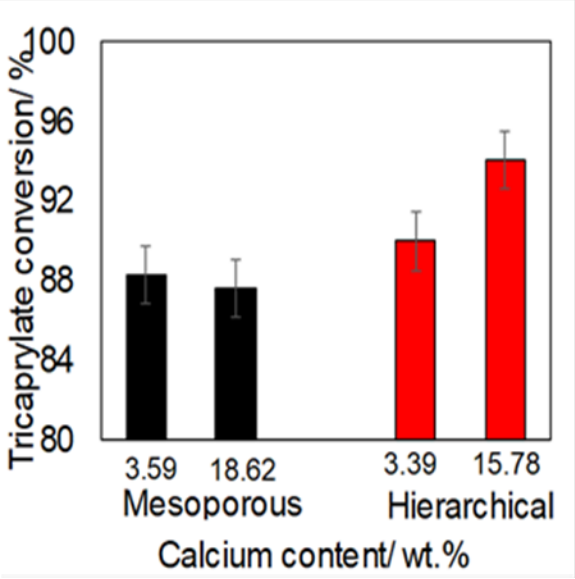

Figure 4. 37: Tricaprylin conversion for CaO/(TLCT) SBA-15 (mesoporous) and CaO/MM-(TLCT) SBA-15 (hierarchical) as calcium content increases

5.0 CONCLUSION AND RECOMMENDATIONS

In conclusion, both MgO/(TLCT) SBA-15 and CaO/(TLCT) SBA-15 using a one-pot TLCT method has been successfully synthesized. This method has been used as a modified method to incorporate macroporosity into aforementioned materials to form MgO/ MM (TLCT)-SBA-15 and CaO/ MM (TLCT)-SBA-15 hierarchical materials. These materials have been characterized using X-Ray diffraction, Inductively coupled plasma-optical emission spectroscopy (ICP OES), Nitrogen porosimetry, X-Ray photoelectron spectroscopy (XPS), Thermogravimetric analysis (TGA), Fourier transform infrared spectroscopy (IR), Scanning electron microscopy (SEM) coupled with Energy dispersive X-ray (EDX), and Transmission electron microscopy (TEM).

X-Ray diffraction results did not show large agglomerate particles of MgO and CaO crystallisation phases. This could have been as an indication that there was unsuccessful impregnation. However, this report was disputed by results obtained from ICP-OES which showed actual weight percentages of MgO or CaO respectively in synthesised materials.

Nitrogen porosimetry results showed higher surface areas between 200 – 600 $m^2 . g^{-1}$ using the "in-situ preparation method" than incipient wetness impregnation as reported in literature. These samples revealed stepwise adsorption and desorption isotherms of a typical type IV pattern with hysteresis loop which is a characteristic of mesoporous materials. BJH plots showed wider pore size distribution of 3nm dominant for both MgO and CaO synthesised catalysts.

X-Ray Photoelectron spectroscopy results showed the formation of more Mg–O–Mg bonds and less Mg-O-Si bonds as magnesium content was increased. Fourier transform spectroscopy analysis displayed asymmetric and symmetric stretching of Si-O-Si vibration, Si-OH groups and O-H groups. There was a slight decrease in Si-O-Si vibration as magnesium and calcium content was

increased. This could be attributed to the interaction between silicon and magnesium/calcium content.

Thermogravimetric analysis showed huge mass loss of physiosorbed water for both CaO and MgO synthesised materials. However, CaO synthesised materials also showed the desorption of calcium carbonates as well.

For all samples, SEM analysis mainly showed the formation of macropore template with mesopores within them. STEM results display long range ordering channels evident in mesoporous materials and also how macropore framework silica is formed of highly concentric mesoporous channels.

All synthesised samples were used as catalysts for the conversion of tributyrin and tricaprylin as model compounds representing the triglyceride component of bio-oil feedstock. It was seen that the activity of catalysts increased linearly with increasing magnesium and calcium loading. For tributyrin, it was seen that the mesomacropores materials slightly outperformed that of the mesoporous materials. For the larger model compound, tricaprylin, magnesium showed a striking enhancement in reactivity as macropores were added. A similar trend was observed for calcium materials in tributyrin conversion, Macropores increased the activity for both magnesium and calcium series however 3.59 wt.% CaO/MM - (TLCT) SBA-15 outperformed that of 18.62 wt.% CaO/ MM -(TLCT) SBA-15. Selectivity towards the production of methyl butyrate decreased as calcium weight percentages increased. This was due to the blockage of pores at higher weight percentages or carbonate poisoning. This effect led to the calcination of calcium materials at

800 ^{o}C to remove surface carbonates which could have led to reaction poisoning. At 800 ^{o}C, CaO/(TLCT) SBA-15 outperforms that of MgO/(TLCT) SBA-15. However, the lowest loading of

the CaO/(TLCT) SBA-15 (3.59 wt.%) proves to be the best catalyst among all synthesized catalysts. For larger triglyceride molecule, tricaprylin, 15.78 wt.% CaO/MM-(TLCT) SBA-15 proved to be the best catalyst among all catalysts.

It is highly recommended that the turnover frequencies (TOF) of the basic active sites of all samples should be determined using CO_2 chemisorption. Leaching tests should be run on the best catalyst to show the percentage and rate of leaching of metal oxides during reaction. The stability of samples should be tested by running the same catalyst at least four times in reaction to monitor its conversion rate. Also, other alkaline earth metal oxide or transition metal oxides could be investigated for comparative studies.

REFERENCES

[1] C. Azar, K. Lindgren, B.A. Andersson, Global energy scenarios meeting stringent CO 2 constraints—cost-effective fuel choices in the transportation sector, Energy Policy. 31 (2003) 961–976.

[2] J. Chow, R.J. Kopp, P.R. Portney, Energy resources and global development, Science (80-.). 302 (2003) 1528–1531.

[3] J.P. Dorian, H.T. Franssen, D.R. Simbeck, Global challenges in energy, Energy Policy. 34 (2006) 1984–1991.

[4] C. Azar, K. Lindgren, E. Larson, K. Möllersten, Carbon capture and storage from fossil fuels and biomass–Costs and potential role in stabilizing the atmosphere, Clim. Change. 74 (2006) 47–79.

[5] Y. Román-Leshkov, C.J. Barrett, Z.Y. Liu, J.A. Dumesic, Production of dimethylfuran for liquid fuels from biomass-derived carbohydrates, Nature. 447 (2007) 982–985.

[6] S.H. Sajjad, N. Blond, A. Clappier, A. Raza, S.A. Shirazi, K. Shakrullah, The preliminary study of urbanization, fossil fuels consumptions and CO 2 emission in Karachi, African J. Biotechnol. 9 (2010) 1941–1948.

[7] R. Madlener, Y. Sunak, Impacts of urbanization on urban structures and energy demand: What can we learn for urban energy planning and urbanization management?, Sustain. Cities Soc. 1 (2011) 45–53.

[8] R. York, Do alternative energy sources displace fossil fuels?, Nat. Clim. Chang. 2 (2012) 441–443.

[9] S. Grimmond, Urbanization and global environmental change: local effects of urban warming, Geogr. J. 173 (2007) 83–88.

[10] D.O. Hall, J.I. Scrase, Will biomass be the environmentally friendly fuel of the future?, Biomass and Bioenergy. 15 (1998) 357–367.

[11] A. Omri, N. Ben Mabrouk, A. Sassi-Tmar, Modeling the causal linkages between nuclear energy, renewable energy and economic growth in developed and developing countries, Renew. Sustain. Energy Rev. 42 (2015) 1012–1022.

[12] B. Kelly, B. Keeler, G. Helm, G. Krantzberg, T. Lyon, W. Mabee, Energy as a driver of

change in the Great Lakes–St. Lawrence River basin, J. Great Lakes Res. 41 (2015) 59–68.

[13] N. Ghaffour, J. Bundschuh, H. Mahmoudi, M.F.A. Goosen, Renewable energy-driven desalination technologies: a comprehensive review on challenges and potential applications of integrated systems, Desalination. 356 (2015) 94–114.

[14] K. Novan, Valuing the wind: renewable energy policies and air pollution avoided, Am. Econ. J. Econ. Policy. 7 (2015) 291–326.

[15] H. Lund, Renewable energy strategies for sustainable development, Energy. 32 (2007) 912–919.

[16] V.Ş. Ediger, E. Kentel, Renewable energy potential as an alternative to fossil fuels in Turkey, Energy Convers. Manag. 40 (1999) 743–755.

[17] S. Naik, V. V Goud, P.K. Rout, K. Jacobson, A.K. Dalai, Characterization of Canadian biomass for alternative renewable biofuel, Renew. Energy. 35 (2010) 1624–1631.

[18] M. Habibullah, H.H. Masjuki, M.A. Kalam, S.M.A. Rahman, M. Mofijur, H.M. Mobarak, A.M. Ashraful, Potential of biodiesel as a renewable energy source in Bangladesh, Renew. Sustain. Energy Rev. 50 (2015) 819–834.

[19] T. Eryilmaz, M.K. Yesilyurt, C. Cesur, O. Gokdogan, Biodiesel production potential from oil seeds in Turkey, Renew. Sustain. Energy Rev. 58 (2016) 842–851.

[20] T.W. Lester, M.G. Little, G.J. Jolley, Assessing the Economic Impact of Alternative Biomass Uses: Biofuels, Wood Pellets, and Energy Production, J. Reg. Anal. Policy. 45 (2015) 36.

[21] T.K. Hari, Z. Yaakob, N.N. Binitha, Aviation biofuel from renewable resources: routes, opportunities and challenges, Renew. Sustain. Energy Rev. 42 (2015) 1234–1244.

[22] A.K. Azad, M.G. Rasul, M.M.K. Khan, S.C. Sharma, M.A. Hazrat, Prospect of biofuels as an alternative transport fuel in Australia, Renew. Sustain. Energy Rev. 43 (2015) 331–351.

[23] A. Limayem, S.C. Ricke, Lignocellulosic biomass for bioethanol production: current perspectives, potential issues and future prospects, Prog. Energy Combust. Sci. 38 (2012) 449–467.

[24] L. Brennan, P. Owende, Biofuels from microalgae—a review of technologies for production, processing, and extractions of biofuels and co-products, Renew. Sustain.

Energy Rev. 14 (2010) 557–577.

[25] J. BONTEMPS, M. BUREL, A. DRAGOMIR, E. DUMITRESCU, Biofuels and food production Ethical issues, Proc. IP Bioeth. Life Sci. Environ. Sci. Lublin, Http//tinyurl. com/owkgbs3. (2009).

[26] A.F. Lee, J.A. Bennett, J.C. Manayil, K. Wilson, Heterogeneous catalysis for sustainable biodiesel production via esterification and transesterification, Chem. Soc. Rev. 43 (2014) 7887–7916.

[27] R.A. Nalepa, D.M. Bauer, Marginal lands: the role of remote sensing in constructing landscapes for agrofuel development, J. Peasant Stud. 39 (2012) 403–422.

[28] S.N. Naik, V. V Goud, P.K. Rout, A.K. Dalai, Production of first and second generation biofuels: a comprehensive review, Renew. Sustain. Energy Rev. 14 (2010) 578–597.

[29] Y.C. Sharma, B. Singh, S.N. Upadhyay, Advancements in development and characterization of biodiesel: a review, Fuel. 87 (2008) 2355–2373.

[30] P.S. Nigam, A. Singh, Production of liquid biofuels from renewable resources, Prog. Energy Combust. Sci. 37 (2011) 52–68.

[31] E. Martinez-Guerra, V.G. Gude, Continuous and pulse sonication effects on transesterification of used vegetable oil, Energy Convers. Manag. 96 (2015) 268–276.

[32] E. Ondul, N. Dizge, B. Keskinler, N. Albayrak, Biocatalytic Production of Biodiesel from Vegetable Oils, (2015).

[33] M. Saeedi, R. Fazaeli, H. Aliyan, Nanostructured sodium–zeolite imidazolate framework (ZIF-8) doped with potassium by sol–gel processing for biodiesel production from soybean oil, J. Sol-Gel Sci. Technol. (2015) 1–12.

[34] G.-Y. Chen, R. Shan, J.-F. Shi, B.-B. Yan, Transesterification of palm oil to biodiesel using rice husk ash-based catalysts, Fuel Process. Technol. 133 (2015) 8–13.

[35] T.M. Albayati, A.M. Doyle, Encapsulated heterogeneous base catalysts onto SBA-15 nanoporous material as highly active catalysts in the transesterification of sunflower oil to biodiesel, J. Nanoparticle Res. 17 (2015) 1–10.

[36] B. Lertpanyapornchai, C. Ngamcharussrivichai, Mesostructured Sr and Ti mixed oxides as heterogeneous base catalysts for transesterification of palm kernel oil with methanol, Chem. Eng. J. 264 (2015) 789–796.

[37] S.H. Teo, U. Rashid, S.Y.T. Choong, Y.H. Taufiq-Yap, Heterogeneous calcium-based

bimetallic oxide catalyzed transesterification of Elaeis guineensis derived triglycerides for biodiesel production, Energy Convers. Manag. (2016).

[38] N. Pal, A. Bhaumik, Mesoporous materials: versatile supports in heterogeneous catalysis for liquid phase catalytic transformations, RSC Adv. 5 (2015) 24363–24391.

[39] G.D. Yadav, S.R. Jadhav, Synthesis of reusable lipases by immobilization on hexagonal mesoporous silica and encapsulation in calcium alginate: transesterification in non-aqueous medium, Microporous Mesoporous Mater. 86 (2005) 215–222.

[40] V. Varela Guerrero, D.F. Shantz, Amine-Functionalized Ordered Mesoporous Silica Transesterification Catalysts, Ind. Eng. Chem. Res. 48 (2009) 10375–10380.

[41] I.K. Mbaraka, B.H. Shanks, Conversion of oils and fats using advanced mesoporous heterogeneous catalysts, J. Am. Oil Chem. Soc. 83 (2006) 79–91.

[42] A. Corma, From microporous to mesoporous molecular sieve materials and their use in catalysis, Chem. Rev. 97 (1997) 2373–2420.

[43] W. Ding, W. Zhu, J. Xiong, L. Yang, A. Wei, M. Zhang, H. Li, Novel heterogeneous iron-based redox ionic liquid supported on SBA-15 for deep oxidative desulfurization of fuels, Chem. Eng. J. 266 (2015) 213–221.

[44] W. Xie, L. Hu, X. Yang, Basic ionic liquid supported on mesoporous SBA-15 silica as an efficient heterogeneous catalyst for biodiesel production, Ind. Eng. Chem. Res. 54 (2015) 1505–1512.

[45] Y. Chen, Y. Cao, Y. Suo, G.-P. Zheng, X.-X. Guan, X.-C. Zheng, Mesoporous solid acid catalysts of 12-tungstosilicic acid anchored to SBA-15: Characterization and catalytic properties for esterification of oleic acid with methanol, J. Taiwan Inst. Chem. Eng. 51 (2015) 186–192.

[46] N. Boz, N. Degirmenbasi, Biodiesel Production from Canola Oil with Methanol in Presence of Nanocrystalline MgO-Supported Alkaline Catalysts, Asian J. Chem. 28 (2016) 261.

[47] G.S. Attard, J.C. Glyde, C.G. GOltner, Liquid-crystalline phases as templates for the synthesis of mesoporous silica, Nature. 378 (1995) 366–368.

[48] I. Dincer, M.A. Rosen, Energy, environment and sustainable development, Appl. Energy. 64 (1999) 427–440.

[49] G.R. Van der Werf, D.C. Morton, R.S. DeFries, J.G.J. Olivier, P.S. Kasibhatla, R.B.

Jackson, G.J. Collatz, J.T. Randerson, CO2 emissions from forest loss, Nat. Geosci. 2 (2009) 737–738.

[50] T.J. Battin, S. Luyssaert, L.A. Kaplan, A.K. Aufdenkampe, A. Richter, L.J. Tranvik, The boundless carbon cycle, Nat. Geosci. 2 (2009) 598.

[51] E. Worrell, L. Price, N. Martin, C. Hendriks, L.O. Meida, Carbon dioxide emissions from the global cement industry, Annu. Rev. Energy Environ. 26 (2001) 303–329.

[52] J. Hill, E. Nelson, D. Tilman, S. Polasky, D. Tiffany, Environmental, economic, and energetic costs and benefits of biodiesel and ethanol biofuels, Proc. Natl. Acad. Sci. 103 (2006) 11206–11210.

[53] L. Van de Velde, W. Verbeke, M. Popp, J. Buysse, G. Van Huylenbroeck, Perceived importance of fuel characteristics and its match with consumer beliefs about biofuels in Belgium, Energy Policy. 37 (2009) 3183–3193.

[54] A.M. Liaquat, M.A. Kalam, H.H. Masjuki, M.H. Jayed, Potential emissions reduction in road transport sector using biofuel in developing countries, Atmos. Environ. 44 (2010) 3869–3877.

[55] W. Vermerris, A. Saballos, G. Ejeta, N.S. Mosier, M.R. Ladisch, N.C. Carpita, Molecular breeding to enhance ethanol production from corn and sorghum stover, Crop Sci. 47 (2007) S-142.

[56] J. Van Gerpen, Biodiesel processing and production, Fuel Process. Technol. 86 (2005) 1097–1107.

[57] P.M. Schenk, S.R. Thomas-Hall, E. Stephens, U.C. Marx, J.H. Mussgnug, C. Posten, O. Kruse, B. Hankamer, Second generation biofuels: high-efficiency microalgae for biodiesel production, Bioenergy Res. 1 (2008) 20–43.

[58] E. Lotero, Y. Liu, D.E. Lopez, K. Suwannakarn, D. a. Bruce, J.G. Goodwin, Synthesis of Biodiesel via Acid Catalysis, Ind. Eng. Chem. Res. 44 (2005) 5353–5363. doi:10.1021/ie049157g.

[59] D. Bajpai, V.K. Tyagi, Biodiesel: source, production, composition, properties and its benefits, J. Oleo Sci. 55 (2006) 487–502.

[60] L.C. Meher, D.V. Sagar, S.N. Naik, Technical aspects of biodiesel production by transesterification—a review, Renew. Sustain. Energy Rev. 10 (2006) 248–268.

[61] H. Fukuda, A. Kondo, H. Noda, Biodiesel fuel production by transesterification of oils, J.

Biosci. Bioeng. 92 (2001) 405–416.

[62] P. Tatsidjodoung, M.-H. Dabat, J. Blin, Insights into biofuel development in Burkina Faso: Potential and strategies for sustainable energy policies, Renew. Sustain. Energy Rev. 16 (2012) 5319–5330.

[63] S.A. Khan, M.Z. Hussain, S. Prasad, U.C. Banerjee, Prospects of biodiesel production from microalgae in India, Renew. Sustain. Energy Rev. 13 (2009) 2361–2372.

[64] N. Habib-Mintz, Biofuel investment in Tanzania: Omissions in implementation, Energy Policy. 38 (2010) 3985–3997.

[65] C.S.K. Lin, L.A. Pfaltzgraff, L. Herrero-Davila, E.B. Mubofu, S. Abderrahim, J.H. Clark, A.A. Koutinas, N. Kopsahelis, K. Stamatelatou, F. Dickson, Food waste as a valuable resource for the production of chemicals, materials and fuels. Current situation and global perspective, Energy Environ. Sci. 6 (2013) 426–464.

[66] W. Zhu, T.A. Lestander, H. Örberg, M. Wei, B. Hedman, J. Ren, G. Xie, S. Xiong, Cassava stems: a new resource to increase food and fuel production, Gcb Bioenergy. 7 (2015) 72–83.

[67] A. Demirbas, Use of algae as biofuel sources, Energy Convers. Manag. 51 (2010) 2738–2749.

[68] T.M. Mata, A.A. Martins, N.S. Caetano, Microalgae for biodiesel production and other applications: a review, Renew. Sustain. Energy Rev. 14 (2010) 217–232.

[69] P. Walden, The Gmelin chemical dynasty, J. Chem. Educ. 31 (1954) 534.

[70] F.H. Mattson, R.A. Volpenhein, The digestion and absorption of triglycerides, J. Biol. Chem. 239 (1964) 2772–2777.

[71] R.B. Meyer, L. Liebert, L. Strzelecki, P. Keller, Ferroelectric liquid crystals, J. Phys. Lettres. 36 (1975) 69–71.

[72] L. Zhang, J. Xia, Q. Zhao, L. Liu, Z. Zhang, Functional graphene oxide as a nanocarrier for controlled loading and targeted delivery of mixed anticancer drugs, Small. 6 (2010) 537–544.

[73] E.J. Vandamme, W. Soetaert, Bioflavours and fragrances via fermentation and biocatalysis, J. Chem. Technol. Biotechnol. 77 (2002) 1323–1332.

[74] A. Güvenç, N. Kapucu, Ü. Mehmetoğlu, The production of isoamyl acetate using immobilized lipases in a solvent-free system, Process Biochem. 38 (2002) 379–386.

[75] P. Somasundaran, T.W. Healy, D.W. Fuerstenau, Surfactant adsorption at the solid—liquid interface—dependence of mechanism on chain length, J. Phys. Chem. 68 (1964) 3562–3566.

[76] M.Y. Koh, T.I.M. Ghazi, A review of biodiesel production from Jatropha curcas L. oil, Renew. Sustain. Energy Rev. 15 (2011) 2240–2251.

[77] M.J. Hills, I. Kiewitt, K.D. Mukherjee, Synthetic reactions catalyzed by immobilized lipase from oilseed rape (Brassica napus L.), Appl. Biochem. Biotechnol. 27 (1991) 123–129.

[78] J. Devaux, P. Godard, J.P. Mercier, Bisphenol-A polycarbonate–poly (butylene terephthalate) transesterification. III. Study of model reactions, J. Polym. Sci. Part B Polym. Phys. 20 (1982) 1895–1900.

[79] K.-H. Wei, J.-C. Ho, The role of transesterification on the miscibility in blends of polycarbonate and liquid crystalline copolyester, Macromolecules. 30 (1997) 1587–1593.

[80] M.J. Haas, Improving the economics of biodiesel production through the use of low value lipids as feedstocks: vegetable oil soapstock, Fuel Process. Technol. 86 (2005) 1087–1096.

[81] Z.J. Predojević, The production of biodiesel from waste frying oils: A comparison of different purification steps, Fuel. 87 (2008) 3522–3528.

[82] F. Ma, M.A. Hanna, Biodiesel production: a review, Bioresour. Technol. 70 (1999) 1–15.

[83] M. Tariq, S. Ali, N. Khalid, Activity of homogeneous and heterogeneous catalysts, spectroscopic and chromatographic characterization of biodiesel: a review, Renew. Sustain. Energy Rev. 16 (2012) 6303–6316.

[84] D.E. Lopez, J.G. Goodwin, D.A. Bruce, E. Lotero, Transesterification of triacetin with methanol on solid acid and base catalysts, Appl. Catal. A Gen. 295 (2005) 97–105.

[85] R.A. Sheldon, The E factor: fifteen years on, Green Chem. 9 (2007) 1273–1283.

[86] V. V Bokade, G.D. Yadav, Synthesis of bio-diesel and bio-lubricant by transesterification of vegetable oil with lower and higher alcohols over heteropolyacids supported by clay (K-10), Process Saf. Environ. Prot. 85 (2007) 372–377.

[87] A.V. Smirnov, O.G. Orlov, P.N. Golipad, Y.N. Koriakin, L.T. Vyalchenkov, Process for separating a hydrophobic liquid from a liquid contaminated therewith, (1998).

[88] I.W. Davies, L. Matty, D.L. Hughes, P.J. Reider, Are heterogeneous catalysts precursors

to homogeneous catalysts?, J. Am. Chem. Soc. 123 (2001) 10139–10140.

[89] K. Motokura, M. Tada, Y. Iwasawa, Layered materials with coexisting acidic and basic sites for catalytic one-pot reaction sequences, J. Am. Chem. Soc. 131 (2009) 7944–7945.

[90] M.E. Borges, L. Díaz, Recent developments on heterogeneous catalysts for biodiesel production by oil esterification and transesterification reactions: a review, Renew. Sustain. Energy Rev. 16 (2012) 2839–2849.

[91] H. Hattori, Heterogeneous basic catalysis, Chem. Rev. 95 (1995) 537–558.

[92] M. Akia, F. Yazdani, E. Motaee, D. Han, H. Arandiyan, A review on conversion of biomass to biofuel by nanocatalysts, Biofuel Res. J. 1 (2014) 16–25.

[93] A.P.S. Chouhan, A.K. Sarma, Modern heterogeneous catalysts for biodiesel production: A comprehensive review, Renew. Sustain. Energy Rev. 15 (2011) 4378–4399.

[94] C. Xu, D.I. Enache, R. Lloyd, D.W. Knight, J.K. Bartley, G.J. Hutchings, MgO catalysed triglyceride transesterification for biodiesel synthesis, Catal. Letters. 138 (2010) 1–7.

[95] X. Liu, X. Piao, Y. Wang, S. Zhu, H. He, Calcium methoxide as a solid base catalyst for the transesterification of soybean oil to biodiesel with methanol, Fuel. 87 (2008) 1076–1082.

[96] N.C.S. Selvam, R.T. Kumar, L.J. Kennedy, J.J. Vijaya, Comparative study of microwave and conventional methods for the preparation and optical properties of novel MgO-micro and nano-structures, J. Alloys Compd. 509 (2011) 9809–9815.

[97] K. Zhu, J. Hu, C. Kuebel, R. Richards, Efficient preparation and catalytic activity of MgO (111) nanosheets, Angew. Chemie. 118 (2006) 7435–7439.

[98] L. Yan, J. Zhuang, X. Sun, Z. Deng, Y. Li, Formation of rod-like Mg (OH) 2 nanocrystallites under hydrothermal conditions and the conversion to MgO nanorods by thermal dehydration, Mater. Chem. Phys. 76 (2002) 119–122.

[99] K.L. Klug, V.P. Dravid, Observation of two-and three-dimensional magnesium oxide nanostructures formed by thermal treatment of magnesium diboride powder, Appl. Phys. Lett. 81 (2002) 1687–1689.

[100] P. Wange, T. Höche, C. Rüssel, J.D. Schnapp, Microstructure-property relationship in high-strength MgO–Al 2 O 3–SiO 2–TiO 2 glass-ceramics, J. Non. Cryst. Solids. 298 (2002) 137–145.

[101] J.M. Montero, P. Gai, K. Wilson, A.F. Lee, Structure-sensitive biodiesel synthesis over

MgO nanocrystals, Green Chem. 11 (2009) 265–268.

[102] L. Wang, J. Yang, Transesterification of soybean oil with nano-MgO or not in supercritical and subcritical methanol, Fuel. 86 (2007) 328–333.

[103] M. Kouzu, T. Kasuno, M. Tajika, Y. Sugimoto, S. Yamanaka, J. Hidaka, Calcium oxide as a solid base catalyst for transesterification of soybean oil and its application to biodiesel production, Fuel. 87 (2008) 2798–2806.

[104] Z. Huaping, W.U. Zongbin, C. Yuanxiong, P. Zhang, D. Shijie, L.I.U. Xiaohua, M.A.O. Zongqiang, Preparation of biodiesel catalyzed by solid super base of calcium oxide and its refining process, Chinese J. Catal. 27 (2006) 391–396.

[105] M.L. Granados, M.D.Z. Poves, D.M. Alonso, R. Mariscal, F.C. Galisteo, R. Moreno-Tost, J. Santamaría, J.L.G. Fierro, Biodiesel from sunflower oil by using activated calcium oxide, Appl. Catal. B Environ. 73 (2007) 317–326.

[106] E.M. Johansson, Controlling the pore size and morphology of mesoporous silica, (2010).

[107] A. Thomas, F. Goettmann, M. Antonietti, Hard templates for soft materials: creating nanostructured organic materials, Chem. Mater. 20 (2008) 738–755.

[108] K. Ishizaki, S. Komarneni, M. Nanko, Porous Materials: Process technology and applications, Springer Science & Business Media, 2013.

[109] S. Xu, Y. Hong, C. Chen, S. Li, L. Xiao, J. Fan, A general synthetic strategy for ordered, extra-large mesoporous metal oxides via uniform sol–gel coating, J. Mater. Chem. A. 1 (2013) 6191–6198.

[110] Y. Wan, D. Zhao, On the controllable soft-templating approach to mesoporous silicates, Chem. Rev. 107 (2007) 2821–2860.

[111] C.T. Kresge, M.E. Leonowicz, W.J. Roth, J.C. Vartuli, J.S. Beck, Ordered mesoporous molecular sieves synthesized by a liquid-crystal template mechanism, Nature. 359 (1992) 710–712.

[112] B. Naik, N.N. Ghosh, A review on chemical methodologies for preparation of mesoporous silica and alumina based materials, Recent Pat. Nanotechnol. 3 (2009) 213–224.

[113] U. Ciesla, F. Schüth, Ordered mesoporous materials, Microporous Mesoporous Mater. 27 (1999) 131–149.

[114] J.A. Sullivan, L. Sherry, Different dispersions of group II catalysts over SBA-15 and MCM-41: Effects on transesterification reactivity, Catal. Commun. 60 (2015) 88–91.

[115] D. Zhao, J. Feng, Q. Huo, N. Melosh, G.H. Fredrickson, B.F. Chmelka, G.D. Stucky, Triblock copolymer syntheses of mesoporous silica with periodic 50 to 300 angstrom pores, Science (80-.). 279 (1998) 548–552.

[116] E. Li, V. Rudolph, Transesterification of vegetable oil to biodiesel over MgO-functionalized mesoporous catalysts, Energy & Fuels. 22 (2007) 145–149.

[117] W. Xie, L. Zhao, Heterogeneous CaO–MoO 3–SBA-15 catalysts for biodiesel production from soybean oil, Energy Convers. Manag. 79 (2014) 34–42.

[118] H. Sun, J. Han, Y. Ding, W. Li, J. Duan, P. Chen, H. Lou, X. Zheng, One-pot synthesized mesoporous Ca/SBA-15 solid base for transesterification of sunflower oil with methanol, Appl. Catal. A Gen. 390 (2010) 26–34.

[119] M.C.G. Albuquerque, I. Jiménez-Urbistondo, J. Santamaría-González, J.M. Mérida-Robles, R. Moreno-Tost, E. Rodríguez-Castellón, A. Jiménez-López, D.C.S. Azevedo, C.L. Cavalcante Jr, P. Maireles-Torres, CaO supported on mesoporous silicas as basic catalysts for transesterification reactions, Appl. Catal. A Gen. 334 (2008) 35–43.

[120] P. Yang, D. Zhao, D.I. Margolese, B.F. Chmelka, G.D. Stucky, Generalized syntheses of large-pore mesoporous metal oxides with semicrystalline frameworks, Nature. 396 (1998) 152.

[121] Y. Meng, D. Gu, F. Zhang, Y. Shi, L. Cheng, D. Feng, Z. Wu, Z. Chen, Y. Wan, A. Stein, A family of highly ordered mesoporous polymer resin and carbon structures from organic− organic self-assembly, Chem. Mater. 18 (2006) 4447–4464.

[122] K. Suzuki, K. Ikari, H. Imai, Synthesis of silica nanoparticles having a well-ordered mesostructure using a double surfactant system, J. Am. Chem. Soc. 126 (2004) 462–463.

[123] Y. Lu, H. Fan, A. Stump, T.L. Ward, Aerosol-assisted self-assembly of mesostructured spherical nanoparticles, Nature. 398 (1999) 223.

[124] W. Li, D. Zhao, An overview of the synthesis of ordered mesoporous materials, Chem. Commun. 49 (2013) 943–946.

[125] G. Kume, M. Gallotti, G. Nunes, Review on anionic/cationic surfactant mixtures, J. Surfactants Deterg. 11 (2008) 1–11.

[126] G. Nałęcz-Jawecki, E. Grabińska-Sota, P. Narkiewicz, The toxicity of cationic surfactants in four bioassays, Ecotoxicol. Environ. Saf. 54 (2003) 87–91.

[127] M.A. Malik, M.A. Hashim, F. Nabi, S.A. Al-Thabaiti, Z. Khan, Anti-corrosion ability of

surfactants: a review, Int. J. Electrochem. Sci. 6 (2011) 1927–1948.

[128] P. Somasundaran, S.C. Mehta, P. Purohit, Silicone emulsions, Adv. Colloid Interface Sci. 128 (2006) 103–109.

[129] M.J. Rosen, J.T. Kunjappu, Surfactants and interfacial phenomena, John Wiley & Sons, 2012.

[130] Y. Deng, J. Liu, C. Liu, D. Gu, Z. Sun, J. Wei, J. Zhang, L. Zhang, B. Tu, D. Zhao, Ultra-large-pore mesoporous carbons templated from poly (ethylene oxide)-b-polystyrene diblock copolymer by adding polystyrene homopolymer as a pore expander, Chem. Mater. 20 (2008) 7281–7286.

[131] T.J. Bandosz, Materials for catalysis, Surf. Chem. Carbon Mater. (2009) 45–92.

[132] U.S. Ozkan, Design of heterogeneous catalysts, John Wiley & Sons, 2009.

[133] S. Ruthstein, V. Frydman, D. Goldfarb, Study of the initial formation stages of the mesoporous material SBA-15 using spin-labeled block co-polymer templates, J. Phys. Chem. B. 108 (2004) 9016–9022.

[134] S. Ruthstein, V. Frydman, S. Kababya, M. Landau, D. Goldfarb, Study of the formation of the mesoporous material SBA-15 by EPR spectroscopy, J. Phys. Chem. B. 107 (2003) 1739–1748.

[135] K. Flodström, H. Wennerström, V. Alfredsson, Mechanism of Mesoporous Silica Formation. A Time-Resolved NMR and TEM Study of Silica− Block Copolymer Aggregation, Langmuir. 20 (2004) 680–688.

[136] C.M.A. Parlett, K. Wilson, A.F. Lee, Hierarchical porous materials: catalytic applications, Chem. Soc. Rev. 42 (2013) 3876–3893.

[137] C.M.A. Parlett, M.A. Isaacs, S.K. Beaumont, L.M. Bingham, N.S. Hondow, K. Wilson, A.F. Lee, Spatially orthogonal chemical functionalization of a hierarchical pore network for catalytic cascade reactions, Nat. Mater. 15 (2016) 178–182.

[138] B.D. Cullity, Elements of X-Ray Diffraction 2nd edition. Addision-Wesley Pub. Co, Inc., CA, USA. 197 (1978) 356.

[139] A.E. Delgado, D.-W. Sun, Desorption isotherms and glass transition temperature for chicken meat, J. Food Eng. 55 (2002) 1–8.

[140] J.F. Watts, J. Wolstenholme, Compositional Depth Profiling, An Introd. to Surf. Anal. by XPS AES. (2003) 79–111.

[141] S.L. Flegler, J.W. Heckman Jr, K.L. Klomparens, Scanning and transmission electron microscopy: an introduction, Oxford Univ. Press. 1993,. (1993) 225.

[142] M.A. Bush, R.G. Miller, A.L. Norrlander, P.J. Bush, Analytical survey of restorative resins by SEM/EDS and XRF: databases for forensic purposes, J. Forensic Sci. 53 (2008) 419–425.

[143] D. Macias-Ferrer, J.A. Melo-Banda, R. Silva-Rodrigo, M. Lam-Maldonado, U. Páramo-García, J.Y. Verde-Gómez, P. Del-Ángel-Vicente, Highly Dispersed PtCo Nanoparticles on Micro/nano-structured Pyrolytic Carbon from Refined Sugar for Methanol Electro-oxidation in Acid Media, Catal. Today. (2018).

[144] D. Yue, J. Lei, Y. Peng, J. Li, X. Du, Hierarchical ordered meso/macroporous H 3 PW 12 O 40/SiO 2 catalysts with superior oxidative desulfurization activity, J. Porous Mater. (2017) 1–8.

[145] Y.M. Wang, Z.Y. Wu, Y.L. Wei, J.H. Zhu, In situ coating metal oxide on SBA-15 in one-pot synthesis, Microporous Mesoporous Mater. 84 (2005) 127–136.

[146] Y.L. Wei, Y.M. Wang, J.H. Zhu, Z.Y. Wu, In-Situ Coating of SBA-15 with MgO: Direct Synthesis of Mesoporous Solid Bases from Strong Acidic Systems, Adv. Mater. 15 (2003) 1943–1945.

[147] N.J. Amos, M. Widyawati, S. Kureti, D. Trimis, A.I. Minett, A.T. Harris, T.L. Church, Design and synthesis of stable supported-CaO sorbents for CO 2 capture, J. Mater. Chem. A. 2 (2014) 4332–4339.

[148] A. Grosman, C. Ortega, Nature of capillary condensation and evaporation processes in ordered porous materials, Langmuir. 21 (2005) 10515–10521.

[149] R. Wang, X. Liu, Y. He, Q. Yuan, X. Li, G. Lu, T. Zhang, The humidity-sensitive property of MgO-SBA-15 composites in one-pot synthesis, Sensors Actuators B Chem. 145 (2010) 386–393.

[150] Y.-F. Han, F. Chen, Z. Zhong, K. Ramesh, L. Chen, E. Widjaja, Controlled synthesis, characterization, and catalytic properties of Mn2O3 and Mn3O4 nanoparticles supported on mesoporous silica SBA-15, J. Phys. Chem. B. 110 (2006) 24450–24456.

[151] W. Xie, L. Zhao, Heterogeneous CaO–MoO3–SBA-15 catalysts for biodiesel production from soybean oil, Energy Convers. Manag. 79 (2014) 34–42.

[152] L.B. Sun, J.H. Kou, Y. Chun, J. Yang, F.N. Gu, Y. Wang, J.H. Zhu, Z.G. Zou, New

attempt at directly generating superbasicity on mesoporous silica SBA-15, Inorg. Chem. 47 (2008) 4199–4208.

[153] N. Kaur, A. Ali, Biodiesel production via ethanolysis of jatropha oil using molybdenum impregnated calcium oxide as solid catalyst, RSC Adv. 5 (2015) 13285–13295.

[154] A. Katiyar, S. Yadav, P.G. Smirniotis, N.G. Pinto, Synthesis of ordered large pore SBA-15 spherical particles for adsorption of biomolecules, J. Chromatogr. A. 1122 (2006) 13–20.

[155] D. Zhao, J. Sun, Q. Li, G.D. Stucky, Morphological control of highly ordered mesoporous silica SBA-15, Chem. Mater. 12 (2000) 275–279.

[156] Y. Deng, T. Yu, Y. Wan, Y. Shi, Y. Meng, D. Gu, L. Zhang, Y. Huang, C. Liu, X. Wu, Ordered mesoporous silicas and carbons with large accessible pores templated from amphiphilic diblock copolymer poly (ethylene oxide)-b-polystyrene, J. Am. Chem. Soc. 129 (2007) 1690–1697.

[157] J. Dhainaut, J.-P. Dacquin, A.F. Lee, K. Wilson, Hierarchical macroporous–mesoporous SBA-15 sulfonic acid catalysts for biodiesel synthesis, Green Chem. 12 (2010) 296–303.

[158] J.W. Morse, R.S. Arvidson, A. Lüttge, Calcium carbonate formation and dissolution, Chem. Rev. 107 (2007) 342–381.